UNIVERSITY OF CALIFORNIA, SAN DIEGO

Structural Studies of Liquid Surface Self-Assembled Iron Oxide Nanoparticle Monolayers

A dissertation submitted in partial satisfaction of the
requirements for the degree
Doctor of Philosophy

in

Physics

by

Jacob Stanley

Committee in charge:

Oleg Shpyrko, Chair
Michael Anderson
Eric Fullerton
Shirley Meng
Sunil Sinha

2015

The dissertation of Jacob Stanley is approved, and it is acceptable in quality and form for publication on microfilm and electronically:

_____

_____

_____

_____

_____
Chair

University of California, San Diego

2015

EPIGRAPH

Great things are not done by impulse, but by a series of small things brought together.

—Vincent van Gogh

TABLE OF CONTENTS

LIST OF FIGURES

LIST OF TABLES

ACKNOWLEDGEMENTS

First I would like to express my gratitude to my advisor, Professor Oleg Shpyrko without whom this work would not have been possible. His patient encouragement has helped keep me motivated and productive during the 3+ years I've been in his group. He provided me the freedom to pursue the project in the way I found most compelling, but made sure that it did not get too far afield.

Oleg's countless anecdotes, words of wisdom, and Russian proverbs/jokes have taught me a lot more about life in academia than I had expected to get out of graduate school. More than just about the science of X-Ray scattering he has taught me the importance of effective communication and inter–personal skills in the scientific world. In his words: *"Science is done by people, not a group of robots; so try to treat them that way. When you watch a talk remember they are people. Connect with them on a human level."*

I would also like to graciously acknowledge the members of my Ph.D. committee, Lecturer Michael Anderson, Professor Eric Fullerton, Professor Shirley Meng, and Professor Sunil Sinha for their support in my academic efforts and willingness to provide their time and feedback.

I would like to thank Mike specifically for all of his advice over the years about my career pursuits. With his encouragement I've realized my desire to pursue a career in teaching and physics education research. His insights into the teaching process have helped me to be a more thoughtful and conscientious educator.

The work done herein was aided by the contributions of many people over the past several years whose expertise and guidance was essential to its success. Specifically, I'm grateful for the mentorship Binhua Lin has provided both at the beamline and during the writing process. She's spent many hours during beamtime teaching me all about the nuances of the experimental design and data collection. She always made sure that we were well fed and getting enough sleep while at APS.

I want to thank Mati Meron for his patience with all of my emails, day and night, about IDL analysis, data interpretation and all other technical aspects of the project. He had an answer for everything. His wisdom and encouragement

gave me confidence to move forward when I found myself unsure about my results - always friendly and always willing to talk with me.

Thanks to all of the members of the Shypyrko group for making work feel a lot less like work and for the company they provided during late nights spent at the beamline. In particular, I want to thank Leandra Boucheron and Yeling Dai for not only being valuable colleagues from whom I learned a great deal, but also for their indelible companionship. Regardless of where the future takes us, I hope to keep in touch with both of you. I wish you all the best.

My thanks to all of the friends I've made here in San Diego, graduate students and otherwise, with whom I could commiserate about the trials of graduate school. Your friendship has made UCSD a welcoming community for me.

I feel extremely fortunate to have had such a loving and supportive family. They raised me well and taught me the importance of persistence and hard work, without which I would not have made it this far.

Lastly, I want to thank Bill Nye the Science Guy for introducing me to the world of science.

The text of Chapter 2, in part, is a reprint of material as it appears in: J. Stanley, Y. Dai, L. Boucheron, B. Lin, M. Meron, O. Shpyrko, "Novel comparison of microscopy and diffraction techniques on the structure of iron oxide nanoparticle monolayers transferred by Langmuir-Schaefer method", *Review of Scientific Instruments*, (submitted for publication), 2014.

The text of Chapter 3, in part, is a reprint of material as it appears in: J. Stanley, L. Boucheron, Y. Dai, S. You, B. Lin, M. Meron, O. Shpyrko "Evolution of in–plane and out–of–plane structure of nanoparticle Langmuir monolayers under lateral compression", (in preparation), 2015.

The text of Chapter 4, in part, is a reprint of material as it appears in: J. Stanley, L. Boucheron, Y. Dai, S. You, B. Lin, M. Meron, O. Shpyrko "Evolution of in–plane and out–of–plane structure of nanoparticle Langmuir monolayers under lateral compression", (in preparation), 2015.

The text of Chapter 5, in part, is a reprint of material as it appears in: J. Stanley, L. Boucheron, B. Lin, M. Meron, O. Shpyrko , "Spontaneous phase separation during self-assembly in bi-dispersed metallic nanoparticle monolayers", *Applied Physics Letters*, (submitted for publication), 2014.

VITA

2007	B. A. in Mathematics *with Honors*, University of California, Santa Cruz
2007	B. S. in Physics *with Honors*, University of California, Santa Cruz
2011	M. S. in Physics, University of California, San Diego
2013 Summer	Instructor, *Physics 2C: Fluids, Waves, Thermodynamics, and Optics*, University of California, San Diego
2014 Summer	Instructor, *Physics 1A: Mechanics*, University of California, San Diego
2014 Summer	Instructor, *Physics 2C: Fluids, Waves, Thermodynamics, and Optics*, University of California, San Diego
2015	Ph. D. in Physics, University of California, San Diego

PUBLICATIONS

L. Boucheron, J. Stanley, Y. Dai, S. You, B. Lin, M. Meron, S. Narayanan, A. Sandy, Z. Jiang, O. Shpyrko "Jamming in Quasi-2D Self-Assembled Nanoparticle Monolayers", *Physical Review Letters*, (in preparation), 2015.

J. Stanley, L. Boucheron, Y. Dai, S. You, B. Lin, M. Meron, O. Shpyrko "Evolution of in–plane and out–of–plane structure of nanoparticle Langmuir monolayers under lateral compression", (in preparation), 2015.

J. Stanley, L. Boucheron, B. Lin, M. Meron, O. Shpyrko , "Spontaneous phase separation during self-assembly in bi-dispersed metallic nanoparticle monolayers", *Applied Physics Letters*, (submitted for publication), 2014.

J. Stanley, Y. Dai, L. Boucheron, B. Lin, M. Meron, O. Shpyrko, "Novel comparison of microscopy and diffraction techniques on the structure of iron oxide nanoparticle monolayers transferred by Langmuir-Schaefer method", *Review of Scientific Instruments*, (submitted for publication), 2014.

T. Saerbeck, J. Pereiro, J. Wampler, J. Stanley, J. Wingert "Ferromagnetism in partially oxidized CuCl", *Journal of Magnetism and Magnetic Materials* **346**, 2013.

J. Stanley, F. Bridges "Degradation and rejuvenation studies of AC electroluminescent ZnS:Cu,Cl phosphors", *Journal of Physics: Condensed Matter* **22**, 2010.

ABSTRACT OF THE DISSERTATION

Structural Studies of Liquid Surface Self-Assembled Iron Oxide Nanoparticle Monolayers

by

Jacob Stanley

Doctor of Philosophy in Physics

University of California, San Diego, 2015

Professor Oleg Shpyrko, Chair

The phenomenon of self–assembly has become increasingly relevant due to the role it can play in nanofabrication and the emergence of macro–scale structure. This phenomenon has been seen in a broad range of material systems. For example, iron oxide nanoparticles undergo self-assembly into well-ordered monolayer films of macroscopic size at an air-water interface. It is this system that is the topic of the work herein. The self–assembly process is the result of the van der Waals forces between the constituent particles. For roughly spherical particles the monolayer is a 2D hexagonal close packed lattice. Using a variety of X-Ray scattering techniques including Grazing Incidence X-Ray Diffraction (GID), X-Ray Reflectivity (XR), and Grazing Incidence X-Ray Off-Specular Scattering (GIXOS) the struc-

ture of some of the emergent characteristics of these films is studied. Namely, the microscale multilayering that occurs when these films are laterally compressed, exhibits varying morphologies which depend on the size of the constituent particles. Additionally, when these films are formed from bi–dispersed mixtures containing 10 and 20 nm particles, the particles phase separate into well–ordered patches during the self–assembly process. The domain sizes of these phase separated regions are at most a factor of 2-3 times smaller than that of a film comprising only mono–dispersed particles, and their degree of disorder is comparable. Finally, using these iron oxide nanoparticle monolayers as a test system, a novel analysis is demonstrated that allows a direct comparison between Scanning Electron Microscopy (SEM) of ex-situ films and GID measurements of in-situ films: the results demonstrate that structural information comparable to that contained in the GID measurements can be obtained by Fourier transform analysis of the SEM images taken of the film after it has been transferred to a silicon substrate. Furthermore this comparison suggests that the Langmuir-Schaefer method of transferring the liquid surface film to a solid substrate preserves the average hexagonal structure and inter-particle spacing of the film.

Chapter 1

Introduction

The advent of nanoscale fabrication has opened up an extensive field of scientific and technological possibilities. The ability to synthesize nanoscale building blocks of various sizes, morphologies, and chemical compositions, provides access to a myriad of novel electrical, photonic, mechanical, and magnetic characteristics. The micro– to macro–scale composite materials formed from such nanoscale building blocks exhibit emergent properties that are the result of the fundamental characteristics of their constituents.

Of course the synthesis is but one facet of nanoscale science. All manner of experimental techniques have been implemented in understanding and characterizing the structures assembled from such nanoscale building blocks. One of the most widely used experimental methods is the use of monochromatic X-Rays to probe the structural arrangements of such samples comprising nanoscale structures. The large penetration depth and short wavelength make X-Rays ideal for probing such nanoscale systems made of high-Z materials.

This dissertation describes experimental efforts to study the structure of a specific system assembled from a particular nanoscale building block, using a range of different X-Ray scattering techniques. The remainder of this chapter provides background on the sample, sample preparation and X-Ray techniques utilized in the structural studies.

1.1 System of Interest

The system studied herein is an ultra-thin film comprising approximately spherical iron oxide nanoparticles which has been formed at an air-water interface. The characteristics of the film are varied by changing the density, lateral compression, nanoparticle size and distribution.

1.1.1 Iron Oxide Nanoparticles

In the past 10-15 years improved nanoparticle synthesis has lead to a great deal of new studies utilizing several different types of iron oxide (predominantly maghemite, $\gamma - Fe_2O3$, or magnetite, Fe_3O_4). These nanoparticles typically range in size from 5-20 nm in diameter. Though they have been fabricated with larger sizes (40-50 nm), the size and shape uniformity is not well maintained as the particle size increases. Magnetite nanoparticles in particular are promising given their biocompatibility, and thus potential for use in biomedical applications. They are found naturally occurring in bacteria as well as animal species. [2–5]

With an appropriate surface coating/capping these magnetic nanoparticles can be dispersed into a variety of organic solvents, forming a uniform suspension. This is commonly referred to as a ferro-fluid and has been the topic of study as a bulk fluid with a range of different concentrations and particle sizes. [2–5] For this work the nanoparticles were coated in a oleic acid ligand of approximately $1 - 2$ thickness and were dispersed into chloroform, $CHCl_3$, to a low concentration of approximately $0.5\,\mathrm{mg/mL}$. These solutions were made for two different particle sizes: 10 and 20 nm diaemter (Figure 1.1). The particles were purchased from Ocean Nano Tech (www.oceannanotech.com) in a powder form, having already been coated in oleic acid. The nanoparticles have a polydispersity of less than 5% the particle size.

1.1.2 Self-Assembly

Self-assembly is a process in which a collection of components form into an organized structure as a result of local interactions between the individual com-

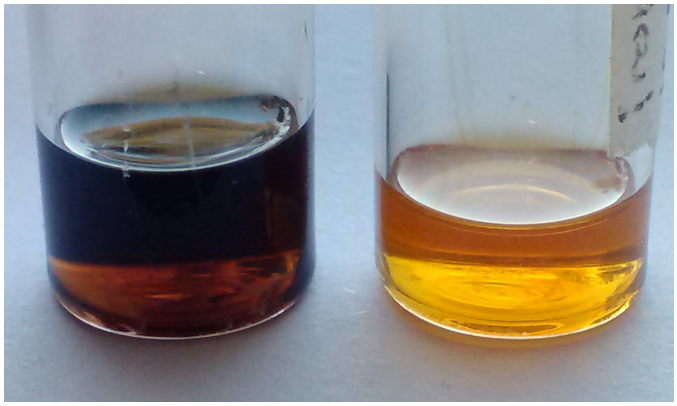

Figure 1.1: A photo of the two particle suspensions, with the 20 nm solution on the left and 10 nm solution on the right. They have equal mass concentration of 0.5 mg/mL; the difference in color is due to the differing particle size.

ponents themselves. By definition no externally driven global interactions/forces are involved in the assembly process, yet self-assembly frequently results in long range order. In other words, the weak/local nature of the interaction implies that as long as the components of the system are in close proximity then self-assembly is a spontaneous process.

Self-assembly is distinct from chemical bonding in three primary ways: 1.) the self-assembly results in a higher order structure than the individual components; 2.) self-assembly is caused by weaker interactions (such as van der Waals, hydrogen bond, capillary) than those responsible for chemical bonding (ionic, covalent, metallic, etc.); 3.) the range of building blocks includes a wide range of nano– and meso–scale structures having various shapes and compositions, in contrast to chemical bonds which involve atoms and small molecules.

A consequence of these features is the thermodynamic stability of the resulting self-assembled system. Since the process takes place without external forces it must be a lower Gibbs free energy for the system.

1.1.3 Particle Interactions

The primary interaction driving self-assembly for iron oxide nanoparticles is an attractive van der Waals force that close packs the particles and a repulsive

steric interaction. [6–8] For a spherical particle the van der Waals interaction energy between two identical spheres is given by [7, 9, 10]

$$V_{vdW}(\delta) = -\frac{A}{12}\left[\frac{R}{\delta\left(1+\frac{\delta}{4R}\right)} + \frac{1}{1+\frac{\delta}{R}+\frac{\delta^2}{4R^2}} + 2\ln\left(\frac{\delta\left(1+\frac{\delta}{4R}\right)}{R\left(1+\frac{\delta}{R}+\frac{\delta^2}{4R^2}\right)}\right)\right] \tag{1.1}$$

where $r = 2R + \delta$ is the spacing between particle centers, with R being the particle radius and δ being the inter–surface distance. Also, A is the Hamaker coefficient for an iron oxide sphere which has been calculated as being $A = 33 - 68\,\mathrm{zJ}$. [11, 12] This value is dependent on the particle environment due to the dialectric response of the medium surrounding it - the lower value corresponding to a vacuum environment and the higher corresponding to water. In the case of iron oxide at the air-water interface an intermediate value would be expected. For particles on the order of 10-20 nanometers in diameter the contribution to the Hamaker constant from magnetic dispersion is less than 10%, which only becomes significant when the dialectric response of the medium is similar to that of the nanoparticle. [12]

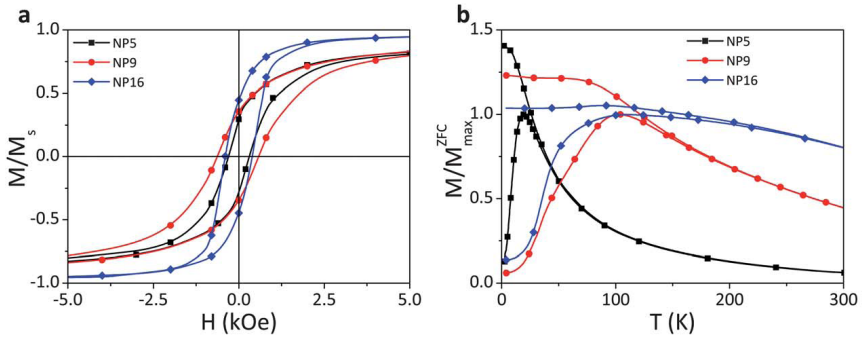

Figure 1.2: (a) Magnetization as a function of applied field at 5 K and (b) the ZFC/FC curves measured in a 75 Oe field for three different sizes of iron oxide nanoparticle. This figure is a reproduction from reference [1].

The magnetic moment per unit volume for the iron oxide nanoparticles are exceptionally large. [1, 3, 13] The magnetization as a function of applied field and the maximum magnetization as a fucntion of temperature are shown in Figure 1.2. The saturation magnetization measured for 16 nm particles is $m_s = 7.3 \times 10^4\,\mu_B$ where $\mu_B = e\hbar/2m_e = 5.79 \times 10^{-5}\,\mathrm{eV/T}$ is the Bohr magneton.

In addition to the van der Waals interaction iron oxide nanoparticles have a magnetic dipole–dipole interaction. [14] Depending on the geometry of the particles and the application of external magnetic fields, this dipole–dipole interaction can lead to a range of self-assembled structures not seen in non–magnetic self–assembled systems. [15–17] The general dipole–dipole energy between two dipole moments $\mathbf{m_1}$ and $\mathbf{m_2}$ separated by $\mathbf{r}$ is given by

$$V_{mag}(\mathbf{r}, \mathbf{m_1}, \mathbf{m_2}) = -\frac{\mu_0}{4\pi r^3}\left[3(\mathbf{m_1}\cdot\hat{\mathbf{r}})(\mathbf{m_2}\cdot\hat{\mathbf{r}}) - \mathbf{m_1}\cdot\mathbf{m_2}\right] \tag{1.2}$$

If the interacting particles are located at the air–water interface and a constant magnetic field is applied normal to the surface, strong enough to saturate the magnetization of the nanoparticles then the dipole–dipole interaction becomes repulsive, given by

$$V_{mag}(r) = \frac{\mu_0}{4\pi}\frac{m_1\, m_2}{r^3} = \frac{\mu_0}{4\pi}\frac{m_s^2}{r^3} = (5.3\times 10^9)\frac{\mu_0\mu_B}{4\pi r^3} \tag{1.3}$$

The total interaction energy for neighboring particles is the sum of the three contributions.

$$V_{tot}(\mathbf{r}, \mathbf{m_1}, \mathbf{m_2}) = V_{vdW}(r) + V_{steric}(r) + V_{mag}(\mathbf{r}, \mathbf{m_1}, \mathbf{m_2}) \tag{1.4}$$

The interparticle distance is going to be determined by the minimization of this total energy. Depending on the orientation of the magnetic moments of the pairwise particles the contribution from the dipole–dipole interaction can either be attractive or repulsive.

1.1.4 Film Formation (Drop-Casting)

To assemble the film on the air-water interface we use a process known as drop-casting. It consists of depositing a small volume of nanoparticle solution onto the interface and then allowing the solvent to evaporate off, leaving behind the previously suspended nanoparticles. [18] Self-assembly occurs most rapidly during the evaporation. The final assembly is highly sensitive to the degree of dewetting of the solvent. However, chlorofom on water experiences very low dewetting and very rapid evaporation, which improves the uniformity of the resulting film.

1.2 Langmuir-Blodgett Trough

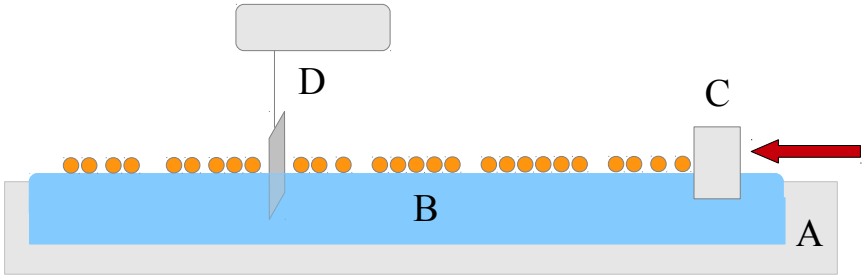

Figure 1.3: Diagram of a Langmuir-Blodgett trough (side view). Includes A.) trough body, B.) water subphase, C.) moveable barrier, and D.) Wilhelmy plate and electrobalance for monitoring surface pressure. The particle film is depicted suspended on surface.

A Langmuir-Blodgett trough was used to support/contain the film during the experiments. The Langmuir-Blodgett trough, first utilized by Irving Langmuir in 1917, is a shallow open topped container with a large surface area. The trough The trough is filled with high-purity water. It's predominantly used to study monolayer films formed from hydrophilic or amphilic materials. This is achieved by spreading the amphilic material over the water surface, allowing it to equilibrate until it forms a sufficiently uniform monolayer, then laterally compressing the monolayer with motor controlled barriers that subtend the liquid surface.

The purpose of the water is to act as a substrate (also referred to as the subphase) on which the monolayer of interest is supported. The benefit of a liquid substrate over a solid one, like silicon, is two fold: 1.) the monolayer does not adhere to the liquid surface as it would to a solid substrate, thereby allowing for mobility of the monolayer and 2.) the liquid surface typically has lower surface roughness than a solid substrate (providing sufficient vibration isolation is being used) so the monolayer is less disrupted.

A diagram of the trough set-up can be seen in Figure 1.3. The teflon barrier (part C in the figure) controls the only tunable global parameter - surface area

available to the film. The two macroscale parameters that are monitored during the experiment are the surface area (as determined by the barrier position) and the in–plane surface pressure. The later is monitored by the Wilhelmy Plate and microbalance set–up (part D in Figure 1.3). These global parameters compliment the local structural measurements made using X-Rays.

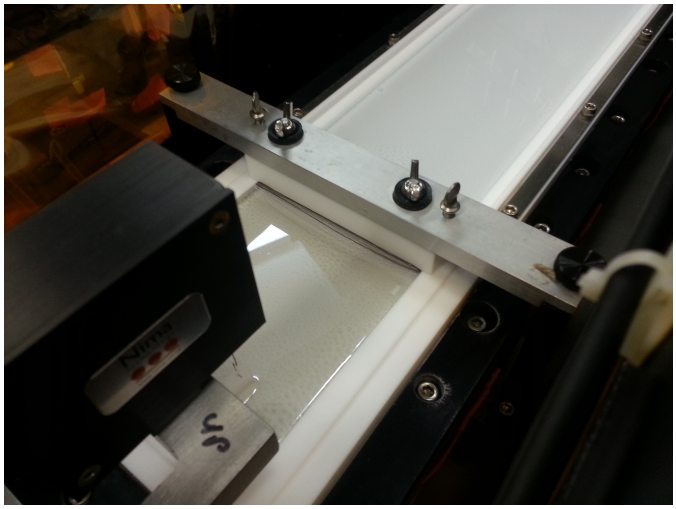

Figure 1.4: Langmuir-Blodgett trough located at APS Sector 15 which was used for all the data contained herein. The barrier (visible) has fully compressed the film.

All measurements were made using the Langmuir-Blodgett trough at Sector 15 at Argonne's Advanced Photon Source. A picture of this set-up can be seen in Figure 1.4. The pressure sensor is visible in the bottom left corner and the motor controlled barrier is shown having fully compressed the film. The current barrier position corresponds to full compression. The film region on which the X-Ray problem is incident is approximately halfway between the wilhelmy plate and the barrier position.

1.2.1 Wilhemy Plate Pressure Sensor

The Wilhelmy plate is a thin rigid plate that is used to measure the interfacial tension at the air-water interface. The plate is oriented perpendicular to the liquid surface at such a height that it subtends the interface. The liquid surface

then forms a contact angle θ with the plane of the Wilhelmy plate. The vertical force acting on the plate is measured by a sensitive microbalance to which the plate is attached (as shown in Figure 1.3. A detailed diagram of the Wilhelmy plate and its physical parameters can be seen in Figure 1.5.

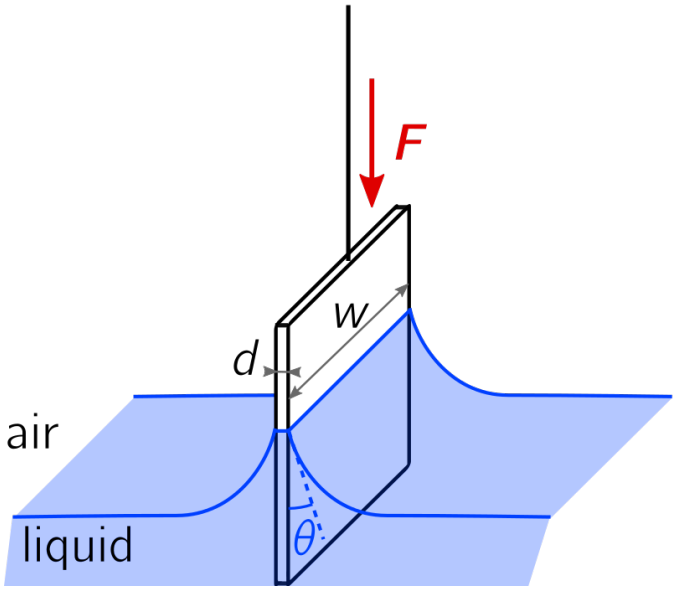

Figure 1.5: Detail of the Wilhelmy plate, including all the physical parameters, as it subtends the liquid surface.

The force measurement recorded by the micro–balance is given by

$$F_{total} = F_g - F_B + F_{tension} \tag{1.5}$$

where F_g is the force of gravity, F_B is the buoyant force, and $F_{tension}$ is the force due to the surface tension. Assuming the plate's orientation is stable throughout the measurement, the forces due to gravity and the buoyant force will remain constant. This systematic offset can be accounted for in the calibration of the balance.

The force due to surface tension ($F_{tension}$) is directly related to the surface tension of the interface γ as well as the size of the plate and the contact angle θ. Specifically, γ is equivalent to

$$\gamma = \frac{F_{tension}}{L \cos\theta} \tag{1.6}$$

where L is the total perimeter of the plate at the point it intersects the interface. γ is the total surface tension, which depends on both the liquid comprising the subphase and the type of material suspended on the surface. The surface pressure of the film is the physical parameter of interest and it is related to the total surface tension. It is given by

$$\Pi = \gamma_0 - \gamma \tag{1.7}$$

where γ_0 is the surface tension of the pure subphase. In the case of water $\gamma_0 = 72.0\,\mathrm{mN/m}$. The surface pressure Π ([mN/m]) can be interpreted as the as the force exerted by the monolayer film directly on the teflon barrier, per unit length.

In order to calibrate the pressure sensor apparatuses to directly measure the surface pressure Π the trough is filled and the Wilhelmy plate is put in place prior to the deposition of the monolayer. The micro–balance is then zeroed and the barriers are opened and closed to check for impurities on the liquid surface. If the pressure does not change as the barriers are moved then the surface is sufficiently clean. At this point no additional water can be added to the subphase as it will alter the buoyant force. Now the monolayer can be added to the surface and the micro–balance will directly measure Π.

With the film deposited the barriers compress the film which will increase the surface pressure. The isotherm of the film is a plot of the film's pressure as a function of the area. An example of this for a film comprising 20 nm iron oxide nanoparticles can be seen in Figure 1.6.

Given the Wilhelmy plate's large size, relative to the constituents of the monolayer, its measurement can be considered a global measure of the surface pressure. However, this assumes the monolayer is in equilibrium, which is not always the case.

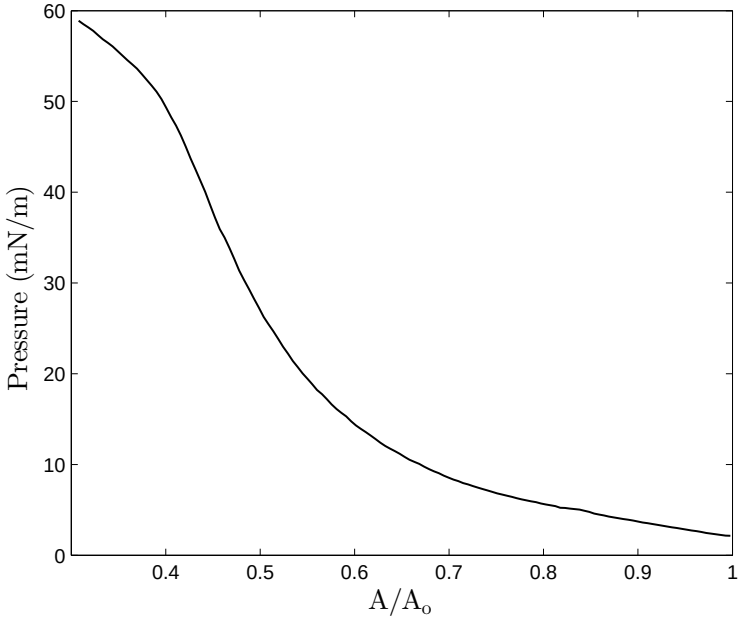

Figure 1.6: Characteristic isotherm for an iron oxide nanoparticle film during continuous compression.

1.3 X-Ray Interaction with Matter

When electromagnetic waves interact with matter the primary interaction is directly with the electrons. There are weak interactions with the nuclear and electronic spins but this effect is negligible when compared to that between electric field and the electronic charge, for most cases. When a a single photon interacts with an atom one of three things can occur: 1.) the photon is elastically scattered, 2.) it is inelastically scattered, or 3.) it is absorbed. In the case of elastic scattering, the energy of the photon is conserved while momentum may be transferred to or from the electrion/atom. In the case of inelastic scattering or absorption part or all of the energy possessed by the photon is transferred to the electron/atom. The processes associated with these two is typically on the order of 1-100 eV (ignoring the energy of K,L,M-shell absorption edges for larger Z atoms). Thus when using X-Rays on the order of 10 keV for scattering the contribution from these inelastic processes can be neglected and the measurements can be approximated as an elastic Thomson scattering process. The entirety of the discussion herein makes

this assumption.

1.3.1 Complex Refractive Index

The refractive index has its roots in the manner of the interaction between the photons and the electrons within the material. First consider a free electron being acted on by an oscillating electric field - its position is given by

$$\mathbf{x}(\omega) = -\frac{e}{m_e\omega^2}\mathbf{E}(\omega) \tag{1.8}$$

where any interaction between the electron and the nucleus is being neglected. The polarization of a material comprising such atoms experiencing the aforementioned electric field is

$$\mathbf{P}(\omega) = \left(eN_A\sum_j \frac{\rho_j f_j^0}{A_j}\right)\mathbf{x}(\omega) \tag{1.9}$$

where N_A is Avogadro's number, ρ_j is the mass density of atom j having atomic weight A_j and atomic form factor f_j^0.

For most atoms the outer shell electrons have resonant energies much lower than the energy of a typical X-Ray used in scattering experiments, thus these electrons can be approximated as free electrons. On the other hand, the inner shell electrons are far more tightly bound, i.e. the K,L,M-shell ionization energies are on the order of 10's of keV - greater than the X-Ray energy. Therefore these inner shell electrons only weakly interact with the incident electric field. Furthermore the outer shell electrons have the effect of screening the inner shell electrons which results in a reduced scattering length, denoted by $f'(\omega)$. Additionally, the electron-electron interactions result in a phase lag in the electrons' response to the electric field. This can be described by a term $if''(\omega)$, which results in absorption. Thus the atomic form factor in equation can be modified to include these corrections.

$$f_j(\omega) = f_j^0 + f_j'(\omega) + f_j''(\omega) \tag{1.10}$$

From equations 1.8 and 1.3.1 one can write the dielectric constant as follows

$$\varepsilon(\omega) = \varepsilon_0(1+\chi_e) = \varepsilon_0\left(1+\frac{\mathbf{P}(\omega)}{\varepsilon_0\mathbf{E}(\omega)}\right) \tag{1.11}$$

$$= \varepsilon\left(1 - r_e\frac{\lambda^2 N_A}{\pi}\sum_j \frac{\rho_j f_j}{A_j}\right) \tag{1.12}$$

where $r_e = e^2/(4\pi\varepsilon_0 m_e c^2) = 2.81794 \times 10^{-15}\,\mathrm{m}$ is the Thomson scattering length of the electron and $\lambda = 2\pi c/\omega$ is the X-Ray wavelength.

X-Rays, like any other electromagnetic wave, undergo refraction which is related to the dielectric constant. Specifically $n = c/v = \sqrt{(\varepsilon\mu)/(\varepsilon_0\mu_0)}$. If one assumes a non-magnetic material ($\mu/\mu_0 \approx 1$) and the frequency of the X-Ray radiation is much larger than the atomic resonant frequencies then the refractive index can be expressed as

$$n(\mathbf{r},\omega) = 1 - \delta(\mathbf{r},\omega) + i\beta(\mathbf{r},\omega) \tag{1.13}$$

where δ and β are, with respect to the terms in equation 1.12, given by

$$\delta(\mathbf{r},\omega) = r_e \frac{\lambda^2 N_A}{2\pi} \sum_j \frac{\rho_j(\mathbf{r})}{A_j} \left(f_j^0 + f_j'(\omega)\right) \tag{1.14}$$

$$\beta(\mathbf{r},\omega) = r_e \frac{\lambda^2 N_A}{2\pi} \sum_j \frac{\rho_j(\mathbf{r})}{A_j} f_j''(\omega) \tag{1.15}$$

Finally, if the sample is a mono-species, homogeneous material (i.e. $\rho(\mathbf{r}) = \rho_0$) and the X-Ray energy is far from the atomic resonance, the refractive index can be simplified to

$$n = 1 - \frac{\lambda^2}{2\pi} r_e \rho + i\frac{\lambda}{4\pi}\mu \tag{1.16}$$

where μ is the absorption length. [19] For visible light the real part of the index is larger than one and can vary considerably depending on the material. On the other hand, for X-Rays the real portion of the index of refraction does not vary much from unity.

For most materials δ is between 10^{-5} and 10^{-8}, for X-Rays. Since δ is positive this means the real part of n is less than unity and therefore the phase velocity c/n inside the material is greater than the speed of light in vacuum. If we consider a plane wave propagating through a medium of complex index of refraction n then it can be rewritten as

$$E(k,z) = e^{inkz} = e^{i(1-\delta+i\beta)kz} = e^{i(1-\delta)kz} e^{-\beta kz} \tag{1.17}$$

The complex term, β is typically several orders of magnitude smaller than δ. Here it is clear that it has the effect of attenuating the wave, as discussed. For magnetite

(Fe_3O_4) and an X-Ray wavelength of $\lambda = 1.239$ the index is given by $\delta = 1.56\times10^{-5}$ and $\beta = 9.74 \times 10^{-7}$. This corresponds to a absorption length of approximately $510\,\mu$m, therefore a single 20 nm particle monolayer will not substantially absorb the incident X-Rays.

1.3.2 Differential Scattering Cross-Section

The fundamental quantity of interest in any scattering experiment is the differential scattering cross-section ($\mathrm{d}\sigma/\mathrm{d}\Omega$) which can be thought of as the fraction of radiation that's scattered into some solid angle at some orientation relative to the incident radiation. Mathematically, it is defined as

$$\left(\frac{\mathrm{d}\sigma}{\mathrm{d}\Omega}\right) = \frac{I_{scatt}}{\Phi_0\,\Delta\Omega} \tag{1.18}$$

where Φ_0 is the incident beam flux and I_{scatt} is the number of scattered photons per second collected at the detector which subtends a solid angle $\Delta\Omega$. This can be expressed in terms of the amplitude of the incident and radiated electromagnetic field as

$$\left(\frac{\mathrm{d}\sigma}{\mathrm{d}\Omega}\right) = \frac{|\mathbf{E}_{scatt}|^2R^2}{|\mathbf{E}_0|^2} = \frac{I_{scatt}R^2}{I_0} \tag{1.19}$$

The general expression for the differential scattering cross-section for X-Rays scattering from an electronic density $\rho(\mathbf{r})$ can be expressed in terms of the auto-correlation function of the electronic density, $\langle\rho(\mathbf{r})\rho(\mathbf{r'})\rangle = \langle\rho(\mathbf{r}-\mathbf{r'})\rho(0)\rangle$, as follows [20]

$$\frac{\mathrm{d}\sigma}{\mathrm{d}\Omega} = V\left(\frac{e^2}{mc^2}\right)^2\int\langle\rho(\mathbf{r})\rho(\mathbf{r'})\rangle e^{i\mathbf{q}\cdot(\mathbf{r}-\mathbf{r'})}\mathrm{d}(\mathbf{r}-\mathbf{r'}) \tag{1.20}$$

where V is the scattering volume. The density ρ depends on the geometry of the sample. In the subsequent sections a more specific expression for the differential scattering cross section will be described.

1.4 X-Ray Scattering Geometry

X-Ray scattering is a class of experimental techniques that are characterized by the resultant change in the momentum and energy of the X-Ray photons after

they have interacted with the sample of interest. In general each X-Ray photon is initially defined by some momentum, $\mathbf{k}_i$, and energy, ω_i. Once having interacted with sample the final energy and momentum are given by $\mathbf{k}_f$ and ω_f, respectively. Any change in energy or momentum must be transferred to the sample. Because

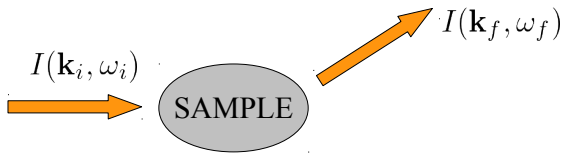

Figure 1.7: A basic schematic of a generalized scattering experiment.

of this it is useful to define the momentum transfer vector, $\mathbf{q}$, as follows:

$$\mathbf{q} = \mathbf{k}_f - \mathbf{k}_i \tag{1.21}$$

Scattering experiments consist of measuring the intensity of scattered light as a function of the photons' change in momentum and energy (Figure 1.7) in order to extract information about the sample. The X-Ray techniques used herein are all approximately elastic scattering where there is no exchange of energy with the sample. This reduces the dimensionality of the the problem by one since there is no longer a frequency dependence of the scattered photons, i.e. $\Delta\omega = \omega_f - \omega_i = 0$ and thus $|\mathbf{k}_i| = |\mathbf{k}_f| = k = 2\pi/\lambda$. Therefore the scattered intensity is only a function of the momentum transfer, $\mathbf{q}$. [21]

In this work three X-Ray techniques are utilized: Grazing Incidence X-Ray Diffraction (GID), X-Ray Reflectivity (XRR), and Grazing Incidence X-Ray Off-Specular Scattering (GIXOS). All three of these are done with reflection geometry and therefore can be described with the same parameters. These techniques are implemented in surface scattering and thus the geometric parameters are defined with respect to the plane of the surface. Specifically the angle between the incident X-Rays and the sample plane (labeled α), the angle between the scattered X-Rays and the plane (labeled β), and finally the angle between the scattered X-Rays and the plane formed by the incident X-Rays and the normal to the sample

surface (labeled $\phi = 2\theta$). [19] This geometry can be seen in Figure 1.8. This geometric description is advantageous as it conforms to the detector and X-Ray beam movements of most X-Ray scattering apparatus.

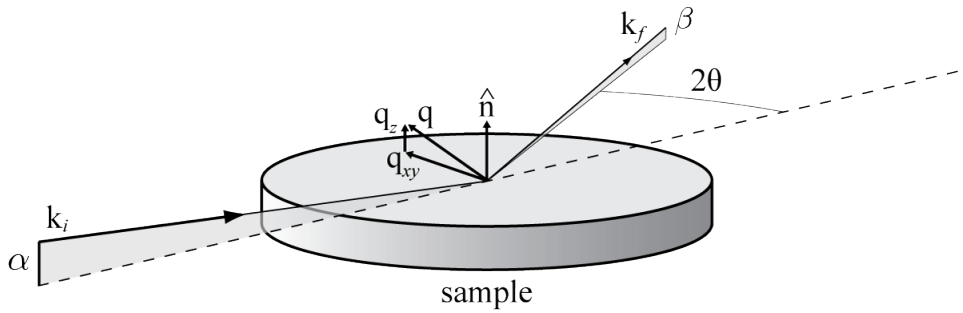

Figure 1.8: Schematic of reflection geometry used for the different scattering techniques. This geometry is fully described by three angles: α, β, and θ. From these the in–plane and out–of–plane components of the momentum transfer vector.

Due to the planar geometry of the sample it is advantageous to separate $\mathbf{q} = (q_x, q_y, q_z)$ into components parallel and perpendicular to the sample surface. The q_x and q_y components lay within the sample plane thus we define $q_{xy} = \sqrt{q_x^2 + q_y^2}$, which is the total momentum transfer in the plane of the file. q_z is the totall momentum transfer normal to the surface. The incident and scattered momentum vectors (and subsequently $\mathbf{q}$) can be written in terms of the angles $\alpha, \beta, \phi(= 2\theta)$ as follows:

$$\mathbf{k}_i = k(0, \cos\alpha, -\cos\alpha) \tag{1.22}$$

$$\mathbf{k}_f = k(-\cos\beta\sin\phi, \cos\beta\cos\phi, \sin\beta) \tag{1.23}$$

$$\mathbf{q} = \mathbf{k}_f - \mathbf{k}_i = k(-\cos\beta\sin\phi, \cos\beta\cos\phi - \cos\alpha, \sin\beta + \cos\alpha) \tag{1.24}$$

From this definition of $\mathbf{q}$ the magnitudes of the in–plane and out–of–plane components can be calculated:

$$q_{xy} = k\sqrt{4\sin^2\left(\frac{\beta+\alpha}{2}\right)\sin^2\left(\frac{\beta-\alpha}{2}\right) + 4\cos\alpha\cos\beta\,\sin^2\left(\frac{\phi}{2}\right)} \tag{1.25}$$

$$q_z = 2k\sin\left(\frac{\beta+\alpha}{2}\right)\cos\left(\frac{\beta-\alpha}{2}\right) \tag{1.26}$$

The scattering problem then comes down to measuring the scattered intensities as a function of q_{xy} and q_z. This formalism is sufficient to describe all forms of reflection scattering. Further simplification can be made for the various specific techniques as will be discussed in the next section.

1.4.1 Grazing Incidence

The refraction of X-Rays is described by Snell's law much in the same manner as visible light, satisfying

$$\cos\alpha = n\cos\alpha' \tag{1.27}$$

where α' is the refracted angle in the medium of index n. As stated in section 1.3 the real part of the index of refraction is slightly smaller than unity. Thus, unlike visible light, X-Rays can undergo total *external* reflection, which occurs when $\alpha' = 0$. The incident angle at which this occurs is called the critical angle, $\alpha = \alpha_c$. *Grazing incidence* is defined as an incident angle α that is less than the critical angle (α_c) of the subphase. The critical angle is approximately given by

$$\alpha_c = \sqrt{2\delta} = \frac{\sqrt{4\pi\rho r_e}}{k} \tag{1.28}$$

where δ is from the real part of the index of refraction (eq. 1.13), which is related to the electron denisty ρ, and the Thompson scattering length r_e . [21] In the case of water the critical angle is approximately $\alpha_c = 0.15°$ for a X-Ray wavelength of $\lambda = 1.239\,\text{Å}$.

When the angle is less than the critical angle ($\alpha < \alpha_c$) the total external reflection is accompanied by an evanescent wave within the refracting medium which propagates parallel to the interface and dies off exponentially into the material without being absorbed. In this way the subphase does not contribute much to the attenuation of the incident beam. That the reflected X-Rays do not pass very far into the subphase makes grazing incidence scattering extremely surface sensitive. This is ideal for studying these thin monolayer films. [19]

1.4.2 Liquid Surface Scattering

Unlike solid interfaces, liquid surfaces experience dynamic capillary fluctuations, that can be described as small height variations about the average surface location as a function of the in–plane position, $z(\mathbf{r}_{xy}) = \bar{z} + \delta z(\mathbf{r}_{xy})$. These height fluctuations can be described by their statistical average. [22] Even for surfaces well isolated from mechanical vibrations these capillary fluctuations can be thermally excited. In the case of thermally excited fluctuations, Sinha et al. [23] have demonstrated that the effects of these surface fluctuations on the scattering intensity (as a function of q_{xy} and q_z) by the following integration results

$$\int_{r_{xy}>\zeta} e^{-\frac{q_z^2}{2}\langle[z(\mathbf{r}_{xy})-z(0)]^2\rangle} e^{i\mathbf{q}_{xy}\cdot\mathbf{r}_{xy}}\,\mathrm{d}\mathbf{r}_{xy} = \frac{1}{q_m^{\eta}}\frac{4\pi^2}{q_{xy}^{2-\eta}} \tag{1.29}$$

where $\eta = \frac{k_B T}{2\pi\gamma} q_z^2$ is the capillary exponent. The lower cutoff length ζ for the bounds of integration is the correlation length of the bulk subphase, and $q_m = \pi/\zeta$. For fluctuations at this length scale or smaller one is not able to separate those occurring in the subphase bulk and those on the surface. However, most thermal capillary fluctuations are of wavelengths much larger than ζ, therefore the excluded integration range results in a small error. Therefore equation 1.29 can be used to express the total differential scattering cross section (equation 1.20) for a liquid surface as [20, 22–26]

$$\frac{\mathrm{d}\sigma}{\mathrm{d}\Omega} = \frac{A_0}{k^2 \sin\alpha \sin\beta}\left(\frac{q_c}{2q_z}\right)^4 \frac{\eta q_z^2}{8\pi}|\Phi(q_z)|^2|T_i|^2|T_s|^2\frac{1}{q_{xy}^2}\left(\frac{q_{xy}}{q_m}\right)^{\eta} \tag{1.30}$$

where I_0 is the initial X-Ray intensity, A_0 is the area of the incident X-Ray beam, $k = 2\pi/\lambda$ is the magnitude of the momentum transfer vector, γ is the surface tension, and T_i and T_s are the incident and scattered Fresnel transmission coefficients for an air-water interface. Finally, the thermal structure factor $|\Phi(q_z)|^2$ is defined in terms of the the average electronic density along the surface normal as

$$|\Phi(q_z)|^2 = \frac{1}{\rho_\infty}\int \frac{\mathrm{d}\langle\rho(z)\rangle}{\mathrm{d}z}\, e^{iq_z z}\,\mathrm{d}z \tag{1.31}$$

where ρ_∞ is the bulk subphase density. In this manner the capillary contributions are separated from the specular reflection.

1.5 X-Ray Techniques

The three X-Ray techniques used herein focus specifically on either in–plane or out–of–plane film structure, thus they focus on different features of the scattering signal. In this section I describe each technique and how it applies to the system of interest.

1.5.1 X-Ray Reflectivity (XRR)

When EM radiation is incident on an interface between two media of differing indicies of refraction some portion of that radiation is reflected and some of it transmitted. Using the geometric description in Figure 1.8, if the reflected angle β is equal to that of the incident angle α (with $\theta = 0$) this is referred to as a *specular reflection*. By measuring the specular reflection as a function of the reflected angle one can obtain information about the nature of the media. Specular reflection can be expressed as a function of q_z (equation 1.26) which is simplified to

$$q_z = 2k \sin\left(\frac{\alpha + \alpha}{2}\right) \cos\left(\frac{\alpha - \alpha}{2}\right) = 2k \sin\alpha \tag{1.32}$$

If the interface is a sharp, well-defined boundary then the reflected intensity as a function of q_z is given by the *Fresnel reflectivity* equation for intensity

$$R_F(q_z) = |r(q_z)|^2 = \left|\frac{q_z - \sqrt{q_z^2 - q_c^2}}{q_z + \sqrt{q_z^2 - q_c^2}}\right|^2 \approx \left(\frac{q_c}{2q_z}\right)^4 \tag{1.33}$$

where q_c is the q_z value at the critical angle.

More generally, if the interface consists of a finite sized graded region with a electron density profile given by $\rho(z)$ (limits: $\rho \to 0$ as $z \to +\infty$ and $\rho \to 1$ as $z \to -\infty$) the total reflectivity from the interface can be obtained by first considering the contribution to the reflectivity $r(q_z)$ from an infinitesimal thin layer at a depth z, given by

$$\delta r(q_z) = -i\left(\frac{q_c^2}{4q_z}\right) \langle\rho(z)\rangle dz \tag{1.34}$$

To obtain the total reflectivity one must Integrate over all the infinitesimal thin slabs along the z-direction, while taking into account the change in phase of the

incident beam as a function of z. The phase is given by $e^{iq_z z}$ and thus the total reflectivity is

$$r(q_z) = -\int_{-\infty}^{\infty} i\left(\frac{q_c^2}{4q_z}\right)\langle\rho(z)\rangle e^{iq_z z}\mathrm{d}z \tag{1.35}$$

$$= \frac{1}{q_z}\left(\frac{q_c^2}{4q_z}\right)\int_{-\infty}^{\infty}\langle\rho'(z)\rangle e^{iq_z z}\mathrm{d}z \tag{1.36}$$

Finally, taking the square of the magnitude of this results in the total intensity reflectivity formula for a generalized interface with varying density along the z-direction. It is expressed as

$$R(q_z) = R_F(q_z)\cdot|\Phi(q_z)|^2 \tag{1.37}$$

where $R_F(q_z)$ is given by the approximation in equation 1.33 and $\Phi(q_z)$ is given by:

$$\Phi(q_z) = \frac{1}{\rho_\infty}\int\left\langle\frac{\mathrm{d}\rho(z)}{\mathrm{d}z}\right\rangle e^{iq_z z}\,\mathrm{d}z \tag{1.38}$$

This is what is known as the *Master-Formula*. [19, 20] Equation 1.37 allows one to relate the experimentally measured reflected intensity from an interface as a function of out of plane momentum transfer vector ($R(q_z)$) to the density profile of the said layer. The benefit of equation 1.37 is that it's valid for any analytic function of $\rho(z)$ given that it satisifies the appropriate limits. Given that $R(q_z)$ is the measured quantity, one cannot just simply invert equation 1.37 and solve for $\rho(z)$. Instead, a parameterized model must be assumed for $\rho(z)$, the integral and Fresnel reflectivity evaluated, and the resulting $R(q_z)$ compared to the experimental data. This process is then iterated and the parameters adjusted in an attempt to minimize some comparative metric, such as the residual sum of squares.

In the case of a layered interface (such as that studied in this work) a model consisting of some finite number of thin slabs is used for this process. Each slab is characterized by three parameters: an amplitude A_i, a thickness d_i, and an edge roughness σ_i. A frequently utilized function in this context is the error function

$$\rho_i(z) = A_i\,\mathrm{erf}\left(\frac{z-z_i}{\sqrt{2}\sigma_i}\right) \tag{1.39}$$

which can then be used to piecewise define the interface and whose derivative is in the form of a Gaussian, thus making for a straightforward evaluation of

reflectivity. [27] Herein, the data was fit in this manner using CPLOT for the iterative minimization and a standard reflectivity fitting program.

1.5.2 Grazing Incidence X-Ray Diffraction (GID)

In a GID experimental set-up the incident X-Ray beam is directed at the surface below its critical angle and the detector moves through a plane parallel to that of the sample surface. The angle β at which the detector is placed is small, close to that of the incident angle. In this way GID measures the variation in the intensity of scatter as a function of ϕ and therefore q_{xy}. This is done to diffract from lattice planes that are perpendicular to the sample surface. [28]

In the case of the nanoparticle monolayers, if lattice order exists in the film then there will be corresponding Bragg planes whose plane spacing is related to the size of the nanoparticle constituents. The angular locations of the Bragg peaks corresponding to these planes are given by the familiar Bragg's law

$$n\lambda = 2d\sin\theta \tag{1.40}$$

where d is the Bragg plane spacing, λ is the X-Ray wavelength, and $theta$ is the scattering angle at the Bragg peak.

For α and β small compared to ϕ ($\alpha, \beta << \phi$) we can simplify the expression for q_{xy}. Specifically it can be decoupled from α and β, since $\cos\beta \approx \cos\alpha \approx 1$. Thus q_{xy} is approximated as

$$\begin{aligned} q_{xy} \approx k\sqrt{\sin^2\phi + (\cos\phi - 1)^2} &= k\sqrt{2 - 2\cos\phi} && (1.41) \\ &= 2k\sin\theta && (1.42) \end{aligned}$$

where $\theta = \phi/2$ and at the Bragg peak is the angle in Bragg's law.

The nanoparticle monolayer is composed of ordered domains of hexagonal close packed particles. These domains are randomly oriented relative to any other within the film. Given the large spot size of the incident beam the Bragg condition for any plane will be satisfied for some fraction of the film's domains. This is analogous to crystalline powder diffraction except in two dimensions, where instead

of having single crystal powder grains there are ordered patches of monolayer of finite extent that are all clustered together to comprise the total film.

Thus all Bragg peaks should be visible and their location along q_{xy} will depend on the interparticle spacing D as well as the particular Miller indicies. The peak location and Bragg plane spacing for each GID peak are listed in Table 1.1. Using this formalism the interparticle spacing of the film can be precisely determined from the location of each of the GID peaks.

Table 1.1: Table of the Miller indicies/Bragg planes that contribute to the GID peaks along with their corresponding q_{xy} positions. D is the interparticle spacing and d is the Bragg plane spacing. This table assumes a hexagonal close packed lattice.

GID Peak	Miller Indicies	Bragg plane	q_{xy}
1st	$(10)(\bar{1}0)(01)$ $(0\bar{1})(11)(\bar{1}\bar{1})$	$d = \frac{\sqrt{3}}{2}D$ $n = 1$	$\frac{4\pi}{D\sqrt{3}}$
2nd	$(1\bar{1})(\bar{1}1)(21)$ $(\bar{2}\bar{1})(12)(\bar{1}\bar{2})$	$d = D/2$ $n = 1$	$\frac{4\pi}{D}$
3rd	same as 1st	$d = \frac{\sqrt{3}}{2}D$ $n = 2$	$\frac{8\pi}{D\sqrt{3}}$
4th	$(13)(31)(\bar{2}1)$ $(1\bar{2})(\bar{1}2)(2\bar{1})\ldots$	$d = \frac{\sqrt{3}}{2\sqrt{7}}D$ $n = 1$	$\frac{4\pi\sqrt{7}}{D\sqrt{3}}$
5th	same as 1st	$d = \frac{\sqrt{3}}{2}D$ n=3	$\frac{12\pi}{D\sqrt{3}}$

1.5.3 Grazing Incidence X-Ray Off-Specular Scattering (GIXOS)

GIXOS is a realtively recent technique [29–32] developed as a useful alternative or compliment to X-Ray Reflectivity for the characterization of interfacial structure along the surface normal. Where as XR requires elaborate and time consuming motion of the beam angle, detector position and sample height, a complete GIXOS measurement can be collected, with an area detector, without any of these adjustments. This fixed geometry allows for much more rapid and real time

collection of evolving systems than XR would be unable to capture. Thus, GIXOS is an ideal technique for in–situ studies of dynamical surface structure such as that which develops in the compression of iron oxide nanoparticle Langmuir-Blodgett films.

Unlike XR, GIXOS measurements are collected out of the specular plane - i.e. $\theta \neq 0$. Although the incident angle α is held fixed, the GIXOS signal is still measured over a range of q_z by subtending a range of the scattering angle β. This was done by using an area detector that had been masked by a set of narrow vertical slits. The detector was then positioned at a fixed θ angle - for the measurements herein $\theta = 0.3°$, which was located between the specular plane ($\theta = 0$) and the first GID peak. A single exposure could then capture the diffuse scatting as a function of β. A diagram of the experimental set-up can be seen in Figure 1.9.

As discussed in section 1.3 scattering from a liquid surface results in a contribution due to the height fluctuation of the surface, known as capillary fluctuations. These capillary fluctuations can be quantified and their contribution to the scattering intensity made explicit in the differential scattering cross section, as shown in equation 1.30. If this is not done then the capillary fluctuation contribution has the effect of blurring the interfacial electron density profile. However, some finite portion of the capillary fluctuation will be included into the intensity measurement due to the finite resolution of the measurement - the result of the finite pixel/slit size of the detector set-up. Therefore, to properly model this capillary contribution, and thus properly model the measured signal one must integrate the differential scattering cross section over the resolution function of the detector to accurate model the scattering signal. The measured intensity at the detector is then given by:

$$\frac{I}{I_0} = \int_{res} \frac{\mathrm{d}\sigma}{\mathrm{d}\Omega}\mathrm{d}\Omega = \frac{A_0}{k^2 \sin\alpha \sin\beta} \left(\frac{q_c}{2q_z}\right)^4 \frac{\eta q_z^2}{8\pi} |\Phi(q_z)|^2 |T_i|^2 |T_s|^2 \int_{res} \frac{1}{q_{xy}^2} \left(\frac{q_{xy}}{q_m}\right)^{\eta} \mathrm{d}\mathbf{q}_{xy} \tag{1.43}$$

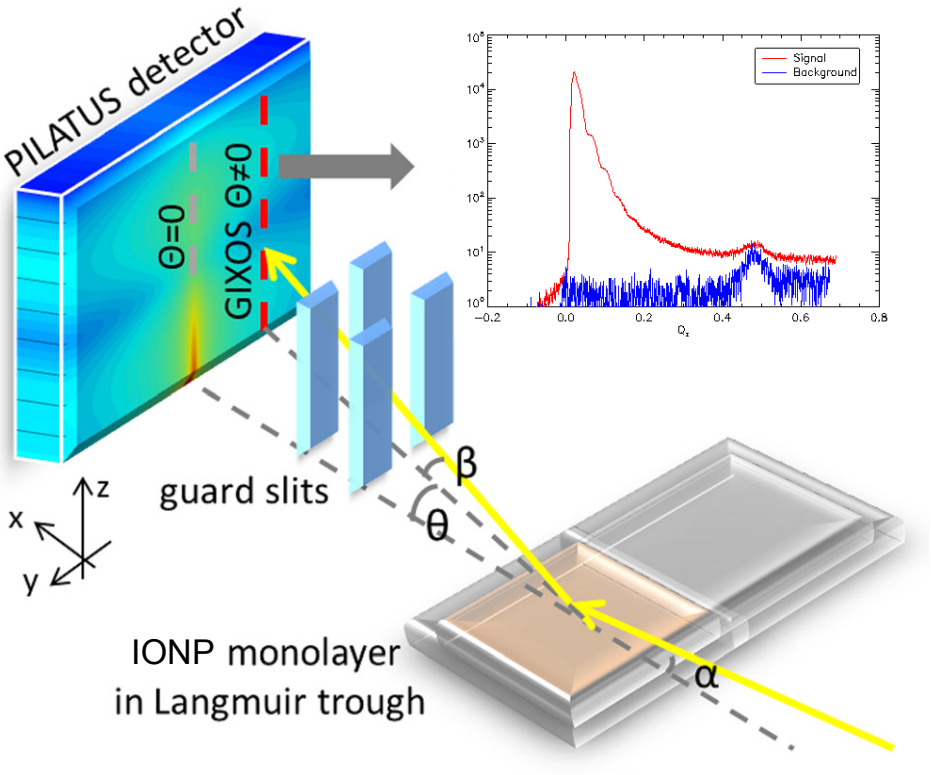

Figure 1.9: Schematic of the GIXOS set-up, where $\theta \neq 0$. Visible are the two sets of vertically oriented slits which define the resolution. The GIXOS signal at $\theta = 0.3°$ with accompanying background scan for the 20 nm film can be seen in the inset.

Chapter 2

SEM and GID Comparison

Nanoscale thin films have shown ever increasing significance in the scientific community in recent years. They have been of great interest due to both their use in studying fundamental behaviors of two-dimensional systems as well as their growing range of technological applications. [5, 33–40] Early such thin films were formed at liquid surfaces and transferred to solid substrates using a Langmuir-Blodgett trough. [41,42] Many techniques have been developed to transfer these liquid surface films to solid substrate, including the Langmuir-Blodgett and Langmuir-Schaefer methods. [43–47] Since the introduction of the Langmuir trough, liquid surface films have been formed from a broad range of different building blocks including phospholipids, polystyrene beads, proteins, and more recently metallic nanoparticles. [31,36,44,48,49] Self-assembly is the primary driving mechanism for the formation of these films. [46, 50, 51]

Previously it has been observed that these nanoscale thin films may not preserve all the aspects of their structure once transferred from liquid surface to solid substrate - these include changes in local molecular order, domain sizes and average inter-particle spacing. [52–55] It is likely these changes depend on several factors, including the method of transference, physical properties of the substrate, physical characteristics of the constituents comprising the film, as well as several others. Therefore it is of interest to be able to verify whether or not the structure of the film is preserved once transferred to the solid substrate. If it can be verified that the characteristics of the film are preserved upon transference then it is more

reasonably assumed that its macroscale properties will be preserved as well.

Many different techniques have been used to directly measure film structure in such systems. Small angle X-Ray scattering (SAXS), X-Ray diffraction, and X-Ray reflectivity have been used for in-situ measurements of in-plane and out-of-plane structure, for liquid surface films. [55–58] Alternatively, for films on solid substrate, similar information has been obtained through the use of AFM, SEM and TEM to image the film. [36, 43, 52, 56, 59] The ability to image these thin films allows for a direct study of their structural properties, which otherwise would have to be indirectly inferred from their surface pressure isotherms or shear modulus. [60]

Based on the above considerations our purpose herein is to demonstrate that the average structure of a nanoscale monolayer of metallic nanoparticles at the air-water interface can be preserved after being transferred to a solid substrate. Moreover, this structural equivalence is demonstrated by comparing the results of image analysis of SEM data (collected post-transference) to in-situ X-Ray diffraction measurements (GID), thereby showcasing the use of SEM as an alternative/companion technique to more widely utilized X-Ray diffraction when studying such monolayer systems. Given that SEM is more practically available and data collection generally quicker than GID, the ability to extract equivalent information from SEM data increases the utility of the technique.

2.1 Experiment

2.1.1 Sample Preparation and Assembly

A Langmuir trough was used to prepare the sample monolayer for both in-situ study as well as transference to solid substrate. The clean trough was filled with an amount of deionized water from a Milli-Q filtration system such that the water surface formed a convex meniscus. The monolayers were formed from oleic acid stabilized iron oxide nanoparticles that were approximately 20 nm in diameter. The nanoparticles were dissolved into a chloroform solution to a mass concentration of 0.5 mg/mL. The Teflon barriers used to compress the film started fully retracted. Using the drop-casting deposition method the nanoparticle solu-

tion was spread onto the water surface. Each drop of solution, randomly deposited every few seconds, was allowed to partially dry before deposition of subsequent drops. The chloroform readily evaporates leaving behind self-assembled domains of nanoparticle monolayer. [18] The solution was deposited until approximately the point at which the drops no longer spread unimpeded due to the density of nanoparticles already present on the liquid surface. The nanoparticles, which we obtained from Ocean Nano Tech (www.oceannanotech.com) had very low polydispersity and the resulting self-assembled film, which extended over centimeters, demonstrated long range uniformity, which has also been observed in previous studies [43, 44]. This uniformity was verified with visible light microscopy. For the 20 nm particle solution, the amount of solution spread corresponded to a surface area coverage of approximately 40%. For comparison this volume of solution was used for all subsequent films. At this point the film was allowed to relax for approximately 30 minutes in order to establish an even distribution of particles. The film was then compressed laterally with the Teflon barriers so that the area available was mostly covered by the nanoparticles, thereby creating a uniform monolayer. [44, 59, 61] At this point the sample, considered fully prepared, was either measured using GID or transferred to a solid substrate.

2.1.2 Langmuir-Schaefer Transfer Method

The Langmuir-Schaeffer method of transferring films provides an alternative to the traditionally used Langmuir-Blodgett method. Unlike the Langmuir-Blodgett technique where the substrate is held perpendicular to the monolayer during transfer, the Langmuir-Schaefer method aligns the substrate parallel to the monolayer, which is transferred when the substrate is pushed through the monolayer and into the subphase. [61] For this work, silicon substrates of approximate area 1 cm^2, were used to transfer the monolayers. Single crystal silicon was chosen due to its low surface roughness and good adherence to oleic acid. [62] The silicon wafers were cleaned by sonication first in ethanol and then di-ionized water, just prior to use. The Langmuir-Schaefer method was then performed using a pair of tweezers: opposite edges of the substrate were grasped by the tweezers, which

was then plunged through the surface of the subphase so that the monolayer was cut at the edge of the substrate. The substrate was then lifted out of the liquid subphase. This process adhered the monolayer to the silicon surface. The film was then stable enough for SEM measurements.

2.2 Grazing Incidence X-Ray Diffraction (GID)

2.2.1 Experiment

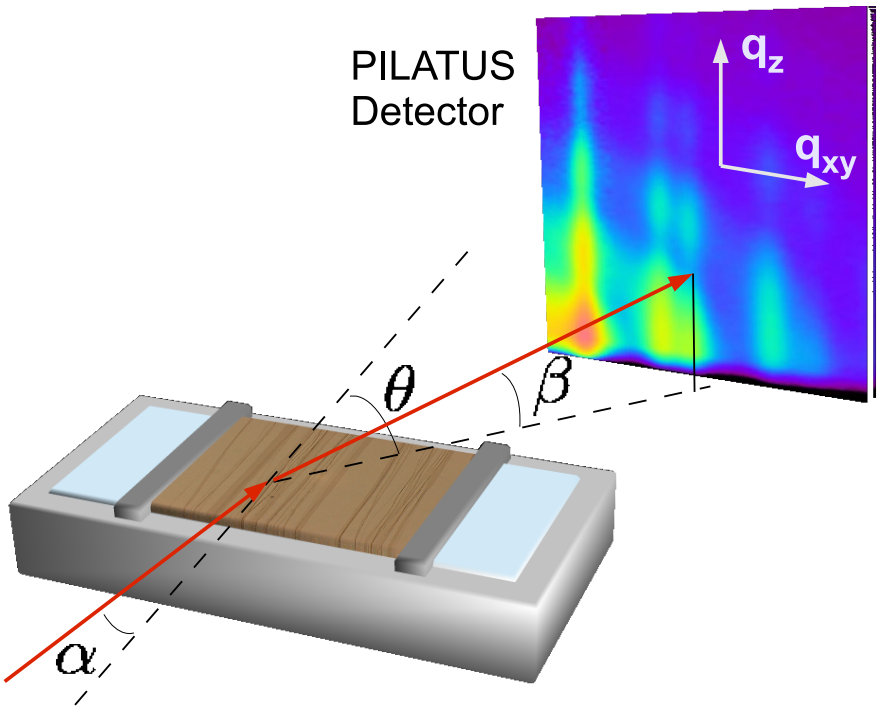

Figure 2.1: GID geometry, characterized by angles α, β, and θ.

The X-Ray scattering experiments were performed at ChemMatCARS 15-ID-C beamline of the Advanced Photon Source (APS) at Argonne National Labs. The monochromatic X-Ray beam was of wavelength $\lambda = 1.239\,\text{Å}$. The scattering geometry used for GID is shown in Figure 2.1 with an incident angle of $\alpha = 0.0906°$, which is below the critical angle for total external reflection from the liquid subphase. This is done to minimize the scattering from the subphase bulk.

The incident beam size was 20 μm horizontal by 120 μm vertical. For the incident angle used, this resulted in a beam footprint of 20 μm $\times$ 7.6 cm along the beam direction. The scattering signal was recorded using a digital, two-dimensional X-Ray detector, Pixel Apparatus for the Swiss Light Source (PILATUS 100K), operating in single-photon counting mode. The detector was located 567.0 mm downstream from the sample.

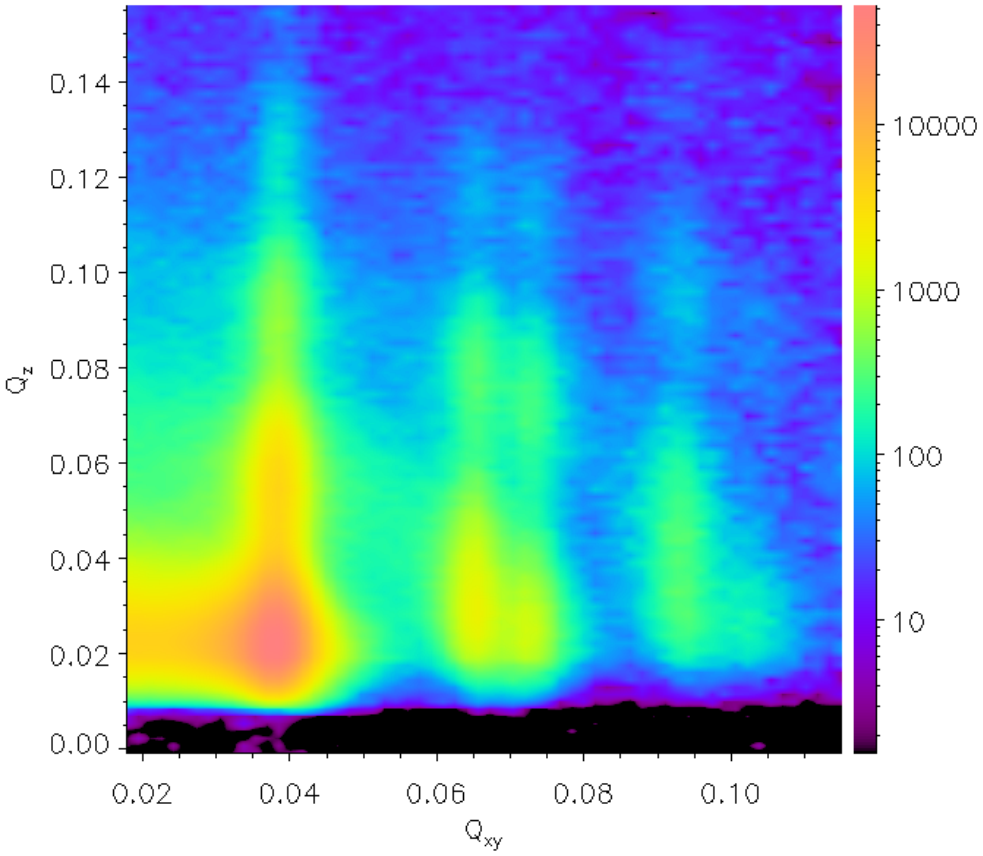

Figure 2.2: 2D GID data showing first through fifth order Bragg rods - the locations of these along the q_{xy} direction correspond to Bragg plane spacings within the film (q_z and q_{xy} in units of Å^{-1}).

Due to the low azimuthal angle of the measured signal ($\theta = 0.30° \rightarrow 1.60°$), two sets of angle-limiting slits were used to mask the detector, thus reducing the higher intensity low-angle scattering. One set of slits was located at a distance 292.0 mm from the sample and the second set was located directly in front of the

PILATUS detector. The detector and slits were then stepped through the intended range of θ and a composite, two-dimensional image of the scattering signal was formed. The resulting two-dimensional data can be seen in Figure 2.2; the first through fifth order GID Bragg rods were visible for these films. Note, along the horizontal (θ) direction, data was collected up to $q_{xy} = 0.15\,\text{Å}^{-1}$. The masking slits defined the reciprocal space resolution of the GID data to $\Delta q_{xy} = 3.9 \times 10^{-3}\,\text{Å}^{-1}$.

2.2.2 Analysis

By defining the elastic scattering vector ($\mathbf{q} = \mathbf{k_f} - \mathbf{k_i}$) as the difference between the scattered and incident wave vectors, the scattering intensity recorded on the detector was represented in terms of the components of $\mathbf{q}$ instead of the angles α, β, and θ. Due to the planar geometry of the sample the scattering vector was best decomposed into components parallel and perpendicular to the sample surface. Thus:

$$q_{xy} = k\sqrt{4\sin^2\left(\frac{\beta+\alpha}{2}\right)\sin^2\left(\frac{\beta-\alpha}{2}\right) + 4\cos\alpha\cos\beta\,\sin^2(\theta)} \quad (2.1)$$

$$q_z = 2k\sin\left(\frac{\beta+\alpha}{2}\right)\cos\left(\frac{\beta-\alpha}{2}\right) \quad (2.2)$$

where $q_{xy} = \sqrt{q_x^2 + q_y^2}$ is the in-plane component and q_z is the component perpendicular to the plane of the sample. [63] The q_z component has no dependence on θ, additionally the q_{xy} component varies less than 1% over the range of β recorded by the detector (in Figure 2.2). Thus the two-dimensional data could effectively be described by q_{xy} along the horizontal direction and q_z along the vertical. The data was reduced by integrating the intensity over the q_z direction on the detector, thus $I(q_z, q_{xy}) \rightarrow I(q_{xy})$. Due to the finite widths of the beam spot as well as the detector slits, the amount of illuminated sample seen by the detector varied with θ. To account for this, the raw data was multiplied by $\sin(\theta)/\sin(\theta_{\text{min}})$, where θ_{min} was the lowest measured angle of θ measured by the PILATUS detector. The result of this data reduction can be seen as the GID curve in Figure 2.5.

2.3 Scanning Electron Microscopy (SEM)

2.3.1 Experiment

The SEM measurements were performed at the Calit2 Nano3 facility at UC San Diego. Once transferred to a silicon substrate the monolayers were imaged using a FEI XL30 ultra-high resolution SEM. A typical example of one of the images can been seen in Figure 2.3. The three adjustable experimental parameters in the data collection were 1.) magnification, 2.) image contrast and 3.) image brightness. In order to get optimal signal from SEM the field of view should be maximized, thereby imaging the maximum number of nanoparticles so as to get the best representation of the monolayer, while simultaneously having sufficiently high magnification such that the individual particle features are not lost due to pixelation. Additionally, contrast and brightness should be adjusted in order to utilize the whole dynamic range while simultaneously maximizing the contrast between the particles and the substrate background - this way the image captures the detail of the form factor and also distinguishes the particles from one another.

For a given magnification the real space pixel size determined the largest reciprocal space value we could measure. In the GID data the signal from the in-plane structure was visible as high as approximately $q_{xy} = 0.11\,\text{Å}^{-1}$. This corresponded to the fifth order GID Bragg rod, as can be seen in Figure 2.2. Therefore the SEM images were taken such that the analyzed results could be compared at least up to this value of q_{xy}. This then defined the minimum magnification of the SEM image. As an overestimate, the largest value for q_{xy} was chosen to be approximately twice that of the fifth order Bragg rod, thus a value of $q_{max} = 0.18\,\text{Å}^{-1}$, which corresponds to a pixel size of approximately $35\,\text{Å}$. This determined the necessary magnification of approximately $M = 7.6 \times 10^4$.

2.3.2 Analysis

We started by expressing the two-dimensional grey-scale SEM image as a matrix $I(x_i, y_i)$, where the dimension of the image was $N_x \times N_y = 645 \times 484$. A two-dimensional Fast Fourier Transform was then applied to the matrix and the

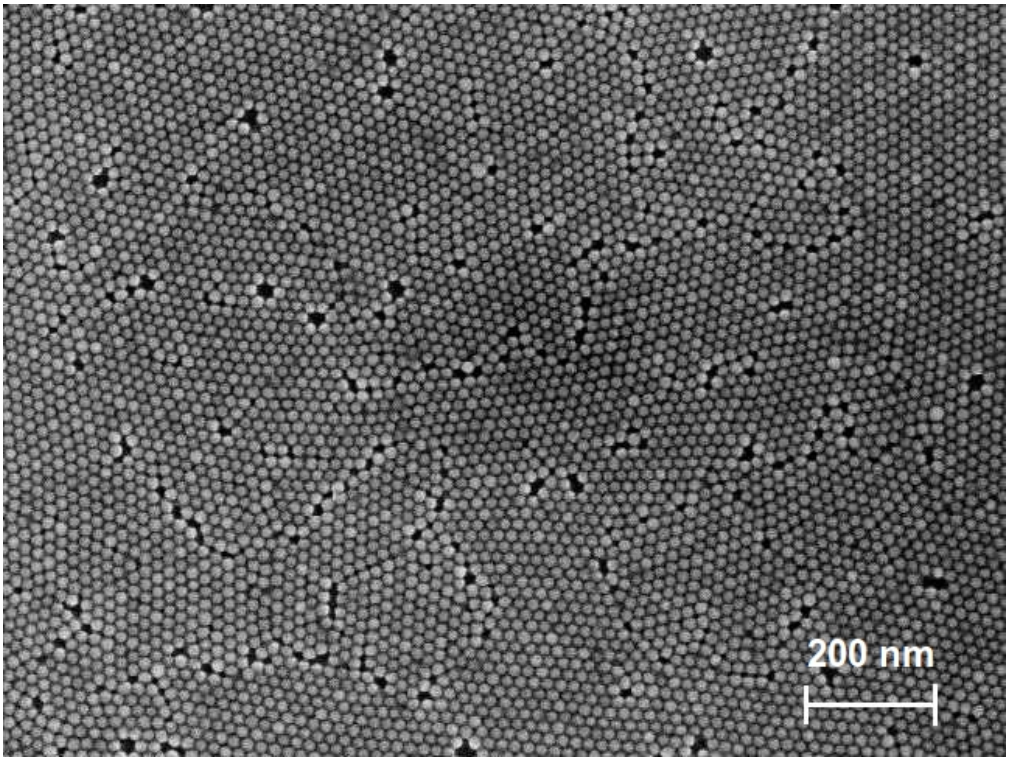

Figure 2.3: An SEM image of IO monolayer stamped onto silicon substrate.

resulting data was multiplied by its complex conjugate to obtain the reciprocal space intensity $I(qx_i, qy_i)$, Eq. 2.3.

$$I(q_{x_i}, q_{y_i}) = |\mathcal{F}_x\{\mathcal{F}_y\{I(x_i, y_i)\}\}|^2 \tag{2.3}$$

The resulting reciprocal space intensity is shown in Figure 2.4. Note the weakly visible six-fold symmetry which implies partial long range order within the field of view of the image. The reciprocal space matrix $I(q_{x_i}, q_{y_i})$ was then re-expressed in polar coordinates $(|\mathbf{q}|, \theta)$ where $|\mathbf{q}| = \sqrt{q_x^2 + q_y^2}$ and $|\mathbf{q}| = 0$ is located at the central pixel of Figure 2.4. The image was binned into annular regions about $|\mathbf{q}| = 0$. The binned regions were then integrated and normalized by the number of pixels contained within each one. The result is a line plot of the average radial intensity as seen in Figure 2.5 (solid line).

The contrast and brightness of the SEM image are physically related to the electron density of the sample, with the brightness corresponding to the mean

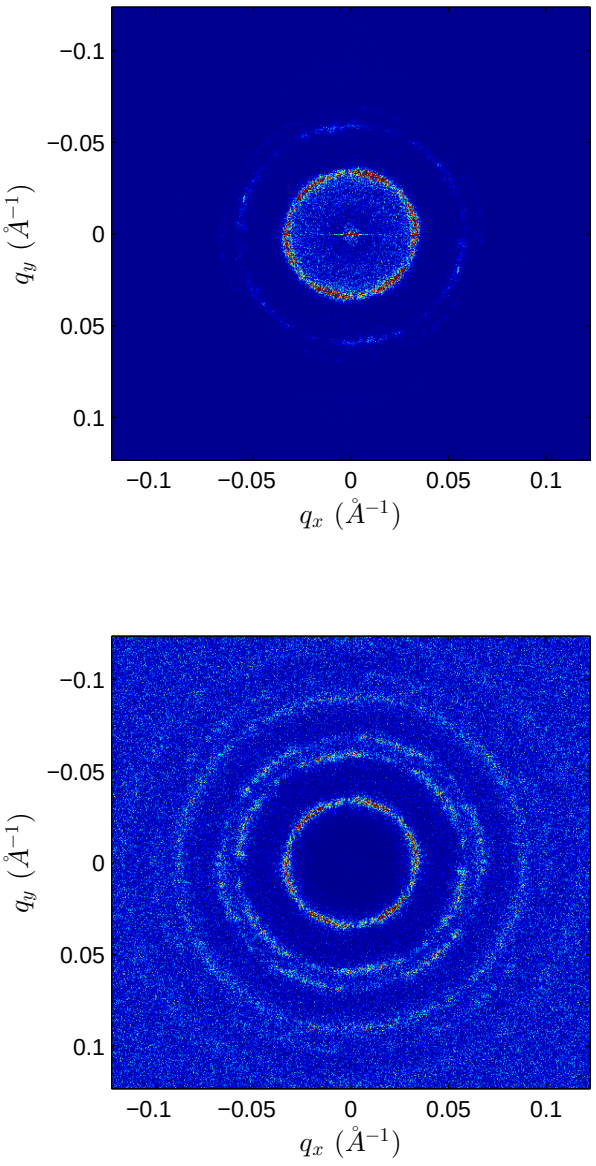

Figure 2.4: Top: $I(q_x, q_y)$ of SEM image in Figure 2.3, calculated from equation 2.3. Bottom: $I(q_x, q_y)$ for isolated structure factor, calculated from Figure 2.6, from same SEM image.

density and the contrast corresponding to the relative density between different portions of the sample. Because the contrast and brightness were freely adjusted

during data collection in order to improve the images by eye, one cannot draw any physical conclusions from the overall intensity of $I(q)$. In order to compare analysis of multiple SEM images or an SEM image with corresponding GID results, contrast and brightness differences were accounted for by two parameters: a scaling factor and a constant off-set. The scaling was done to fit the lowest-q peak from SEM and GID to one another. The result of this comparison can been seen in Figure 2.5.

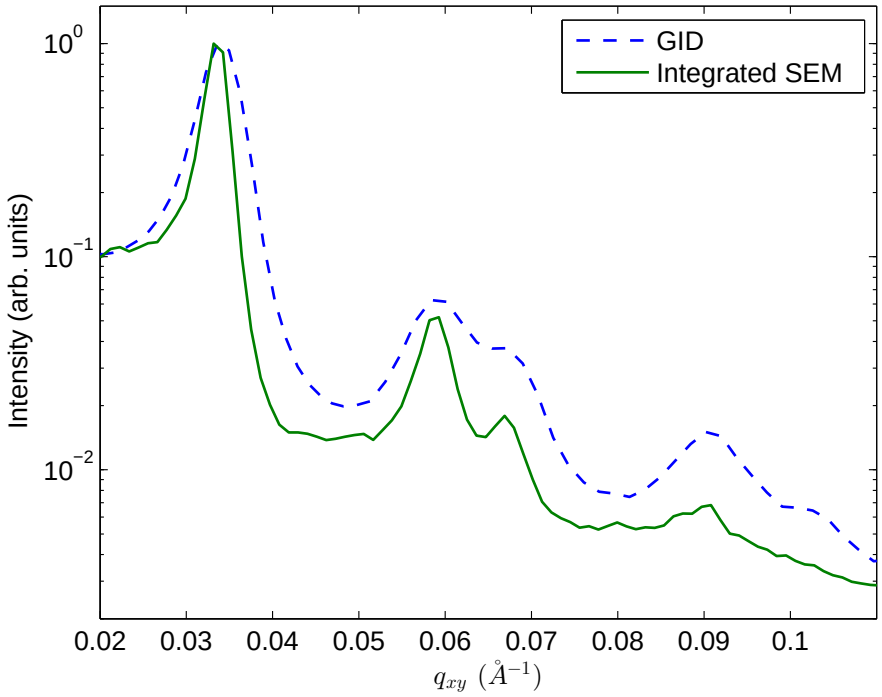

Figure 2.5: Comparison of the angular integration of $I(q_x, q_y)$ seen in Figure 2.4 (Top) to the GID measurement along the q_{xy} direction in Figure 2.2.

The first three Bragg peak locations show good agreement between the SEM and GID data which suggests not only that the lattice structure of the film is preserved once transferred to the silicon substrate, but also that the SEM is capable of capturing the details of the film structure when analyzed in this manner. However, the relative peak amplitudes and peak widths are not in close agreement and the higher order peaks (4th and above) are not readily visible. There are several reasons for this, one of which is the difference in particle form factor experienced by

SEM and X-Ray scattering (see Mott-Bethe formula). In order to account for this difference in form factor the reciprocal space intensity was approximately assumed to be given by eq. 2.4,

$$I(\mathbf{q}) \sim N|f(\mathbf{q})|^2 S(\mathbf{q}) \tag{2.4}$$

where $f(\mathbf{q})$ is the particle form factor of an individual nanoparticle, $S(\mathbf{q})$ is the structure factor of the monolayer, and N is the total number of particles being illuminated. This approximation is valid for highly monodispersed particles, which is accurate for the 20 nm nanoparticles used since they have less than 5% polydispersity. Since the SEM electron probe has a characteristically different energy and penetration depth than does the GID X-Ray probe, the two measurements should exhibit different form factors. Despite their different form factors, the structure factor should be equivalent in both cases if the monolayer structure is preserved upon its transfer. In order to better compare the GID and SEM results we then attempted to isolate the structure factor so that they could be compared without the contribution of the form factor.

Using the Microscopy Image Segmentation Tool (MIST) [64] the centers for all nanoparticles within the SEM image were located. By replacing each particle by a single non-zero pixel at its center the form factor was effectively eliminated from the SEM image, seen in Figure 2.6. By applying the same analysis as described above the reciprocal space intensity, due solely to the structure factor, was retrieved ($S(q_{xy})$). Lastly, an exponential function was fit to the background of $S(q_{xy})$ and divided out. The normalized results can be seen in Figure 2.7. By removing the contribution of the form factor the fourth and fifth order Bragg peaks can now be resolved.

In order to compare this result to the X-Ray data we then attempted to isolate the structure factor from the total GID scattering data (Figure 2.2). Due to the quasi two-dimensional nature of the monolayer, the out-of-plane structure (along the z-direction) contains only information about the particle form. Therefore the intensity fluctuation along the q_z–direction, as detected by the PILATUS detector, should be an approximation of the particle form factor $|f(\mathbf{q})|^2$. Thus

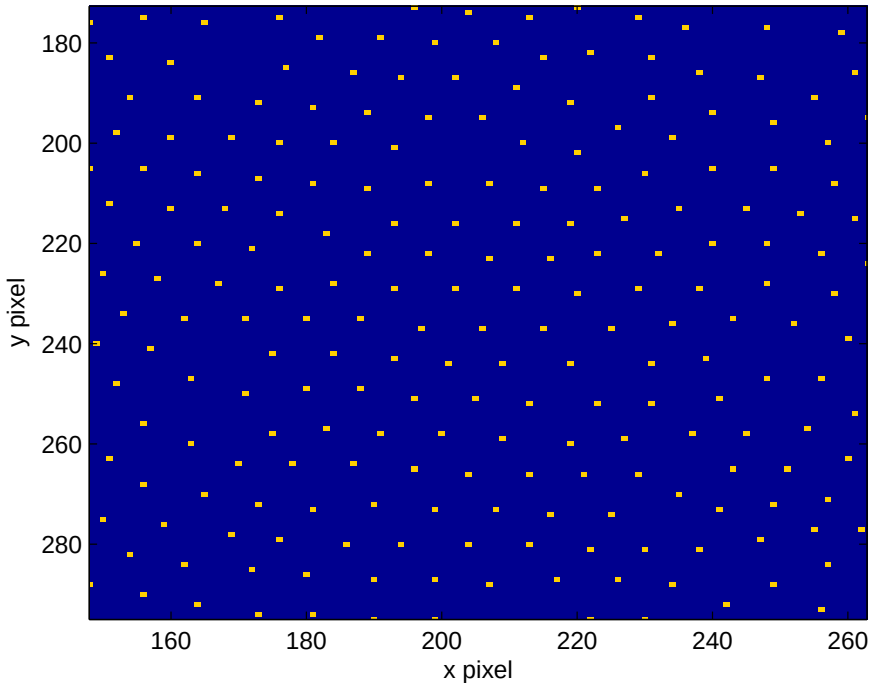

Figure 2.6: Detail region of SEM image showing the particles replaced by single pixels at center. This represents the structure of the film.

dividing the total intensity along the q_{xy} direction (which contains both form and structure factor contributions) by the extracted form factor isolates the structure factor $S(q_{xy})$ (eq 2.4). These results can be seen in Figure 2.7, where they are compared to the isolated structure factor from the SEM data.

2.4 Discussion and Conclusion

Qualitatively, the first through fifth order GID peaks are in better agreement with the SEM results in Figure 2.7 than they are in Figure 2.5, in both the peak amplitudes and widths.

Moreover, in Figure 2.7 the SEM results show higher peak contrast than the GID results, There are two possible reasons for this: the difference in the q-space resolution of the two measurements and/or the difference in the size of the region probed by each technique. The resolution resulting from the SEM data

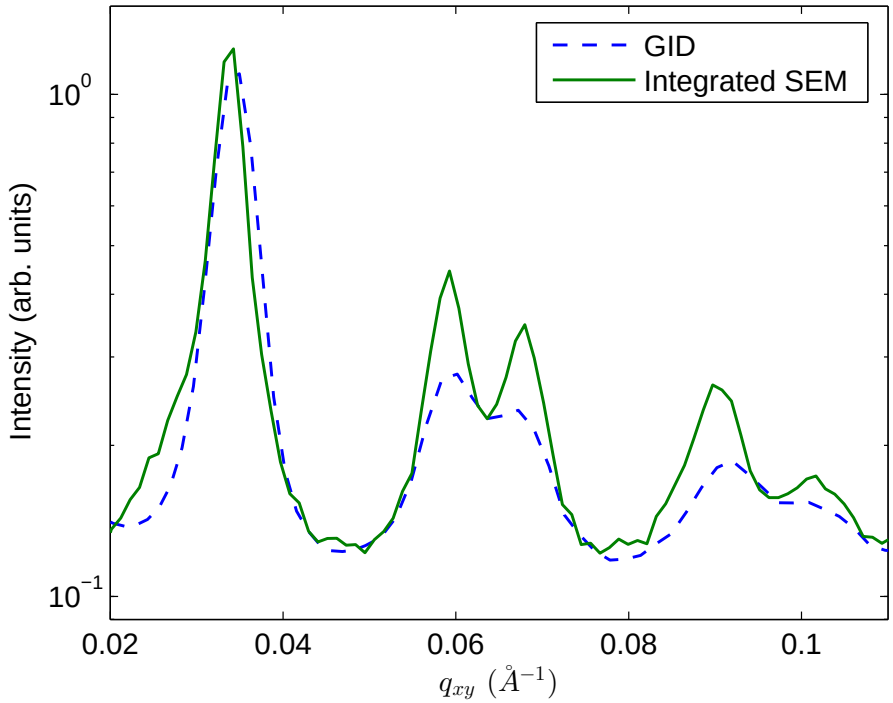

Figure 2.7: Comparison of the structure factors $S(q_{xy})$ isolated from both the GID and SEM data.

processing (specifically the binning and integration) was approximately $\Delta q_{xy} = 3.0 \times 10^{-3}\,\text{Å}^{-1}$. Given that the q-space resolution for the GID measurement is $\Delta q_{xy} = 3.9 \times 10^{-3}\,\text{Å}^{-1}$ the difference in the line shapes seen in Figure 2.7 could be accounted for by the difference in resolution.

On the other hand, the size of the regions probed by the two techniques could have a big impact on the subsequent analysis. The SEM measurement sampled a film region of $2.05\,\mu\text{m}^2$, as seen in Figure 2.3. Conversely, based on the beam size and incident angle, the GID measurement sampled a film region of approximately $1.52 \times 10^6\,\mu\text{m}^2$. In other words, GID sampled approximately one million times more film area than did the SEM, but it is unable to isolate the structure of smaller, local regions of the film.

The higher contrast of the SEM results implies the data is of a region of greater film uniformity than the area sampled in the GID measurements. Given the larger GID sampling region, it likely captured many more defected regions of

the film, thereby decreasing its resulting contrast. But, the fact that the local and global structure, probed by SEM and GID respectively, is as comparable as shown in Figure 2.7, suggests the local lattice spacing is well representative of the large scale average.

In order to account for the difference in contrast multiple SEM images could be collected and processed (as described herein) and then subsequently averaged together. This result would be more representative of the global behaviour of the film which would manifest in the peak contrast. In this way SEM can act as a scalable substitute for GID, capable sensitivity to the local structure as well as wide-range film statistics. This greatly improves the versatility of the SEM technique.

Thus this comparison demonstrated that a transferred iron oxide nanoparticle film maintains its structural spacing and hexagonal order from its original assembly on the liquid surface. Moreover this novel use of SEM for comparison to GID proves useful in the study of nanoparticle monolayer structure and may find broader applications in other thin film systems.

2.5 Supplemental

The content of this chapter up to this point has been a reproduction of my paper submitted for publication to *Review of Scientific Instruments*. The remainder of this chapter is being appended to expand upon the preceding analysis in order to address some details that the brevity of the the journal of submission would not permit.

2.5.1 Langmuir-Schaefer Transfer

The Langmuir-Schaefer transfer technique much like the Langmuir-Blodgett technique relies on the film's constituent being able to adhere to the substrate on which it will be supported. Typically this bonding process is the result of non-covalent interactions such as electrostatic, $\pi - \pi$ or van der Waals effects between the substrate material and particles of interest. Because of this the choice of

substrate is an important factor. [42]

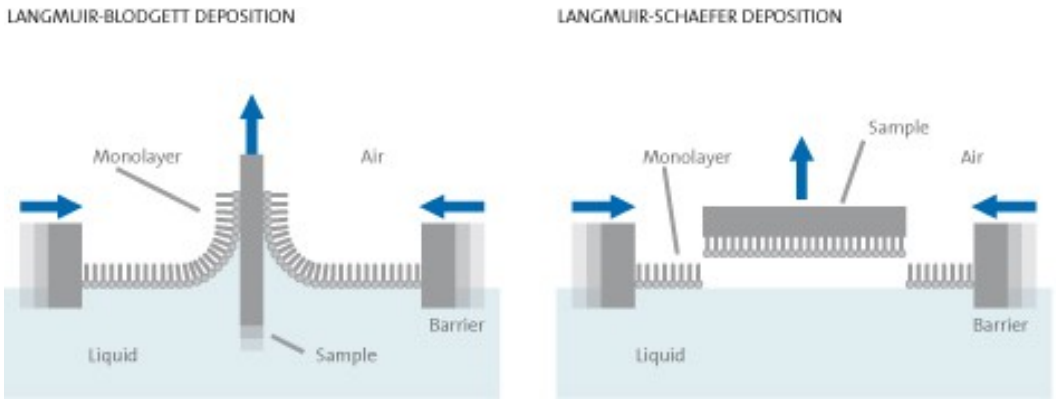

Figure 2.8: A schematic comparison between Langmuir-Blodgett (left) and Langmuir-Schaefer (right) transfer. This figure was reproduced from online.

There are a few distinctions between Langmuir-Schaefer and Langmuir-Blodgett that should be pointed out. The primarily difference is in the geometry: Langmuir-Blodgett is performed with the substrate oriented perpendicular to the liquid surface and thus initially the film is also perpendicular to it, as seen in Figure 2.8. The result is that the film may experience greater in–plane stress when using the Langmuir-Blodgett technique, given that the force between substrate and film is parallel to the film. This can be reduced by slowing the speed at which the substrate is drawn from the interface. [65] Conversely, with the Langmuir-Schaefer technique the substrate exerts a force on the film perpendicular to the surface and it attempts to do so uniformly over the film. Therefore the in–plane structure is more likely to be preserved. However the force applied in this process may disrupt any out–of–plane structures, thus it may not be as effective for multi–layered or folded films.

Secondly, the two methods result in the substrate adhering to different sides of the film. [42] Conventionally, the Langmuir-Blodgett technique starts with the substrate penetrating the interface. The film is then deposited with the substrate in place and finally the substrate is pulled out. This results in the substrate being adhered to the underside of the film. Conversely, the Langmuir-Schaefer technique results in the substrate adhering to the top surface of the film. In the even of an asymmetric film, such as those formed from amphiphilic constituents. But the

symmetry of the iron oxide nanoparticles whose oleic acid capping results in a hydrophobic film from top or bottom.

The Langmuir-Schaefer technique does not necessitate that the substrate pass through the liquid interface in order to transfer the film. Depending on the tensile strength of the film, slight contact with the substrate may be sufficient to cut it at the substrate's boundaries. Given the high Shear and Young's moduli of the iron oxide films it was necessary to plunge the substrate through the liquid interface in order to exert a large enough force to cut the film. [60] The comparatively weak interaction between nanoparticles and Si wafer was not sufficient.

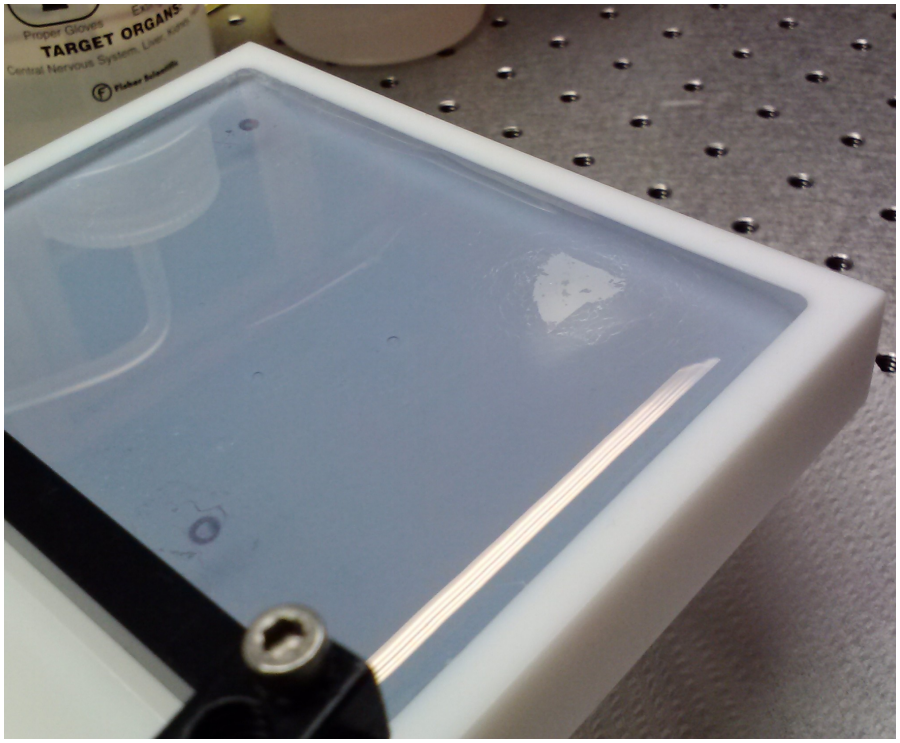

Figure 2.9: An example of the film, post stamping. This film is formed from 6 nm spherical gold nanoparticles (used for visible demonstration). The iron oxide films demonstrate comparable behavior, but the film itself is difficult to discern in photos.

Once stamped the films appear to maintain their macroscopic order in the region close to where the substrate was applied. Essentially, the transfer method does not appear to perturb the film on a macroscopic scale, and the missing patch of film maintains its perimeter. This behavior is only seen for well compressed

films. Figure 2.9 is an example of the state of the compressed film after stamping has occurred. The film in this image is in fact a gold nanoparticle film, which was chosen since it's easily visible - done so for illustrative purposes. Iron oxide nanoparticle films demonstrate very similar behavior.

Examples of the substrates with adhered films can be seen in Figure 2.10. On the left is a substrate containing a highly compressed film. The lighter colored circle in the center was the result of a bubble that was trapped against the surface during stamping. On the right are two substrates containing low-density (uncompressed) films. These can not be discerned with the naked eye, unlike a highly compressed film.

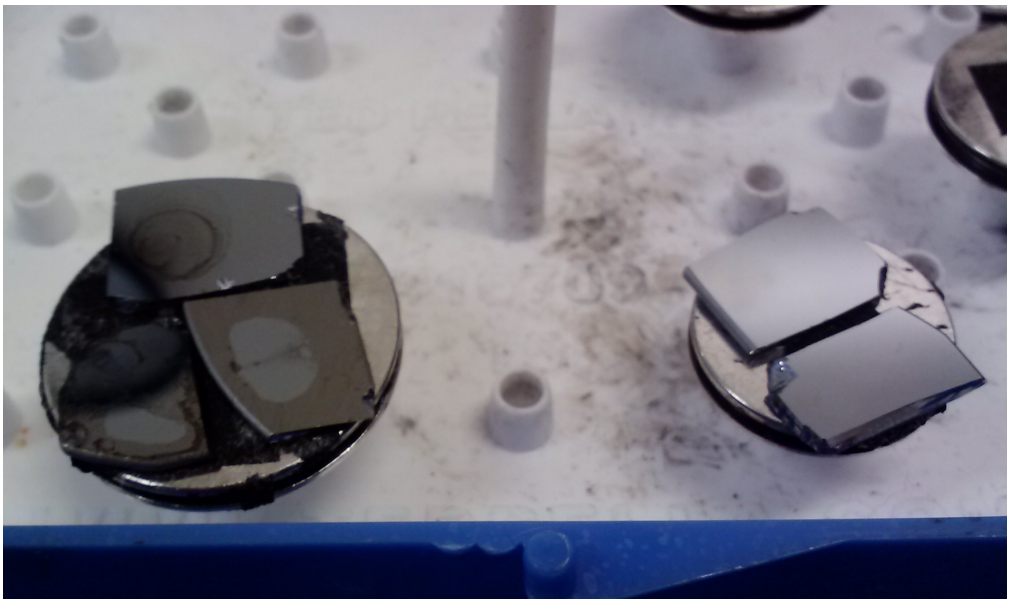

Figure 2.10: Here are multiple substrates post transference. On the left (front) is a highly compressed 20 nm iron oxide film. The two substrates on the right are uncompressed 20 nm iron oxide films.

2.5.2 GID Form Factor

In Section 2.3 the GID data seen in Figure 2.2 was analyzed by separating the contribution to the scatter due to the particle shape (the Form Factor) from that due to the lattice arrangement of the particles (the Structure Factor). The relationship was stated in equation 2.4. This is obtained if one assumes that the

scattering is from N number of identical particles located at positions $\{R_i\}$. Then the electron density in the scattering volume is given by [19–21]

$$\rho(\mathbf{r}) = \sum_{j=1}^{N} f(\mathbf{r} - \mathbf{R_i}) = f(\mathbf{r}) * \sum_{j=1}^{N} \delta(\mathbf{r} - \mathbf{R_i}) \tag{2.5}$$

We can then calculate the reciprocal space density from this definition, and make use of the fact that the Fourier Transform of a convolution is the product of the Fourier Transforms (convolution theorem).

$$\begin{aligned} \rho(\mathbf{q}) &= \int_{Vol} \rho(\mathbf{r}) e^{-i\mathbf{q}\cdot\mathbf{r}} \mathrm{d}\mathbf{r} & (2.6) \\ &= \left(\int f(\mathbf{r}) e^{-i\mathbf{q}\cdot\mathbf{r}} \mathrm{d}\mathbf{r} \right) \left(\int \sum_{j=1}^{N} \delta(\mathbf{r} - \mathbf{R_i}) e^{-i\mathbf{q}\cdot\mathbf{r}} \mathrm{d}\mathbf{r} \right) & (2.7) \end{aligned}$$

Assuming kinematic scattering, I identify the absolute square of the reciprocal space density as the measured intensity.

$$\begin{aligned} I(\mathbf{q}) \sim |\rho(\mathbf{q})|^2 &= |f(\mathbf{q})|^2 \sum_{jk} e^{-i\mathbf{q}(\mathbf{R_j} - \mathbf{R_k})} & (2.8) \\ &= N|f(\mathbf{q})|^2 S(\mathbf{q}) & (2.9) \end{aligned}$$

which is the original relationship between intensity, form factor, and structure factor (equation 2.4). [19]

The structure factor in the 2D only had dependence on q_{xy} ($S(\mathbf{q}) \rightarrow S(q_{xy})$). Therefore in order to capture all the detail in $S(\mathbf{q})$ it was only necessary to take a horizontal slice of the 2D GID data. By taking this slice at a q_z value where the signal intensity is maximum will result in the greatest contrast. This slice ($I_z(q_{xy})$) can be seen in Figure 2.11, as a red box - note that it intersects the maxima of the five Bragg rods. This region also contains information about the form factor. Unlike the structure factor the form factor is a function of $|\mathbf{q}|$. By extracting the intensity variation along the q_z direction over a very narrow range of q_{xy} one can directly measure the form factor absent any contribution from $S(\mathbf{q})$. This isolated region can be seen in Figure 2.11, the blue box $|f_{xy}(q_z)|^2$.

From I_z and $|f_{xy}|^2$ one can calculate $S(q_{xy})$ using equation 2.4, but they

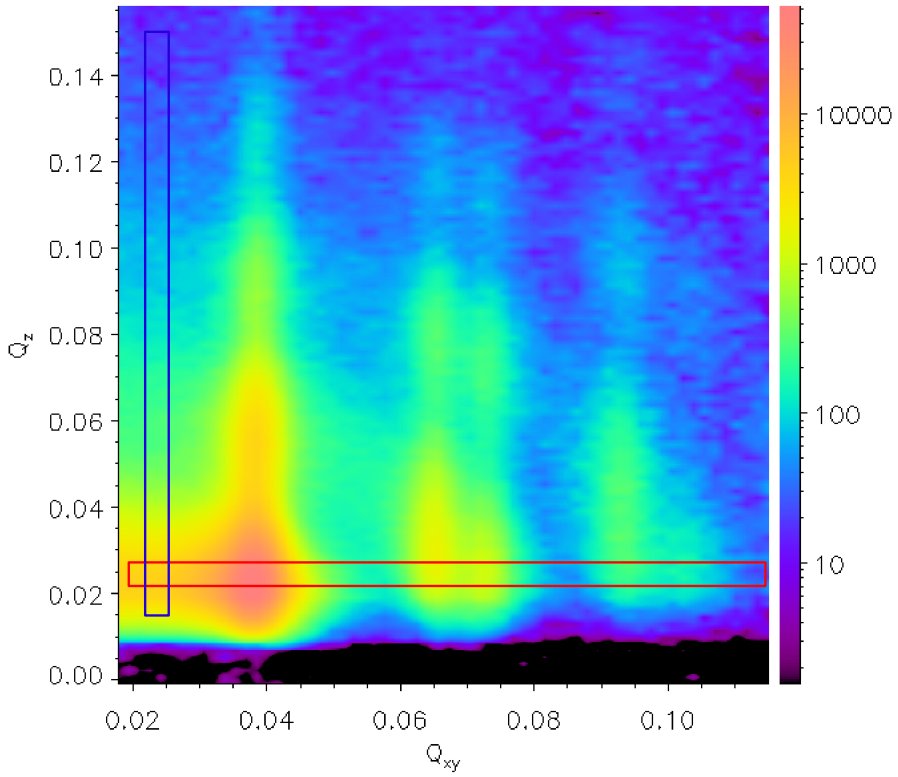

Figure 2.11: A picture of the full 2D GID data. Blue box $|f_{xy}(q_z)|^2$ - Intensity at fixed q_{xy} used to represent the form factor. Red Box ($I_z(q_{xy})$) - Intensity data at fixed q_z containing both structure and form factor.

must undergo a change of variables before being compared:

$$I_z(q_{xy}) \rightarrow I_z(|\mathbf{q}|) \tag{2.10}$$

$$|f_{xy}(q_z)|^2 \rightarrow |f_{xy}(|\mathbf{q}|)|^2 \tag{2.11}$$

$$\Rightarrow S(\mathbf{q}) \propto \frac{I_z(|\mathbf{q}|)}{|f_{xy}(|\mathbf{q}|)|^2} \tag{2.12}$$

Finally, a change of variables in $S(\mathbf{q})$ results in the extracted structure factor $S(q_{xy})$ seen in Figure 2.7. The 1D plot of theform factor data used in this calculation (blue box in Figure 2.11) can be seen in Figure 2.12.

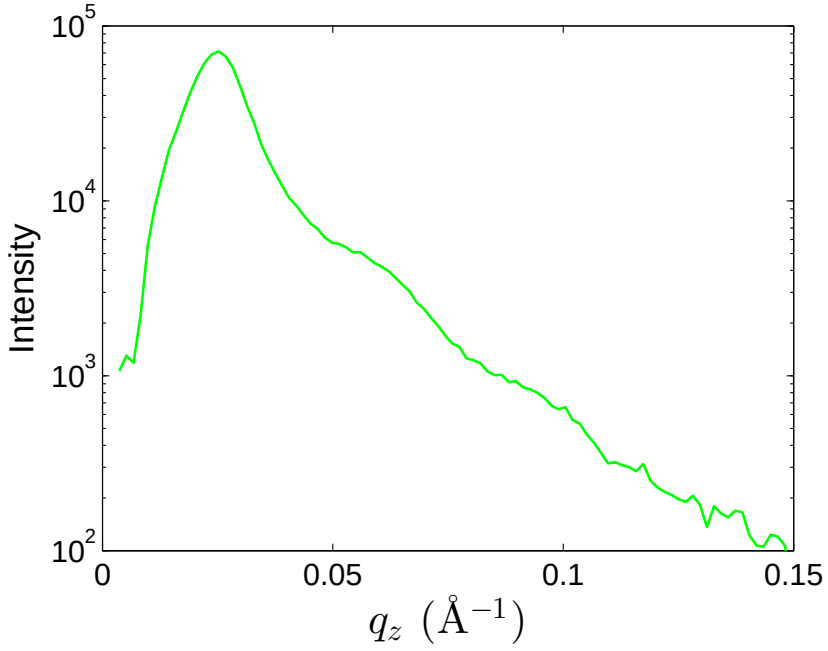

Figure 2.12: 1D plot of the form factor extracted from the 2D GID data. Specifically this is a plot of he data located in the blue box of Figure 2.11.

2.5.3 SEM Form Factor

In section 2.3 the SEM images were analyzed by locating the center of each particle $\{\mathbf{R_i}\}$ within the image and replacing it by a single pixel of value unity. The remainder of the image is zeroed. Given that the grey scale of the SEM image can be interpreted as electron density then equation 2.5 can be applied and the above image processing results in

$$\rho(\mathbf{r}) \rightarrow \sum_{j=1}^{N} \delta(\mathbf{r} - \mathbf{R_i}) \tag{2.13}$$

and therefore the form factor is eliminated from the final result. Conversely the form factor of an averaged particle can also be determined, as follows. Having located all the particle centers, the region around each center (which represents the particle shape) can be numerically overlaid and averaged together, pixel by pixel. The resulting average particle, for the SEM image in Figure 2.3 can be seen in Figure 2.13. Note that asymmetries are still apparent despite averaging over several thousand particles.

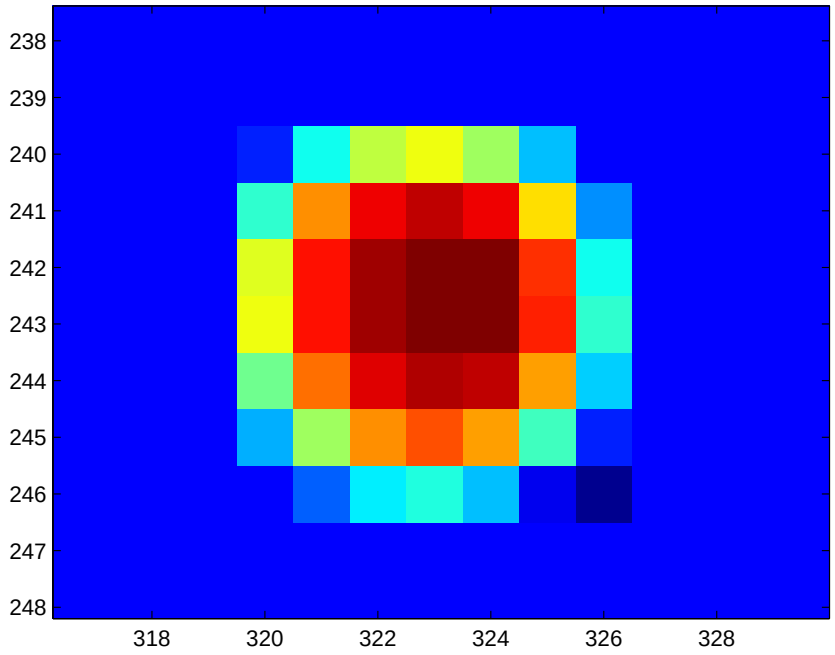

Figure 2.13: Average particle obtained from all the particles located in Figure 2.3

We can then Fourier Transform this averaged particle to obtain the 2D form factor, which can be seen in Figure 2.14. Lastly, the 2D results can be angularly integrated, akin to the process carried out in section 2.3, to obtain the form factor as a function of $|\mathbf{q}|$. THe result of which are plotted in Figure 2.15 (blue curve). If one assumes the particle is well aproximated by a sphere of radius R then the form factor should be given by [21]

$$|f(\mathbf{q})|^2 = \left[\frac{\int_{V_R} dV \exp[-\imath\, \mathbf{q}\cdot\mathbf{r}]}{V_R}\right]^2 \rightarrow \left[3\frac{\sin(qR) - (qR)\cos(qR)}{(qR)^3}\right]^2 \qquad (2.14)$$

The average-particle form factor is different than the *averaged* particle form factor $\frac{1}{N}\sum |f_i(\mathbf{q})|^2$ but the formalism of equation 2.5 assumes a uniform particle density $f(\mathbf{r})$ for all N particles and thus it represents the former. This of course is a simplification and in practice the Fourier transform of the image is related to the *averaged* particle form factor since the particle density function $f(\mathbf{r}-\mathbf{R_j})$ in equation 2.5 is in fact different for each particle (i.e. $\{f_i(\mathbf{r}-\mathbf{R_i})\}$).

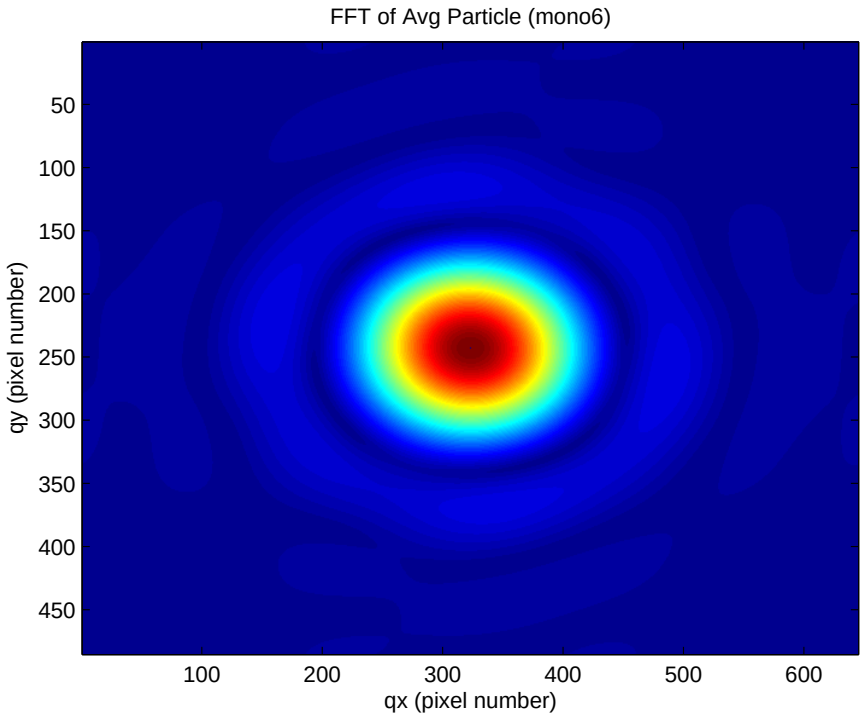

Figure 2.14: The 2D FFT of the average particle in Figure 2.13, which was padded with zeros so that the particle represented the equivalent image fraction as the original SEM image.

A by–product of this is that the form factor extracted from either the GID or SEM data is not well fit by equation 2.14. The poly–dispersity of the particles in the scattering volume have the effect of broadening the total form factor. Therefore by fitting equation 2.14 convolved with a guassian to the GID data along the q_z direction at the first GID peak results in the curve seen in Figure 2.15 (green curve). Finally, one sees a comparison between the SEM and GID form factors.

2.5.4 Disordered/Composite SEM Image Analysis

One major difference between the SEM and GID techniques is the disparity in scattering volume, as discussed in section 2.4. The GID measurements have a footprint approximately 10^6 times larger than that of the SEM images. Therefore the GID measurements will be more representative of the global state of the film. This large footprint will capture the range of disorder that's present: dislocations,

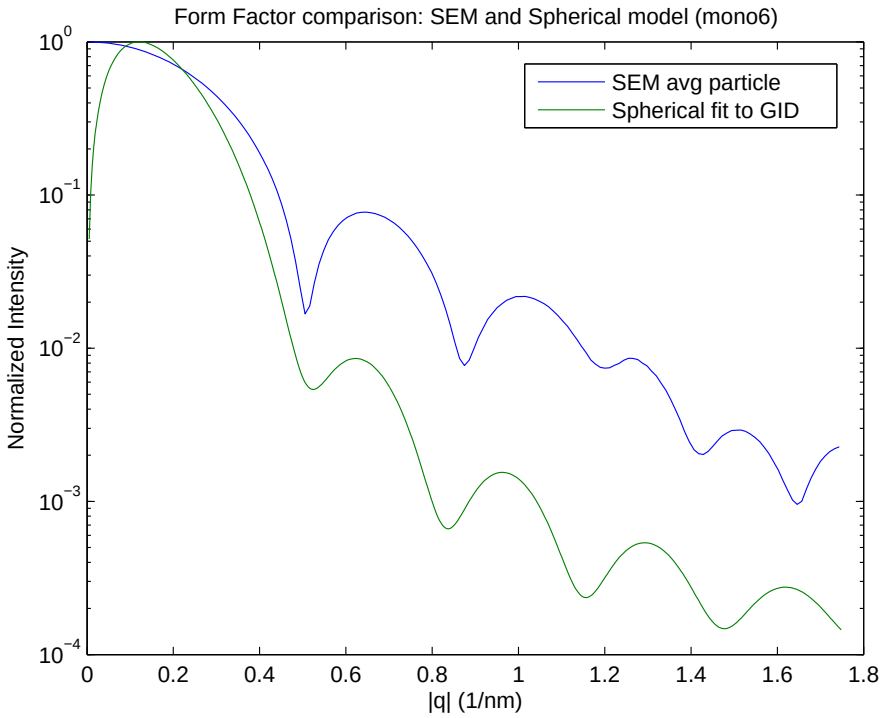

Figure 2.15: Angular integration of FFT (Figure 2.14) of the average particle as compared to a particle form fit to the GID using a spherical model.

grain boundaries, large and small voids, glassy regions, etc. These are not likely to be present in the SEM images due its much smaller scattering volume. The question becomes how are the results of the analysis in section 2.3 affected when the SEM images capture varying degrees of disorder?

In Figure 2.16 one can see two SEM images containing varying degrees of disorder. The image on the left is that from Figure 2.3. The image on the right is another image taken from the same film but in a different location and one can clearly see multiple large scale defects - specifically, voids, blank patches and disordered clumps. Though, for the most part, this image shows comparable film uniformity over its majority. The comparison between the Fourier transform and angular integration analysis for these two images can be seen in Figure 2.17.

It is clear from Figure 2.17 that the basic line shape for each of the GID peaks is preserved. The relative amplitudes, peak locations and widths are preserved. The effects of the additional defects is two fold: 1.) the peak contrast is

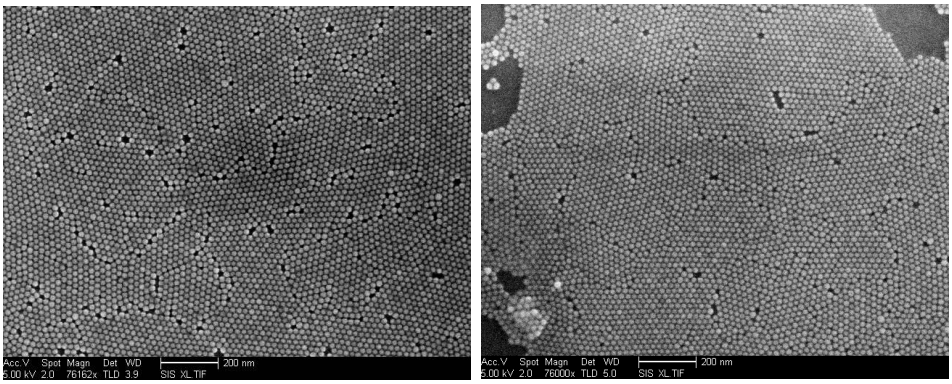

Figure 2.16: Two SEM images of transferred 20 nm nanoparticle films showing differing degrees of disorder.

decreased for the more disordered film and 2.) the low-q line shape shows strong disagreement. The low-q region corresponds to larger length scales in the SEM image. The largest disparity in this low-q region is at approximately $q_{xy} = 0.007^{-1}$, which corresponds to a length scale of $2\pi/q_{xy} = 898$ which is approximately 4-5 particles across. The defects visible in the right hand image are approximately this size scale or larger, which suggests the technique is capable of distinguishing this difference.

Finally, I attempted to address how the combination of multiple SEM images affects the results of the analysis in section 2.3. In this manner the SEM results may better approximate the GID measurements, since the SEM results would include a larger film area. The intent was to 1.) see how consistent is the peak location when taking into account a large area of the film and 2.) how big of an effect compounding film defects had on the resulting analysis.

To heighten the effect of defects on the results a film was deposited and then disturbed by rapid lateral compression prior to Langmuir-Schaefer stamping. This fast compression resulted in poor uniformity of the film, though ordered domains were still present. A series of SEM images were collected with the same magnification and exposure settings from across many millimeters of film area. Figure 2.18 contains several examples of the images.

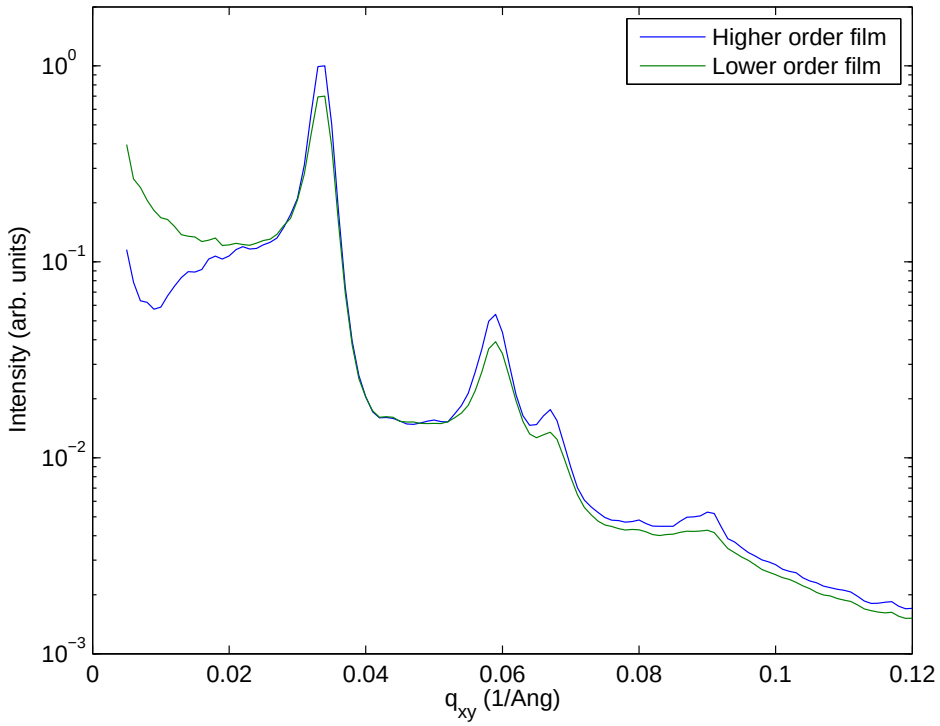

Figure 2.17: Comparison of the FFT and angular integration analysis performed on the two images in Figure 2.16. The more disordered SEM image (that on the right) is plotted in green and the less disordered image (that on the left) is plotted in blue.

The the FFT analysis was then performed on 20 of the images, all of which appeared to have similar features, by eye. The analysis results from the 20 images were then averaged together and compared to that of a single image. The results are seen in Figure 2.19. By linearly superimposing the q-space results I assume that the contributions from different areas of the film contribute incoherently. Given that the transverse coherence length at Sector 15ID-C at APS is less than 1 μm (smaller than the width of the SEM images) then the incoherent superposition makes for a more accurate comparison to GID.

It is clear from the resulting comparison that the compounding defects have a major affect on the contrast of all the Bragg peaks. But the peak locations are very consistent. This suggests the average inter-particle spacing is relatively uniform over a large region.

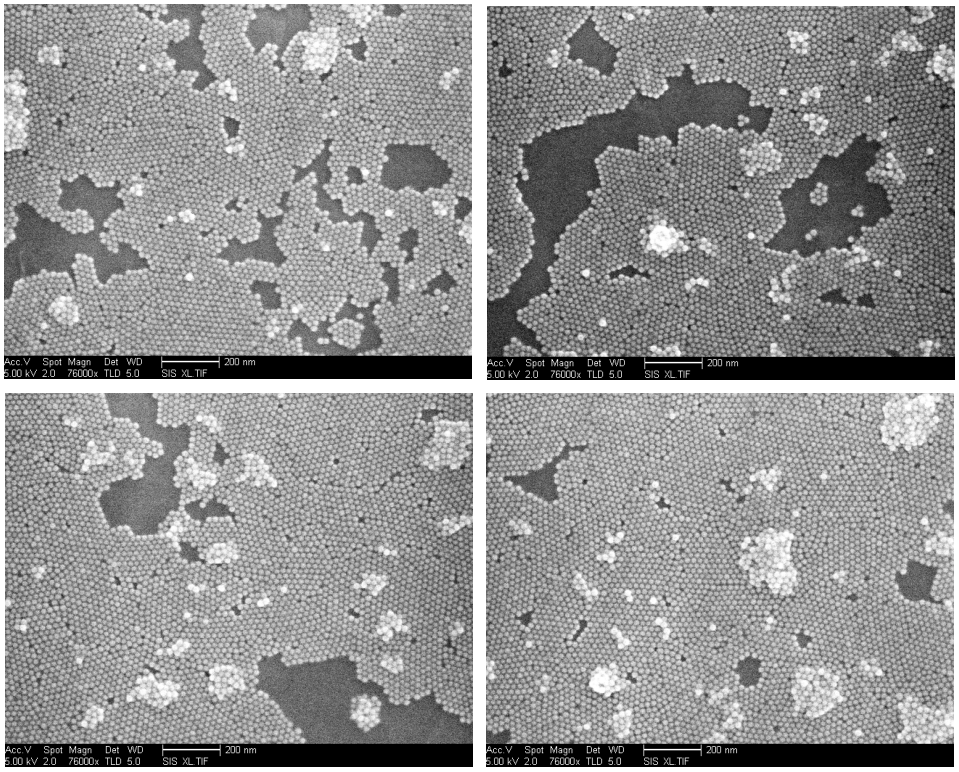

Figure 2.18: Examples of different SEM images with a high degree of disorder which were used in the composite result, which can be seen in Figure 2.19.

The text of Chapter 2, in part, is a reprint of material as it appears in: J. Stanley, Y. Dai, L. Boucheron, B. Lin, M. Meron, O. Shpyrko, "Novel comparison of microscopy and diffraction techniques on the structure of iron oxide nanoparticle monolayers transferred by Langmuir-Schaefer method", *Review of Scientific Instruments*, (submitted for publication), 2014.

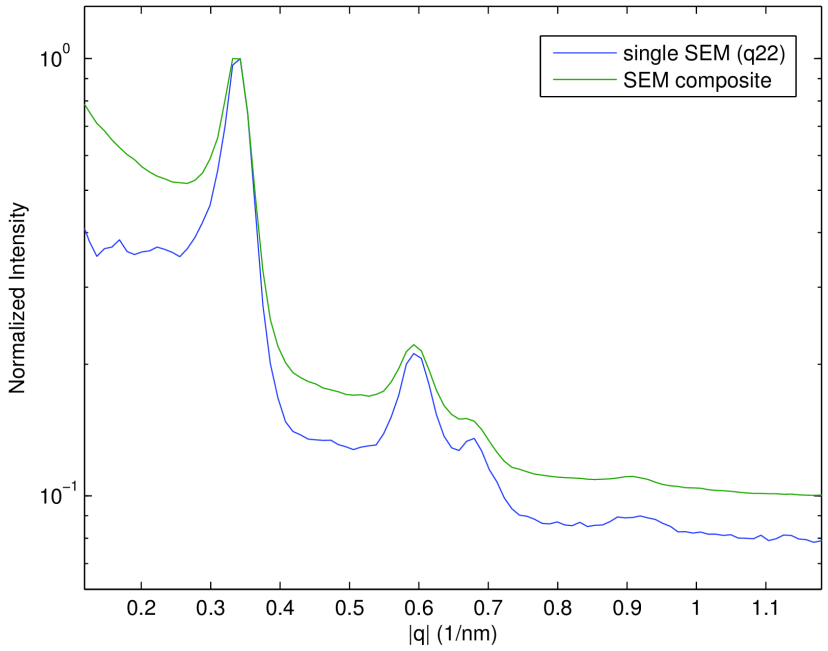

Figure 2.19: Comparison between the SEM analysis on a single image and that averaged together from 20 images.

Chapter 3

In-Plane Structure (GID and Microscopy)

The following chapter discusses the nature of the in–plane structure of the self–assembled nanoparticle films, both after self-assembly and during the lateral compression. To do so I utilize the surface pressure, monitored with the Wilhelmy plate pressure sensor discussed in section 1.2 as a macroscale measure of the system, which is complimented by *in-situ* visible microscopy to correlate the microscale appearance of the film with its surface pressure. Additionally, SEM is used to see the structure of the film at the particle level. Since SEM cannot be performed in-situ, the transfer technique discussed in section 2.5 will be used to prepare the sample for SEM. Finally, the interparticle spacing and domain size throught the compression will be quantified by the use of GID *in-situ*, which provides a global average of the film behavior by virtue of the large illumination film area.

3.1 Isotherm and Microscopy Data

The isotherm (liquid surface area vs. surface pressure Π) due to lateral compression for the nanoparticle films, consist of three separate phases: the initial low density phase, the intermediate phase, and the multilayering "collapsed" phase. A characteristic isotherm with the labeled regions can be seen in Figure 3.1. [44, 60, 66, 67]

The initial phase is characterized by constant $|\mathrm{d}\Pi/\mathrm{d}A|$, which is at its minimum value. As the film is further compressed $|\mathrm{d}\Pi/\mathrm{d}A|$ begins to increase - this marks the start of the intermediate phase, at around $70 - 80\%$ the initial area. During the intermediate phase $|\mathrm{d}\Pi/\mathrm{d}A|$ continues to increase to its maximum value and eventually becomes constant. The final phase ("collapsed phase") begins once $|\mathrm{d}\Pi/\mathrm{d}A|$ begins to decrease, which occurs around $30 - 45\%$ of the initial area.

The area at which the transitions between the different isotherm phases occurred depended on the amount of solution initially deposited on the water's surface. A standardized volume was used for the extent of this work. In order to compare between 10 and 20 nm the amount of solution was used that represented the same cross-sectional particle area per unit of liquid surface area.

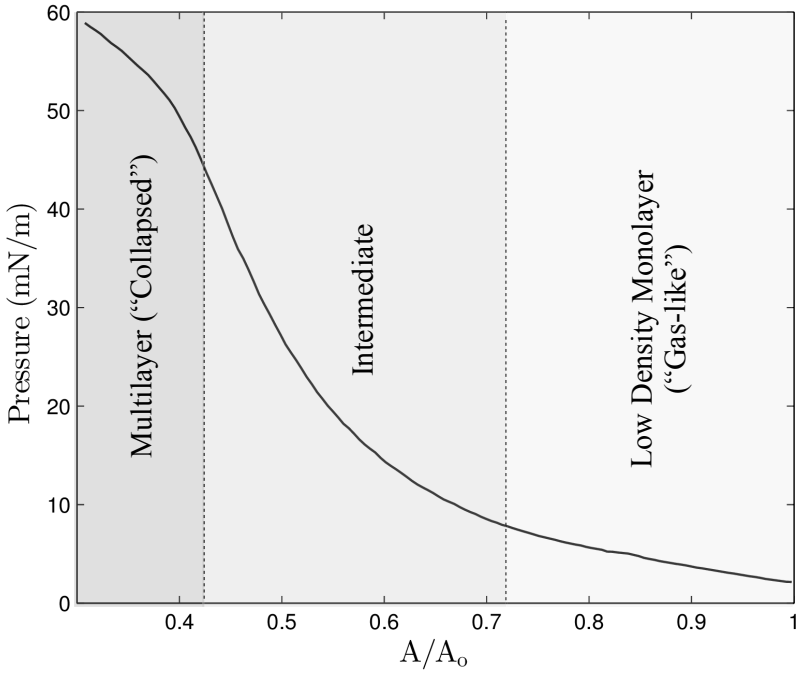

Figure 3.1: A diagram of a characteristic isotherm showing the different phases of the film compression. $\mathrm{A_o}$ is the initial liquid surface area available to the film prior to compression (for the trough at Sector 15ID-C this was $\mathrm{A_o} = 338.1\,\mathrm{cm}^2$).

The macroscale pressure measurements were complimented by *in-situ* visible microscopy which was performed using a conventional microscopy with a 100x objective. The microscope was positioned over the Langmuir-Blodgett trough which had a glass window in the bottom through which the liquid surface film could be back-lit. A white light sources was positioned below this window. The trough was filled and the liquid surface was adjusted into the focal plane of the objective. The nanoparticle film was then deposited. A digital camera was integrated into the output of the microscope which was computer controlled to capture still frames of the film during the compression. Unlike the trough at Sector 15ID-C the microscopy trough possessed two opposing barriers which compressed toward the center at equal rates. The objective was approximately located over the geometric center of the trough so that the examined film region was roughly stationary.

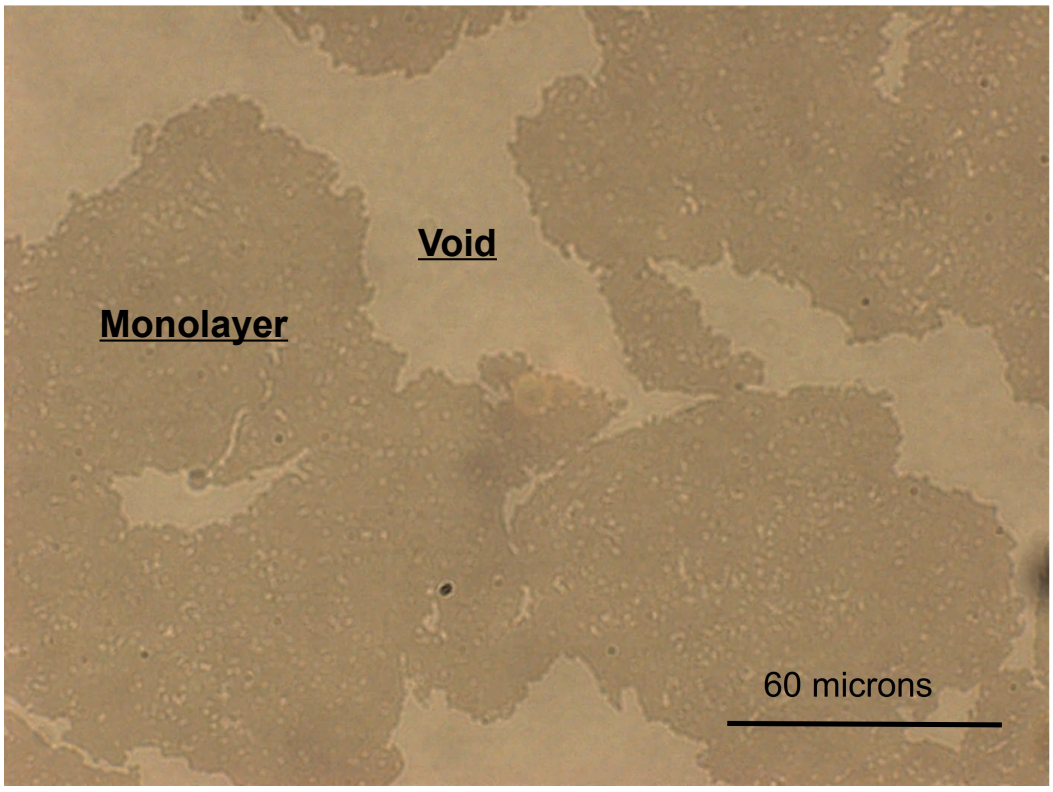

Figure 3.2: Visible microscopy of a stamped uncompressed monolayer. Visible are the bare subphase voids present between contiguous assembled regions. These large voids are closed during the initial compression phase.

Figure 3.2 is a micropscopy image taken of the film during the low density phase. At this length scale there are two major features visible: the 'void' regions which are uncovered suphase regions and the 'monolayer' regions which are the self–assembled film. During the initial compression the large 'void' regions are closed as the 'monolayer' regions are brought together. The 'monolayer' regions have minimal interaction during this process - the result is a linear change in pressure.

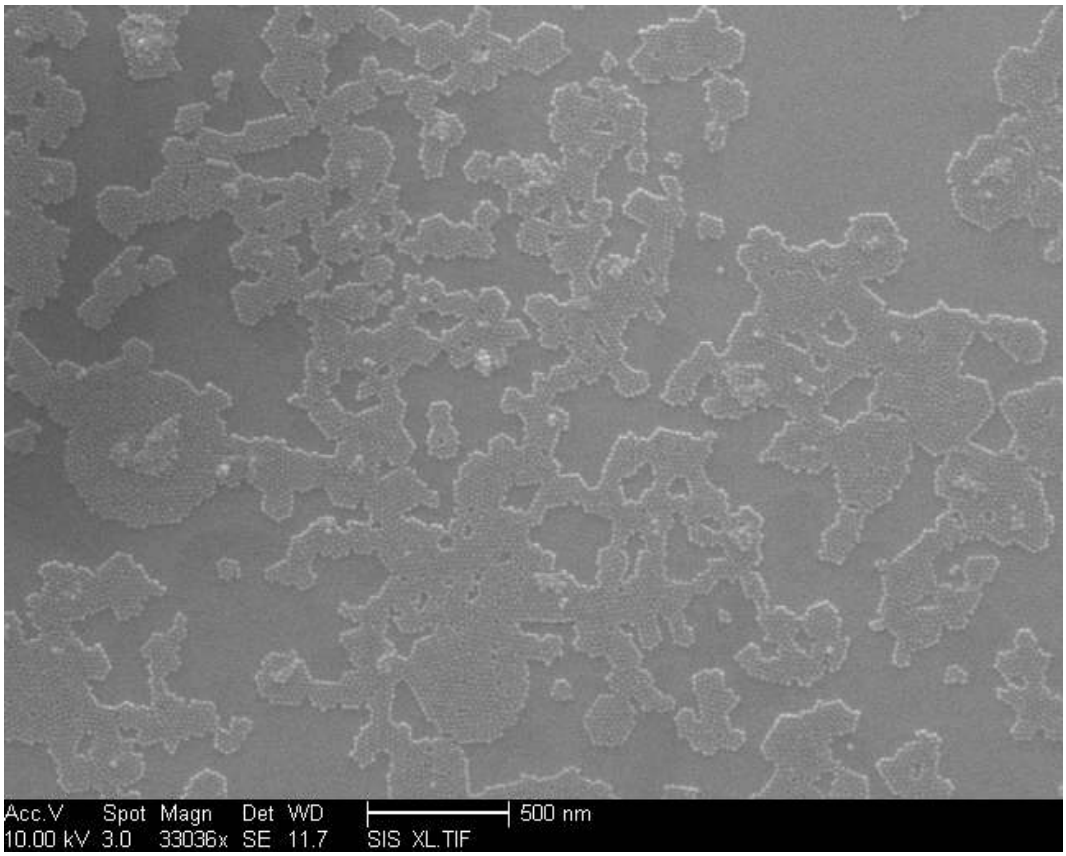

Figure 3.3: SEM of a stamped uncompressed monolayer. Field of view is contained in the 'monolayer' regions of Figure 3.2. Film does not form a *uniform monolayer*. The number of particles deposited is only sufficient to cover a fraction of the water's surface.

Using the Langmuir-Schaefer transfer method and SEM the details of the the 'monolayer' regions can be better understood. Figure 3.3 shows a detail of the 'monolayers' region (equivalent to that seen in Figure 3.2) of an uncompressed 20 nm film. A network of well–ordered domains are visible with comparably sized

gaps between them. The domains appear to be approximately a few hundred nanometers in size. These domains appear chained together in a network–like fashion and thus behave as a contiguous film, despite the visible gaps. These gaps are distinct from the large voids in Figure 3.2, as they are internal to the 'monolayer' and are 100-1000 times smaller.

The intermediate phase begins once the voids in Figure 3.2 have been removed, at which point the 'monolayer' regions begin confining one another and stress develops at the interface between them. [68] The smaller gaps seen in the SEM image of Figure 3.3 gradually close throughout the intermediate phase. At this point the film is effectively a uniform monolayer - as seen in Figures 2.3 and 2.16. Once these gaps between the ordered domains have been closed, further compression causes the film to be forced out of the plane, resulting in multilayering structures (seen in Chapter 4. This occurs sporadically throughout the intermediate phase and finally the "collapsed" phase begins when this multilayering exists across most of the film.

3.1.1 Isotherm Variability

Though all of the general characteristics of the isotherm for these films are reproducible, the random nature of the drop–casting deposition process can result in variability of the isotherm. To measure this variability multiple films were prepared using the same process. All films had the same starting liquid surface area, and the liquid surface was checked for impurities prior to film deposition by compressing the bare water surface and verifying that this did not change the surface pressure. All films had the same volume of solution deposited, and the drop–casting was done in a randomized fashion, pausing several seconds between each drop for the chloroform to partially evaporate. The films were then allowed to come to equilibrium for approximately 60 minutes. Then the films were compressed at a rate of $2.0\,\mathrm{cm}^2/\mathrm{min}$. The results of these isotherms can be seen in Figure 3.4. Note that the isotherms are in good agreement during the low density phase but begin to diverge in the intermediate phase. By 50% compression the variance of the pressure is $\sim 5\,\mathrm{mN/m}$.

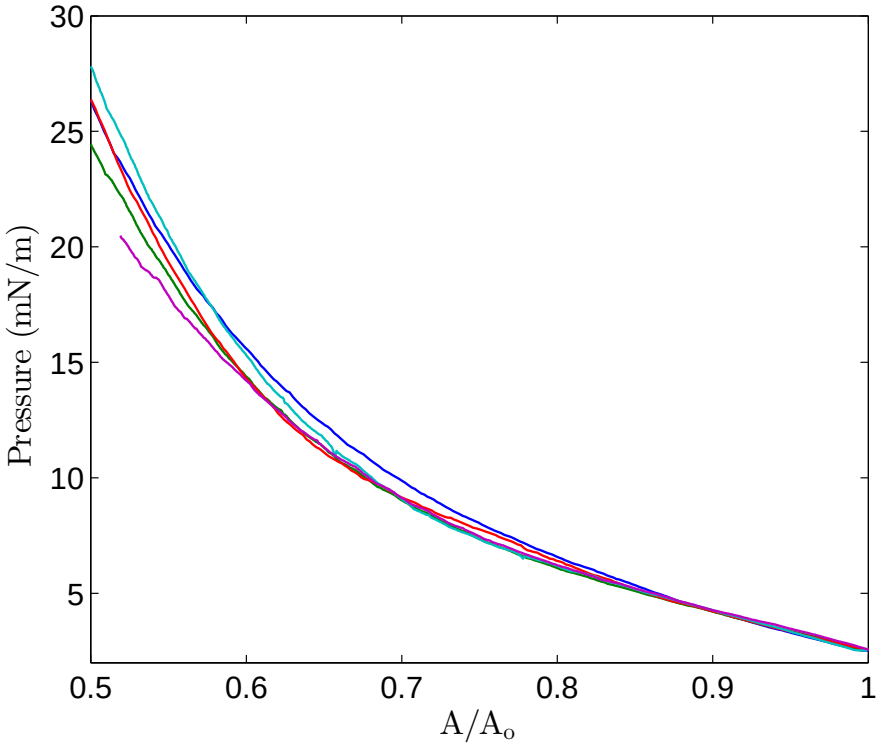

Figure 3.4: A comparison between five different 20 nm films, all assembled in the same manner and compressed at the same rate. Low density state shows little variability, but as the film density is increased, the pressure values begin to diverge.

It's at the point when the drops are randomly deposited that the irregularity of the films likely occurs. Though the macroscale structure of the film is the same, the local environment at the microscale and smaller is highly irregular. Similar systems have been observed to exhibit intrinsically glassy structure/dynamics. As these systems are compressed a jammed state is formed which results in irregular strain across the film - this results in domains of differing pressure. This strain is the result of the shear interaction between the small ordered domains of the film. [9, 69–74] This is a feasible model to describe the iron oxide nanoparticle films as well. The Wilhelmy plate only experiences the pressure in the region directly around where it intersects the water's surface. Therefore the pressure value it records is not fully representative of the average pressure of the entire film. However, as long as the variability seen in Figure 3.4 is accounted for in the

uncertainty of the pressure measurement, then the Wilhelmy plate is a suitable measure of the global state of the film.

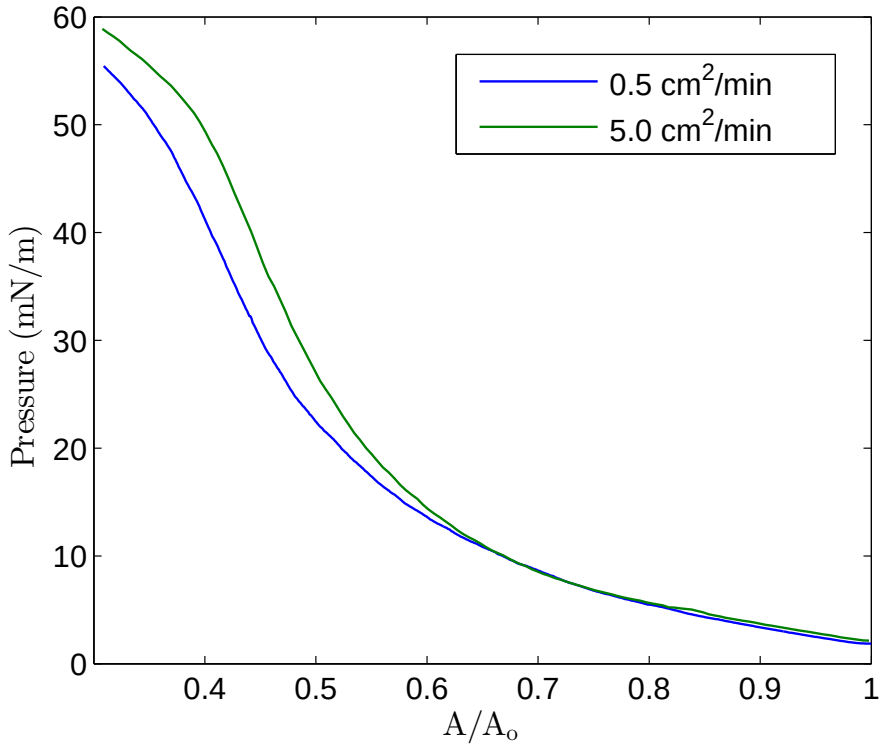

Figure 3.5: Isotherms of two equivalently prepared 20 nm films with different compression rates. Low density region shows little difference but the pressure differs for higher densities. The difference is not significant in light of the variability seen in Figure 3.4

The rate of lateral compression is a potential source of variability in the isotherm. To test this multiple isotherms were collected on films formed in the same manner as described above, using differing compression rates. Figure 3.5 shows the comparison of two isotherms, one having been compressed at 0.5 cm^2/min and the other at 5.0 cm^2/min. The variability between these two is within the variation seen in Figure 3.4, therefore the compression rate within this range does not appear to have a significant effect on the isotherm.

3.2 Grazing Incidence Diffraction (GID)

GID provides a compliment to the qualitative information obtained from the pressure and microscopy measurements - obtained from GID are high precision measurements of the average interparticle spacing and correlation length of the ordered nanoparticle domains within the film. The beam size, which is $20\,\mu\text{m} \times 120\,\mu\text{m}$, results in an illuminated film area of $20\,\mu\text{m} \times 7.6\,\text{cm}$. This large scattering volume acts as a sufficient sample to accurately represent the statistical average film structure.

Figure 2.2 is an example of the two dimensional GID data from a 20 nm monolayer. The presence of the first through fifth order GID peaks suggests that the film is highly poly–crystalline, with all grain orientations present in the illumination area - therefore grains exist to satisfy all bragg angle conditions for the incident beam. [36] The 2D data is then integrated along the q_z. This does not effect the GID peak shape since the peak location/shape do not depend on q_z. Examples of the resulting integration are in Figures 2.5 and 5.2.

This 1D data (GID peak intensity as a function of q_{xy}) can then be fit to extract the peak location and width, from which the physical parameters about the film can be extracted. The fitting process used for the GID data is discussed in sections 5.4 and 5.7.3. Gaussian functions are used for each peak and the background is fit with a quadratic spline. GID data was collected at various stages throughout the compression. The following sections describe the result for the 20 nm films.

3.2.1 Inter-Particle Spacing

The peak locations of all five GID peaks are consistent with a hexagonal close packed lattice as outlined in Table 1.1. All five peak locations provide information about the interparticle spacing within the hexagonl close packed film. The first GID peak, being of the highest signal, was fit for several measurements at different degrees of lateral compression. The q_{xy} value of the the peak location as a function of compression is plotted in Figure 3.6.

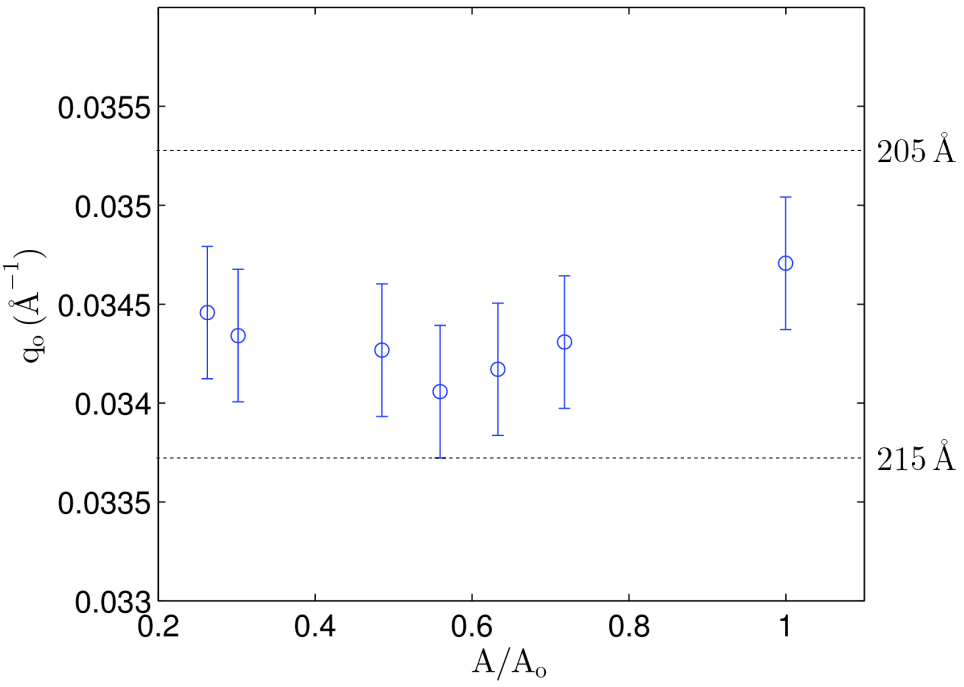

Figure 3.6: A plot of the q_{xy} peak location (from the fitting results) of the first order GID peak from a 20 nm film during compression. The dashed lines denote interparticle spacing corresponding to the value of q_o.

It's clear from the plot that the peak location is constant (within the confidence intervals) throughout the compression, therefore compression has little effect on the interparticle spacing of the film's constituents. The interparticle spacing is effectively determined by the intial self–assembly. The average peak location during compression is $q_o = 0.0344\,\text{Å}^{-1}$ which corresponds to an average interparticle spacing of $D = 210.9\,\text{Å}$.

3.2.2 Domain Size

In addition to interparticle spacing the peak width can be extracted from the fitting and utilized to determine the correlation length of the ordered scattering regions. The relationship between peak width and correlation length is given by

the Scherrer equation [75]

$$L = \frac{K\lambda}{\beta \cos\theta} \tag{3.1}$$

where $K \approx 0.9 - 1.1$ is a dimensionless shape constant, λ is the X-Ray wavelength, θ is the Bragg angle, and β is the full–width half maximum of the Bragg peak.

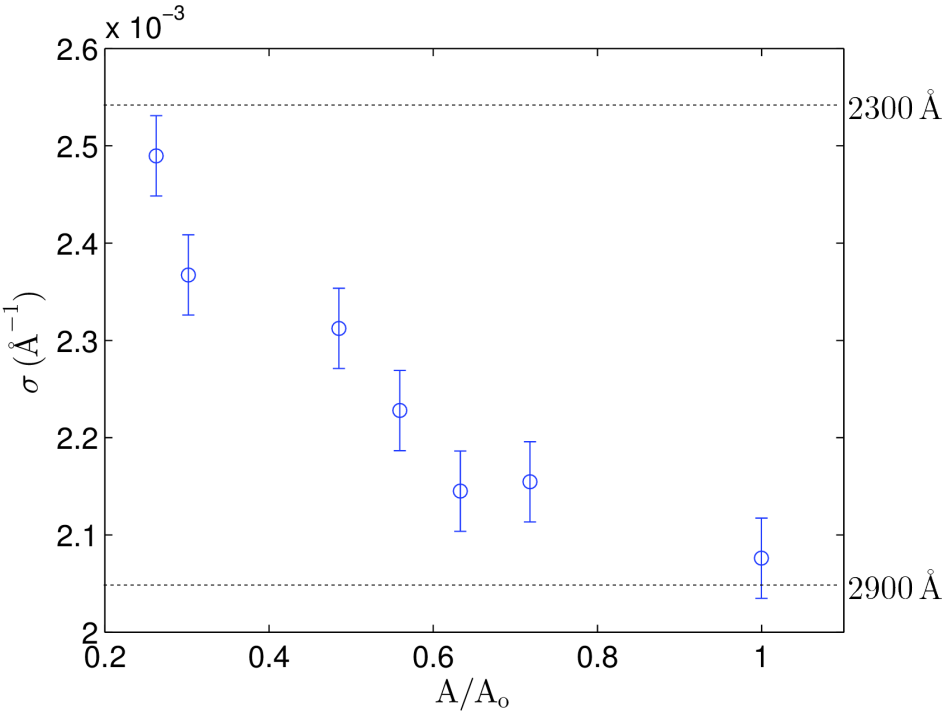

Figure 3.7: A plot of the width of the first order GID data from a 20 nm film during compression. The dashed lines mark the domain size corresponding to the peak width.

The fitting parameter corresponding to the Gaussian width (σ) can be used to calculate the FWHM, but first the instrumental resolution must be subtracted off. The total peak width is the result of the finite q_{xy} resolution of the detector in addition to broadening due to the finite size of the ordered domains. It is the later which must be isolated in order to calculate the FWHM. Further explanation can be found later in sections 5.4 and 5.7.3.

The resulting peak width due to broadening as a function of compression is plotted in Figure 3.7. The two dashed lines represent the upper and lower bounds on the linear dimension of the average ordered domain within the film,

as calculated from the Scherrer equation. As you can see the average domains are initially about 2900 Å and as the film is compressed this size monotonically decreases to 2300 Å. This is likely explained by shear forces that arise between monolayer regions (those seen in Figure 3.2) as they are compressed together. This results in strain and ultimate dislocation of the ordered regions that comprise these monolayer regions (those domains seen in Figure 3.3). Further compression results in a greater degree of dislocation and inclusion of defects, which result in ever smaller ordered film regions.

3.2.3 GID Sample Damage

The exposure of the film to extended periods of high energy radiation can cause two possible types of damage: 1.) ionizing damage due to the high photon energy and 2.) thermal damage due to to total energy deposited. The likely effects of this damage are 1.) the removal of oleic acid from the particle by way of breaking its bond to the nanoparticle surface and 2.) the sintering of the nanoparticles that are in contact with one another. Both of these may disrupt the structure of the film and result in a change in the GID peak position, shape, and intensity - therefore an upper limit on the total exposure had to be established to minimize the damage.

To determine the maximum radiation dosage which would still preserve the film structure, successive GID measurements were taken, scattering from the same film region each time, with long exposure times. These measurements are plotted in Figure 3.8. As you can see the peak intensity and location are effected by the high radiation dosage - the peak shifts toward high–q and the peak intensity drops. The shift toward high–q implies that the oleic acid is being removed from the nanoparticles which can then group more closely.

The 500 second measurement has the same peak location and amplitude as the typical GID measurement. The maximum exposure time used for the GID measurements was 400 seconds.

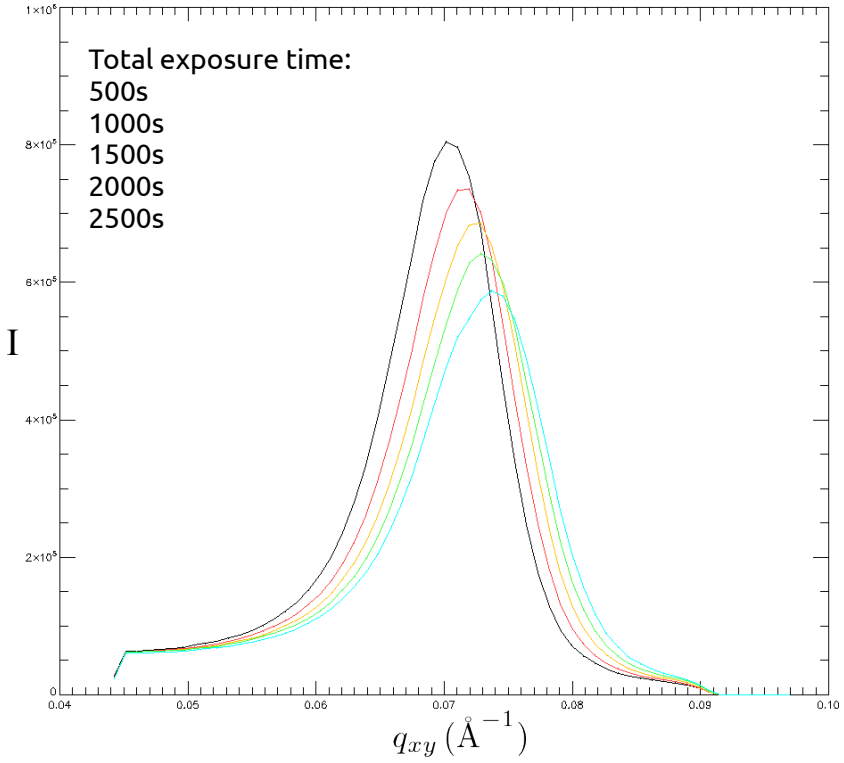

Figure 3.8: First order GID peak of a nanoparticle film showing the effects of extended X-Ray exposure (black: 500 seconds exposure, teal: 2500 seconds of exposure). The illuminated film region was held constant throughout the exposure.

3.3 GID Form Factor

The GID peak locations provided information about the interparticle spacing but in order to measure the spacing between the particle surfaces the true size of the particles needed to be determined. Nominally the particles were 20 nm in diameter, as specified by the manufacturer. To verify this, analysis of the form factor, extracted from the 2D GID data was performed. The form factor $|f(\mathbf{q})|^2$ for a uniform sphere is given by equation 2.14, and its approximate contribution to the overall intensity pattern is shown in equation 2.4.

The form factor was extracted at $q_{xy} = 0.0344\,\text{Å}^{-1}$ which is the maximum

intensity of the first order GID peak. Here the form factor oscillations along q_z were most prominent. The model used to fit these oscillations (equation 3.2) was the convolution between a broadening gaussian (fitting parameter: peak width σ) and equation 2.14 (fitting parameter: radius R). The third fitting parameter was a scaling amplitude.

$$F(q; A, R, \sigma) = A\left[|f(q, R)|^2\right] * \left[e^{-q^2/2\sigma^2}\right] \tag{3.2}$$

The top plot of Figure 3.9 shows the extracted form factor oscillations (green points) and the fit using equation 3.2. The bottom plot shows the radius values that result from the fitting for the film at various degrees of compression. The error bars are the manufacturer's estimates on the poly dispersity. The average radius is $R = 9.79 \pm 0.05\,\text{nm}$. Therefore the average spacing between particles is given by:

$$\delta = D - 2R = \frac{4\pi}{0.0344\sqrt{3}} - 2(97.9) = 15.1\,\text{Å} \tag{3.3}$$

The text of Chapter 3, in part, is a reprint of material as it appears in: J. Stanley, L. Boucheron, Y. Dai, S. You, B. Lin, M. Meron, O. Shpyrko "Evolution of in–plane and out–of–plane structure of nanoparticle Langmuir monolayers under lateral compression", (in preparation), 2015.

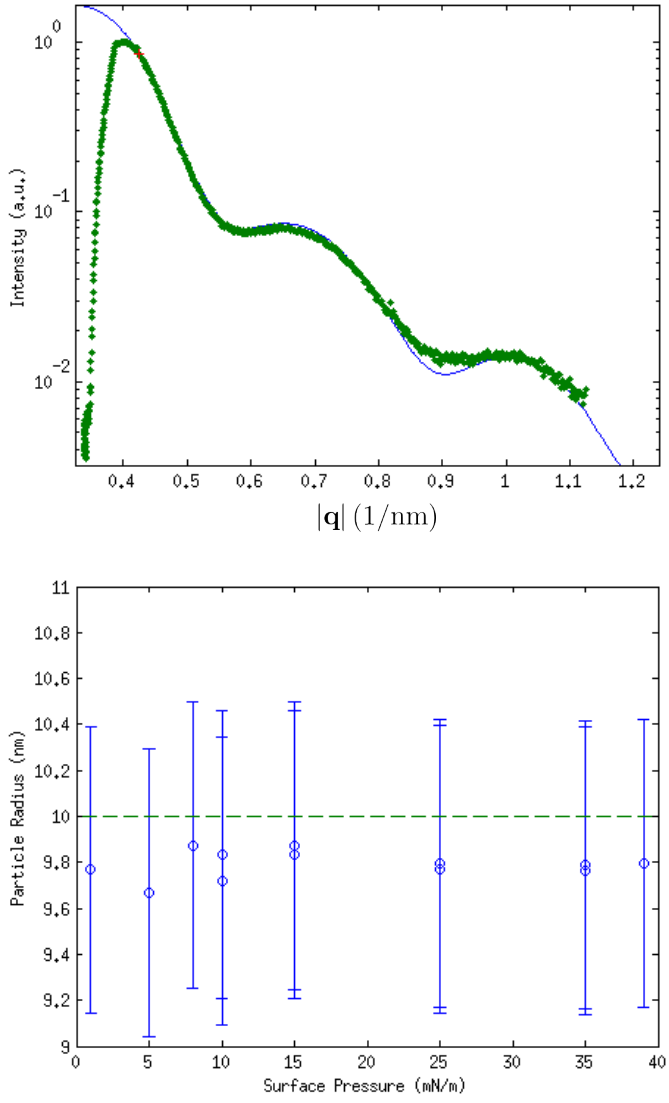

Figure 3.9: Top: A plot of I vs. $|\mathbf{q}|$ (1/nm) along the q_z at the first GID peak (green points) and the form factor fit (blue curve) using equation 2.14 convolved with a Gaussian. The red point - start of the fitting region. Bottom: R fit parameter.

Chapter 4

Out-of-Plane Structure (XR and GIXOS)

This chapter is a reproduction of a manuscript currently in production to be submitted to *Journal of Applied Physics*.

The lateral compression of Langmuir-Blodgett films has been a facet of inter–facial science for numerous decades and some of this work has been focused on the conformational changes of the films in the out–of–plane direction, and how this structure depends on the constituents of the film. The building blocks that have been studied have ranged in size, chemical composition, shape, surface coating, and chemical reactivity. [10, 76] Research of this kind, on metallic nanoparticle films, using precision X-Ray techniques has only been performed in the past few years. Thus far these films have demonstrated markedly different behaviors resulting from only minor differences in the film constituents. In these metallic nanoparticle systems, the development of out–of–plane structures depends on many factors, which determine whether the formation of bi–layers, tri–layers, buckles, or folds occur. [9, 13, 58, 77, 78].

This chapter covers *in-situ* measurements from visible microscopy, collected during compression, which show varying particle-size dependent structures at the micron length scale and larger. These are followed up with *in-situ* X-Ray measurements (both X-Ray Reflectivity and Grazing Incidence X-Ray Off-Specular Scattering) which are used to probe the submicron nature of these structures and

relate the behavior at this length scale to that observed using visible microscopy. Finally, the connection between the visible microscopy and X-Ray measurements are corroborated by way of *ex-situ* SEM measurements, utilizing the Langmuir-Schafer transfer process described in Chapter 2.

The lateral compression of Langmuir-Blodgett films was performed using the motor controlled teflon barrier seen in Figures 1.3 and 1.4. As discussed in Chapter 3 the film which, after the initial deposition, consisted of self-assembled patches with interstitial blank subphase in between - shown in Figure 3.3. These patches are group together into roughly uniform regions of film that are on the order of tens of microns. These film regions are then separated by large voids of bare subphase (Figure 3.2). The lateral compression of the barrier then consolidated these film regions by reducing the over all available area, eliminating the voids. After a given amount of compression the majority of these large film regions had been consolidated into an inter–connected macro–scale monolayer. This occurred at some point during the intermediate compression phase, shown in the isotherm of Figure 3.1. At this stage of compression the film is considered a *uniform monolayer*. Further compression results in a greater rate of increase in film pressure, during which the smaller blank regions, interstitial to the self-assembled domains are closed up (those seen in Figure 3.3). It is during this point in the intermediate phase that the transition from monolayer to multilayer is initiated. From this point on in the compression, the various measurements are used to discern the nature of the developing out–of–plane structure.

4.1 Microscopy

At a point late in the intermediate phase of compression the multilayering becomes detectable using visual miscroscopy. The multilayering occurs sporadically and non-uniformally throughout the film. Sn order to capture this behavior, further compression of the film to the point that it enters the "collapsed" phase (seen in Figure 3.1) will grantees a greater fraction of the film has transitioned to a multilayer and therefore is more likely to be captured in the field of view.

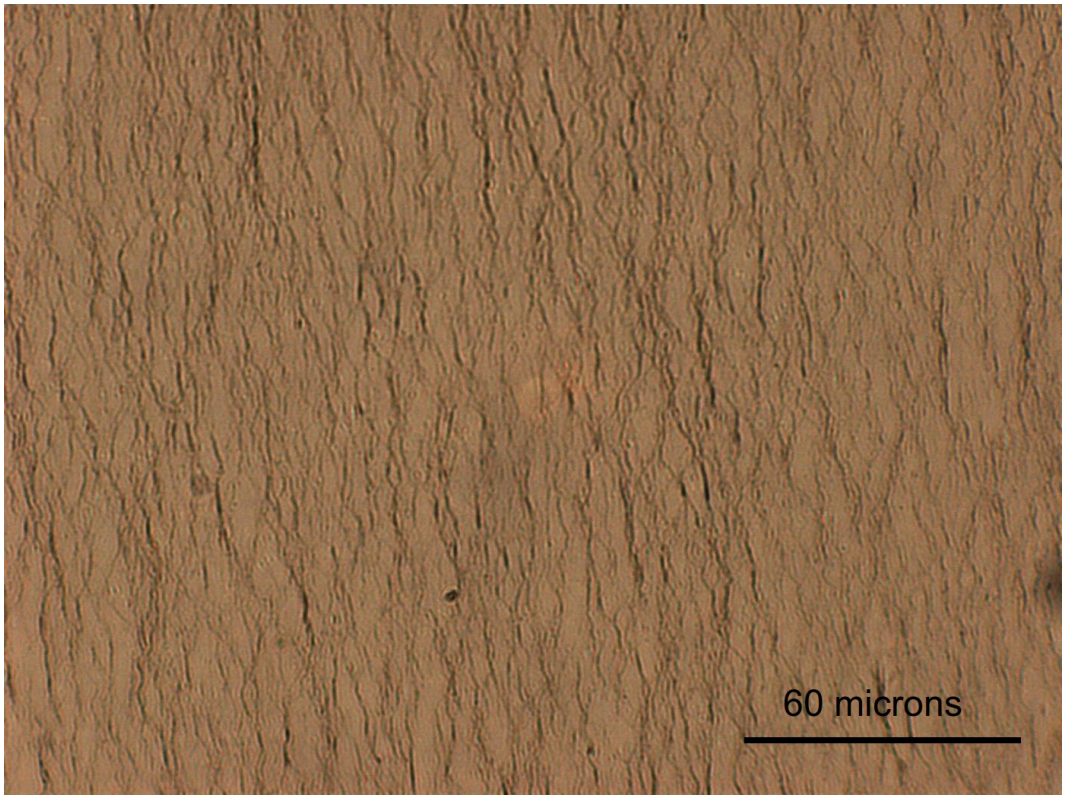

Figure 4.1: A microscopy image of a highly compressed 20 nm nanoparticle film showing several different multilayering morphologies. The compression direction is along the horizontal.

Visible microscopy was performed *in-situ* using a conventional microscopy with a 100x objective. The microscope was positioned over the Langmuir-Blodgett trough which had a glass window in the bottom through which the liquid surface film could be back-lit. A white light sources was positioned below this window. The liquid surface was adjusted into the focal plane of the objective and the film was subsequently deposited. A digital camera was integrated into the output of the microscope, which could capture still frames of the film during the compression.

Figure 4.1 shows a microscopy image of a *20 nm nanoparticle monolayer* which has been compressed into the "collapsed" phase - a compression ratio of $\sim 30\% \, (A/A_o)$. The out–of–plane structures take up a large fraction of the film area and are quite uniformly distributed. The compression of the film was in the horizontal direction and, on average, these structures are oriented parallel to the

barrier. These structures possess an irregular, sinuous shape that vary in lengths of $1 - 10\,\mu$m. It is unclear from this and other microscopy images what is occurring, on the particle length scale, to form these out–of–plane structures. It's possible these could be 'kinks' at the level of individual particles, which has been proposed for other nanoparticle films. [58,77] In the image of Figure 4.1, by eye there appears to be preferential angles to the bends seen in the sinuous structures, which would suggest this behavior is tied to the lattice orientation and therefore a product of the granularity. Alternatively, if the width of these out–of–plane deformation is much larger than the interparticle spacing then it is possible their formation is better described by the folding of a continuum medium such as an elastic membrane. Additionally, it cannot be determined from the microscopy data if the out–of–plane structures in the 20 nm films are pushed up out of the plane or down into the subphase. [67]

On the other hand, Figure 4.2 shows a microscopy image of a *10 nm nanoparticle monolayer* which has been compressed into the "collapsed" phase - a compression ratio of $\sim 0.30(\mathrm{A/A_o})$. The compression of the film was in the horizontal direction. The most apparent characteristic is that the orientation of the multilayering conforms to the direction of compression and possess long range order along this direction. These structures extend well beyond the frame of the image - upwards of several millimeters in length. Based on the analysis of grain size in Chapters 3 and 5 this these millimeter length structures are approximately 10,000 times the linear dimension of the average ordered-grain.

The behavior of the 10 nm film is much more indicative of a continuum medium than is the 20 nm film, given the extended length of the out–of–plane structures formed. Also unlike the 20 nm film, which showed the appearance of just one type of structure, multiple different types of structures can be see in the 10 nm film image: multiple different shaded regions suggesting bi– or trilayers formed from a split/subtending in the film or an s-folding [58]; dark thin regions that could be the result of crinkling or buckling. The specific nature of these structures cannot be determined from microscopy alone.

In order to determine the nature of these out–of–plane structures in both

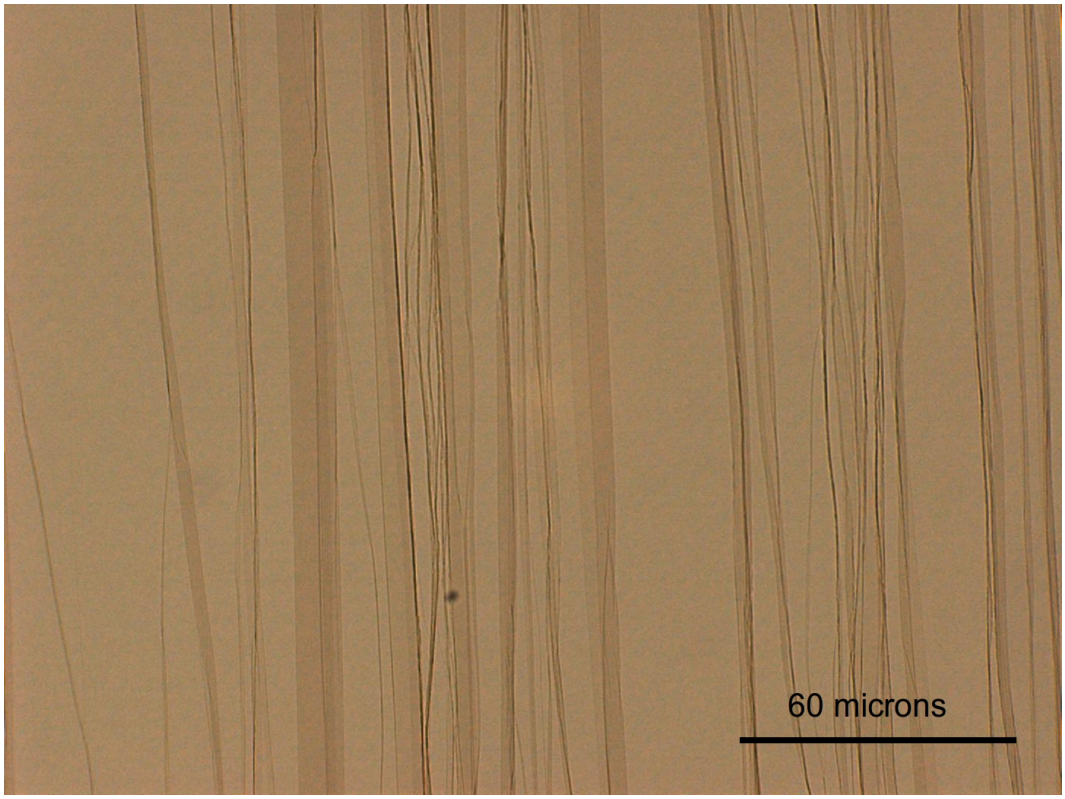

Figure 4.2: Microscopy image of a highly compressed 10 nm nanoparticle film showing different multilayering morphologies. These appear characteristically different from those of the 20nm film. The compression direction is along the horizontal.

the 10 and 20 nm films we move on to the X-Ray techniques.

4.2 X-Ray Reflectivity

The reflectivity measurements required the movement of the angle of the incident beam (which determined α), the detector orientation (which determined β), and the height of the trough (which maintained the location of the beam spot) all in concert with one another. The data sets consisted of approximately 160 points with each point having an exposure time of $3 - 5\,\mathrm{s}$ and an additional 5 s for read out and motor movement. Therefore a single reflectivity scan took approximately 25 minutes.

The beam size (as defined by the incident beam slits) was 2 mm horizontal

by 0.02 mm vertical - the incident angle ranged from 0.18 to 1.42 degrees during the scan corresponds to a footprint length of 6.4 mm to 0.8 mm. Thus the total beam footprint (illuminated film area) was of maximum area 12.8 mm^2. Electronic slits of dimension 17×5 pixels were used to define the detected reflectivity signal. This corresponded to an area on the detector of $2.92 \times 0.86\,mm^2$ which was positioned at a distance of 567.0 mm.

4.2.1 20 Nanometer Nanoparticle Film

If the out–of–plane structures formed from compression are at the granular scale then it's possible that the multilayering would occur in discrete units - from monolayer to bilayer to trilayer, etc. Alternatively, if the film behaves as a continuous medium and buckles or folds then the discrete transition in layers should not should not be present in the reconstructed average electron density. With this in mind, I move on to the reflectivity data.

Due to the time required to collect a complete reflectivity measurement the film could not be continually compressed during data collection. Instead the compression was paused intermittently throughout the total compression range - the same process carried out in Chapter 3 when collecting the GID data during compression.

Figure 4.3 shows the reflectivity data from a compressed 20 nm film at different degrees of compression. As the film was compressed the Kiessig fringes appear to monotonically decrease in contrast but the periodicity remains the same. The uncompressed scan had a distinctly different shape than of the rest - this was likely due to the incomplete surface coverage of the film after deposition (seen in Figure 3.2), therefore the film was not likely to be uniform within the area illuminated by the beam.

The reflectivity data was first normalized by the Fresnel reflectivity, equation 1.33, in which q_c was calculated from the critical angle for water (equation 1.28). The fresnel normalized reflectivity could then be fit using the piece-wise defined model, as described in Section 1.5, and the Master-Formula (equation 1.38. The iterative fitting was performed using a standard routine in CPLOT.

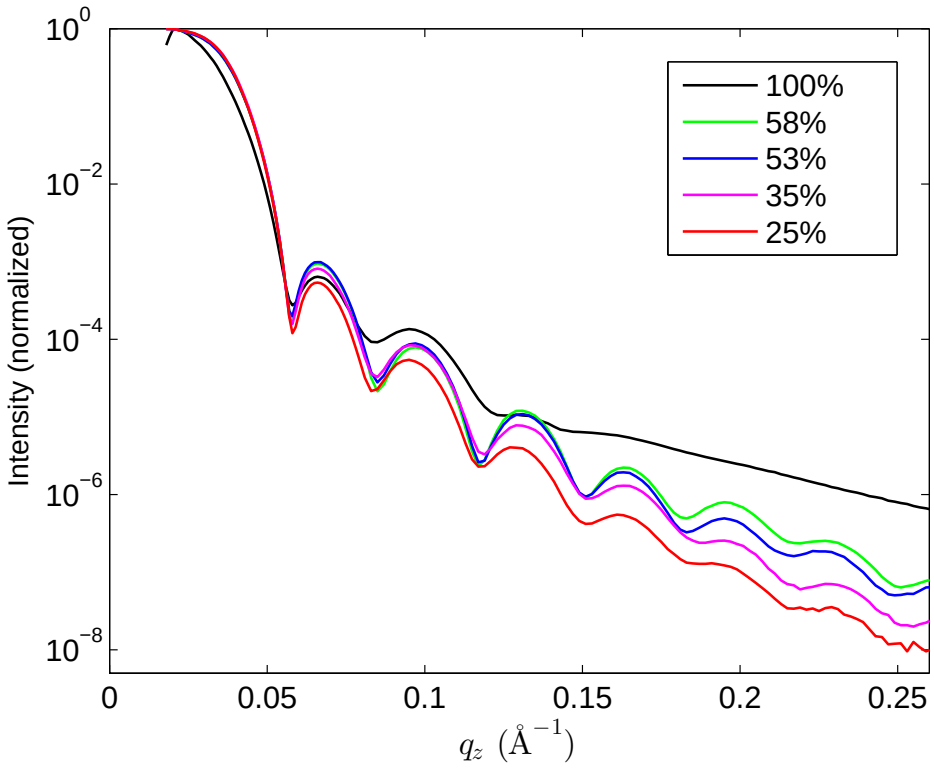

Figure 4.3: Reflectivity from a compressed 20 nm film at different areas, relative to the initial area. Uncompressed film (100%) appears different than compressed scans - likely due to incomplete surface area coverage. Data is normalized by the Fresnel Reflectivity.

Initially the fitting was attempted with the simplest model: a single "box" consisting of a top and bottom surface roughness, a density and a thickness. Since the film would assumed to be a monolayer this starting point model was physically motivated. However, this model did not demonstrate good convergence - specifically it not well describe the higher–q portion of the data. The model's complexity was systematically incremented by the inclusion of additional "boxes" (1 roughness parameter, 1 density parameter, and 1 thickness parameter per box) and the fitting re-run until good convergence was obtained. The phenomenological model required to accurately fit the reflectivity data was an "8-box" model. Results of this fitting can be seen in Figure 4.4 where the least compressed (barring the uncompressed data set) and the most compressed data sets (from Figure 4.3) are shown with the resulting "8-box" fit.

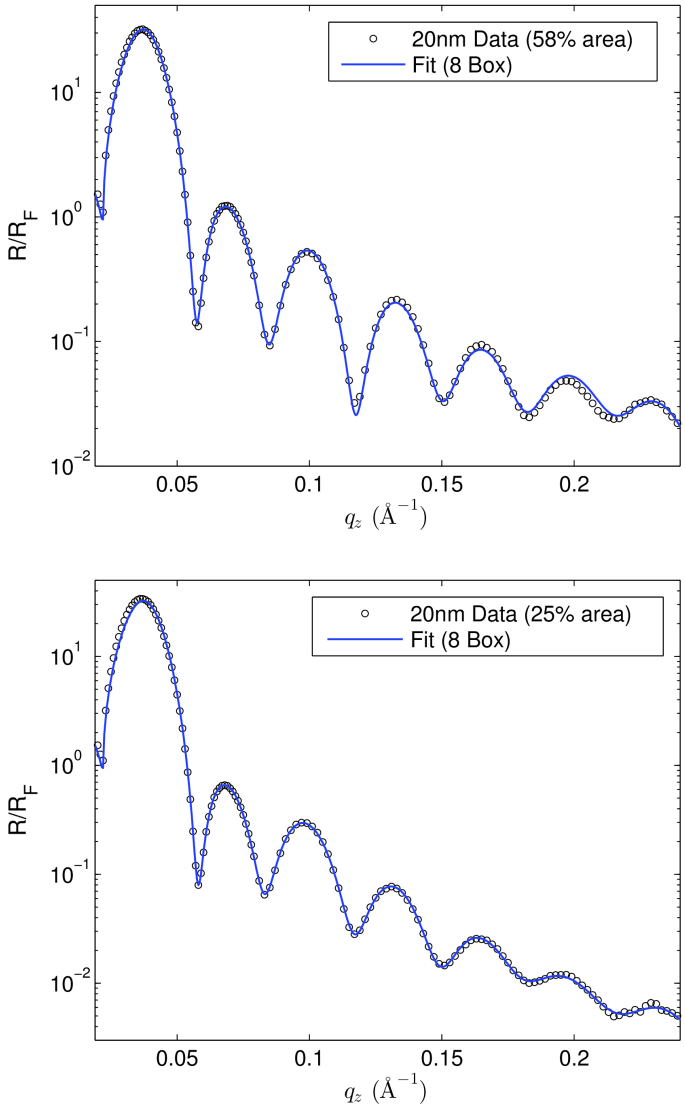

Figure 4.4: Results of the "8-box" model fit to the Fresnel reflectivity normalized data. Top: smallest amount of compression, bottom: greatest amount of compression. Black circles: data (error bars are smaller than the symbol). Blue line: fit.

The average electron density as a function of the height perpendicular to film plane corresponding to the two fits shown in Figure 4.4 can be seen in Figure 4.5. Two things are evident from this plot: 1.) the two data sets are in good agreement with one another and 2.) they demonstrate that the majority of the film

is well characterized as a monolayer of a thickness consistent with 20 nm particles (a box denoting a 20 nm layer can be seen in the figure as a guide for the eye). The consistency between these two suggests that despite great degree of compression between the two measurements the average density within the area illuminated by the beam is not changed. This may be consistent with the result found in Chapter 3 from the GID measurements, that the average interparticle spacing is mostly unchanged during compression, but it does not explain the multilayering observed in the microscopy results in the previous section.

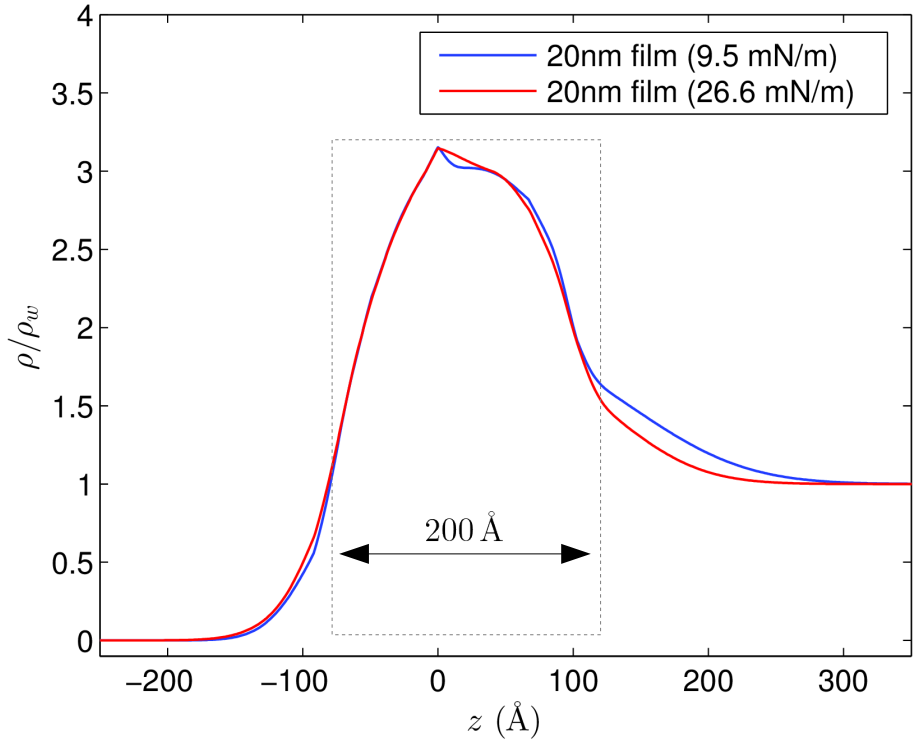

Figure 4.5: Electron densities for low and high compression of a 20 nm film (corresponding to fits in Figure 4.4). Both show very clear monolayers of approximately 20 nm (guide for the eye included).

The primary discrepancy between the two electron densities is in the shape of the profile just below the main film layer (the right hand side of Figure 4.5). The density smoothly drops off until only the subphase remains. This decay in intensity is suggestive of a small percentage of disordered particles passing into

the subphase, with the lower compression measurement showing more disorder - physically one might expect the opposite trend. The lack of difference in the main layer and the counter–intuitive nature of the disordered particles passing into the subphase suggests that these film conditions are not indicative of those for a continuously compressed film. Thus, the GIXOS measurements (which can be collected during continuous compression) are more likely to be illuminating.

4.2.2 Reflectivity Sample Damage

Much like in Chapter 3 the effects of beam damage on the film had to be taken into consideration. The exposure of the film to extended periods of high energy radiation can cause two possible types of damage: 1.) ionizing damage due to the high photon energy and 2.) thermal damage due to to total energy deposited. The likely effects of this damage are 1.) the removal of oleic acid from the particle by way of breaking its bond to the nanoparticle surface and 2.) the sintering of the nanoparticles that are in contact with one another. Both of these may disrupt the structure of the film and result in a change in the reflected intensity, therefore an upper limit on the total exposure had to be established to minimize the damage.

To determine this upper limit we measured the reflected intensity as a function of total exposure time at a fixed reflection angle corresponding to the largest reflection angle in the scan ($q_z = 0.261\,\text{Å}^{-1}$). This large angle maximizes the local intensity of the beam which results the pathological extreme of damage to the film. The beam attenuation filters which reduce the beam intensity by a factor of approximately 10^3 (used during data collection) were removed for the damage assessment measurement. Shown in Figure 4.6 is the reflectivity as a function of total exposure time. The reflected intensity varied by less than 20% within the first 400 seconds of exposure, after which point the intensity begins to climb dramatically. This point was set as the hard limit for maximum exposure of any reflectivity measurement.

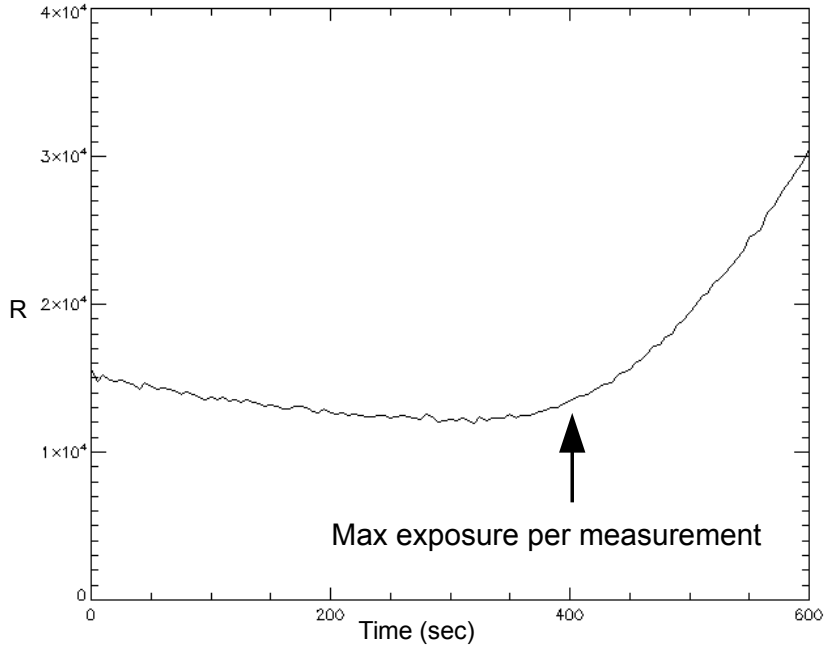

Figure 4.6: Reflectivity as a function of total exposure time. Collected at a fixed reflection angle ($q_z = 0.261\,\text{Å}^{-1}$) - the largest α for the reflectivity scans, at which the film would experience maximum intensity. Denoted is the maximum exposure time used.

4.3 Grazing Incidience X-Ray Off-Specular Scattering (GIXOS)

In order to capture the multilayering behavior of the films during a continuous compression the GIXOS technique was utilized. Unlike reflectivity GIXOS is performed with a fixed geometry and the entire data range can be collected in a single exposure without movement of the detector. The incident angle was fixed at $\alpha = 0.0904°$ with a beam size of $300\,\mu$m horizontal by $120\,\mu$m vertical. This resulted in a beam footprint of $0.3\,\text{mm} \times 76.4\,\text{mm} = 22.9\,\text{mm}^2$ which is approximately twice as large than the maximum footprint during the X-Ray Reflectivity measurements. Therefore it was expected that the GIXOS measurements would

provide better statistics about the film structure. The off-specular angle (θ) at which the detector was located was 0.15°. The exposure time for each scan was 30 seconds. And a scan was collected every 60 seconds during the compression.

The compression rate used to compress both 10 and 20 nm films during the GIXOS measurements was $2\,\mathrm{cm}^2/\mathrm{min}$. This was the same compression rate used for all the measurements. The films were compressed to approximately 25% their original area.

4.3.1 20 Nanometer Nanoparticle Film

The compression isotherm of the 20 nm particle film which was measured using GIXOS can be seen in Figure 4.7. It possesses the same features seen in the other previous isotherms (Figure 3.1): a low density phase with a slowly changing pressure per unit of compression followed by an abrupt increase in $\mathrm{d}P/\mathrm{dA}$ at around 60% of the original film area, marking the transition into the intermediate compression region. What's absent from this isotherm that's seen in Figure 3.1 is the transition to the "collapsed" phase around 30-40% the original area. It's likely this is due to the natural variability of the isotherms or the results of the different placement of the Wilhelmy plate within this particular trough - to make sufficient space for the scattering the Wilhelmy plate was placed near the end of the trough instead of in the middle (as was done for the isotherms in Figures 3.1 and 3.5). For this reason the compression ratio is considered a better measure of the state of the film than is the in–plane pressure value. None the less the pressure vs. area does provide us with supporting evidence of the film's state.

GIXOS data was collected every 30 seconds, but here I present a subset of those measurements which capture the essential behavior of the film during the compression. The measurements herein correspond to the red points in Figure 4.7: one at the start of compression, one at a latter point during the "gas-like" low density phase, and four measurements throughout the intermediate phase. The data corresponding to these points in the compression can be seen in the top panel of Figure 4.8. They are labeled by the percentage area compared to that for the uncompressed film.

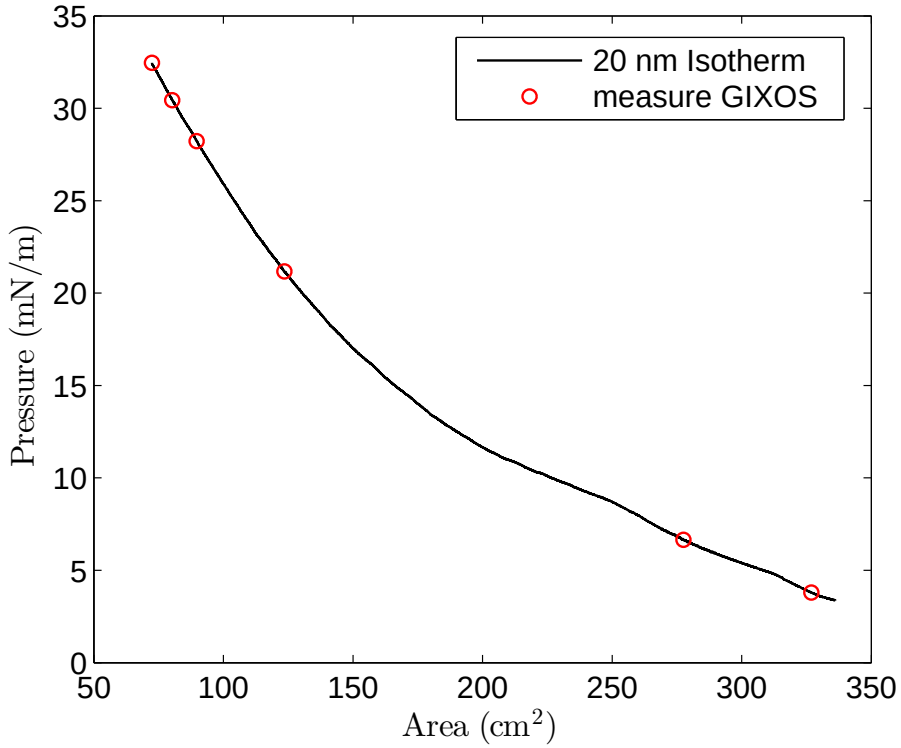

Figure 4.7: Isotherm of continuously compressed 20 nm nanoparticle film. Red points represent fitted GIXOS measurements seen in Figure 4.8.

The evolution of the electron density has some noteworthy features. Primarily the most prominant feature is the well defined monolayer whose thickness is consistent with 20 nm spherical particles. From this alone, one can say that the film is predominantly a monolayer. The top surface of the film has a well defined boundary, as evidenced by the abrupt drop in the density on the air-side (negative z-direction) of the film. The uncompressed film appears somewhat asymmetric with a broader shoulder at the film-water interface (positive z-direction).

Upon initial compression the peak density drops with an accompanying broadening of the density at the film-water interface. This occurs within the low density phase (note the first two points in Figure 4.7), suggesting that during the merging of the large film regions in the early stages of compression the edges of these regions may dislodge from the film and be forced through the water surface.

As the film is compressed into the intermediate phase (and particularly in

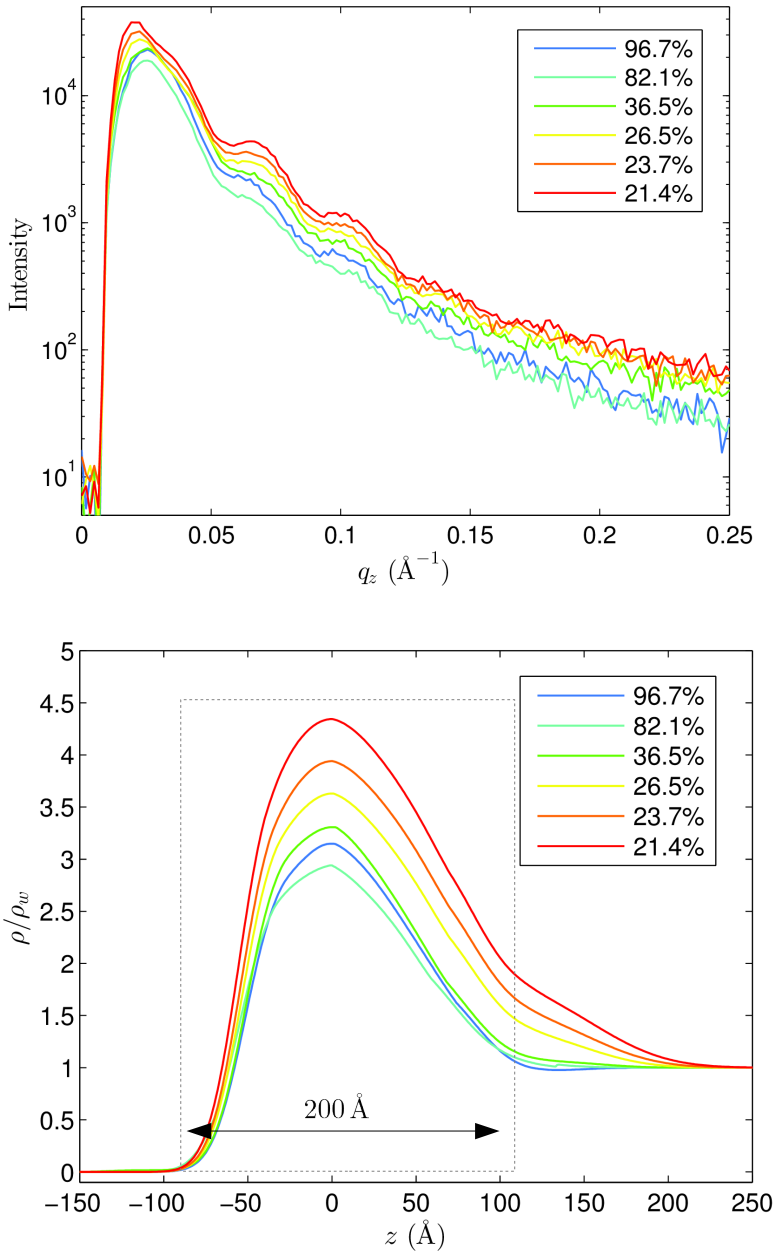

Figure 4.8: Evolution of GIXOS signal (top panel) and the corresponding electron densities vs. height along z-direction (bottom panel) during the compression of a 20 nm nanoparticle film. The scans correspond to the red points on the isotherm of Figure 4.7.

the late intermediate phase) the peak density changes rapidly. This change is non-linear - the rate of change of the density is greater the more the film is compressed. The broad shoulder at the nanoparticle-water interface increases in intensity and passes further into the subphase. Conversely, the film-air interface shows little change during this same period of compression.

The broad shoulder that developed at the film-water interface is not consistent with the formation of a discrete second film layer: 1.) it is not sufficiently thick (only about 5-10 nm) and 2.) is does not demonstrate a peak in density which would connote an additional discrete layer as seen in other nanoparticle films undergoing multilayering. [9, 58, 77] However, this is consistent with the buckling of a seemingly continuum material whose buckled structures subtend into the subphase. [67] This is evidence that the multilayering structures seen in Figure 4.1 are likely buckling that passes below the water surface, not up toward the air above the film.

4.3.2 10 Nanometer Nanoparticle Film

A comparable process was carried out on the 10 nm nanoparticle film. The GIXOS configuaration, including the incident angle, off-specular angle, sample–to–detector distance, beam size, and exposure time, was the same for the 10 nm film measurements as it was for the 20 nm film measurements.

The isotherm corresponding to the continuous compression of the 10 nm film can be seen in Figure 4.9, which has been compressed at a rate of $2\,\mathrm{cm}^2/\mathrm{min}$. It has the same qualitative features as the 20 nm isotherm in Figure 4.7. They both reach approximately the same peak pressure with the same degree of compression. The plot shows the selected GIXOS scans which can be seen plotted in the top frame of Figure 4.10. The bottom frame shows the calculated electron densities from the fits of the corresponding GIXOS data.

The behavior of the 10 nm film upon compression bears a great deal of resemblance to that of the 20 nm film, but with some striking differences as well. The film starts with a single prominent film layer which is consistent with the anticipated thickness of 10 nm. As the film is compressed the density of this layer

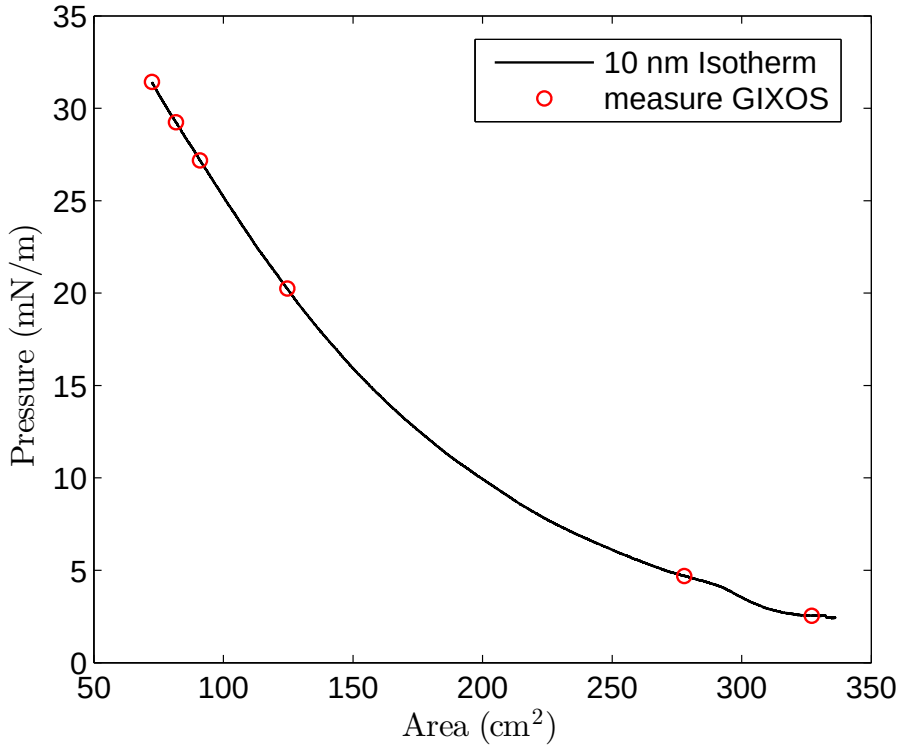

Figure 4.9: Isotherm of continuously compressed 10 nm nanoparticle film, at a rate of 2 cm^2/min. Red points represent fitted GIXOS measurements seen in Figure 4.10.

initially decreases slightly (compare the 96.7% area scan to that at 82.2% area) and has an accompanying increase in the breadth of its interfacial shoulder. As the film is further compressed the density of this layer grows non-linearly. Unlike the 20 nm film the film broadening occurs at the film–air interface and it is thick enough to constitute an additional 10 nm layer. By the point the film is compressed to approximately 30% of its original area the broadening has clearly developed into a discrete layer. Thus, unlike the 20 nm film, the multilayering of the 10 nm film consists of a discrete second nanoparticle layer over some fraction of the film. However the film is not observed to form a trilayer. Therefore the multilayering structures seen in the microscopy image (Figure 4.2) must be the result of the monolayer rupturing and sliding over onto itself, forming a bilayer. Lastly, the film–air interface maintains its integrity throughout the compression.

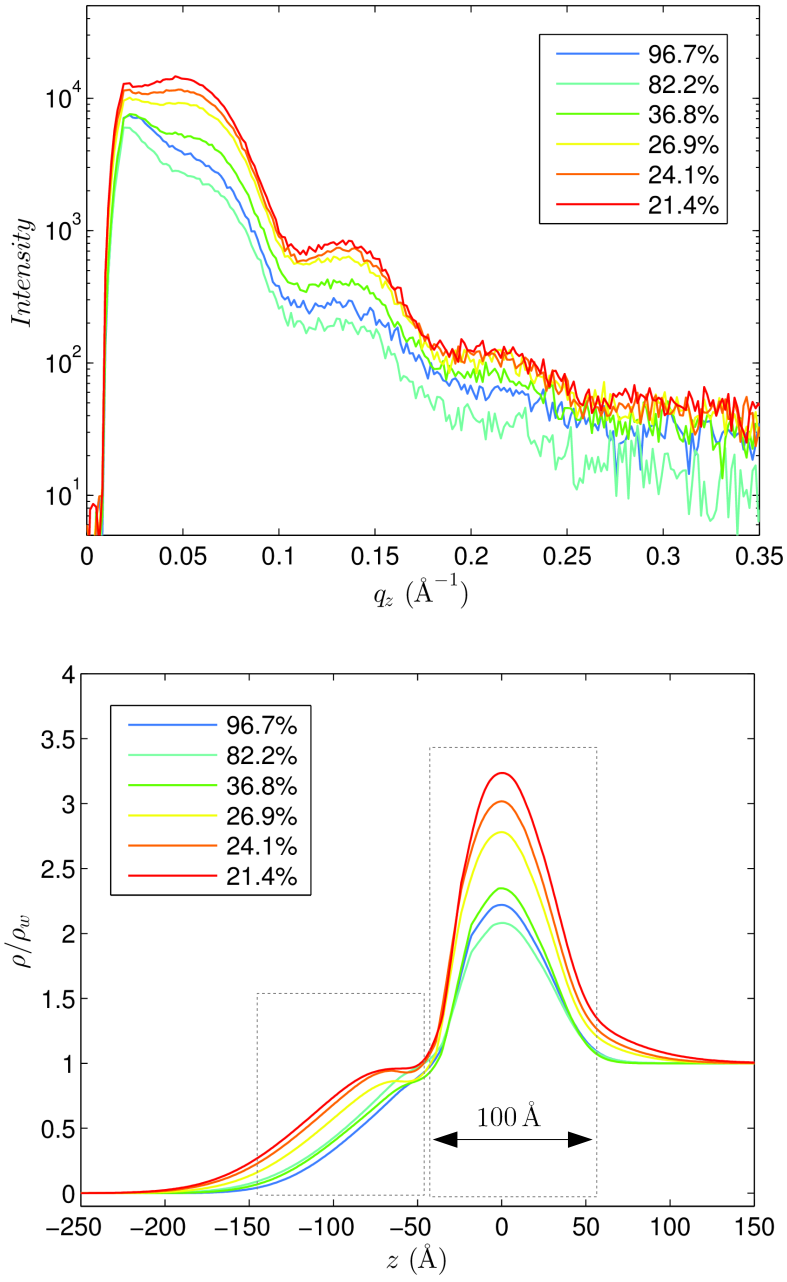

Figure 4.10: Evolution of GIXOS signal (top panel) and the corresponding electron densities vs. height along z-direction (bottom panel) during the compression of a 10 nm nanoparticle film. The scans correspond to the red points on the isotherm of Figure 4.9.

To summarize, the compression of the 20 nm nanoparticle film resulted in continuum buckling which was pushed down into the subphase. Conversely the 10 nm particle film formed a distinct bilayer over some fraction of it's surface, but did not form any buckling which passed into the subphase. It can be concluded that the multilayering behavior of iron oxide nanoparticle films show a clear size dependence.

4.4 SEM

For some additional corroboration of these results (at least in the context of the 20 nm film), a compressed 20 nm film was stamped using the Langmuir-Schaefer technique described in Chapter 2 which was then measured using SEM in order to observe the multilayering structures with higher resolution. Once concern was that the out–of–plane structure would be more likely to be disrupted by the stamping than would a uniform monolayer, therefore it's not clear that this measurement is as reliable as the in-situ measurements done with GIXOS. Keeping this in mind, it still provided another avenue for observing the out–of–plane behavior. In Figure 4.11 is a successively magnified region of the compressed film. The sinuous structures seen in microscopy are clearly visible and upon inspection they appear to be in the foreground of the image - i.e. raised up off the plane of the substrate. Given that the substrate was adhered to the film-air interface then these buckling structures must have formed into the subphase thus corroborating the observations made for the 20 nm film using GIXOS and XR.

The text of Chapter 4, in part, is a reprint of material as it appears in: J. Stanley, L. Boucheron, Y. Dai, S. You, B. Lin, M. Meron, O. Shpyrko "Evolution of in–plane and out–of–plane structure of nanoparticle Langmuir monolayers under lateral compression", (in preparation), 2015.

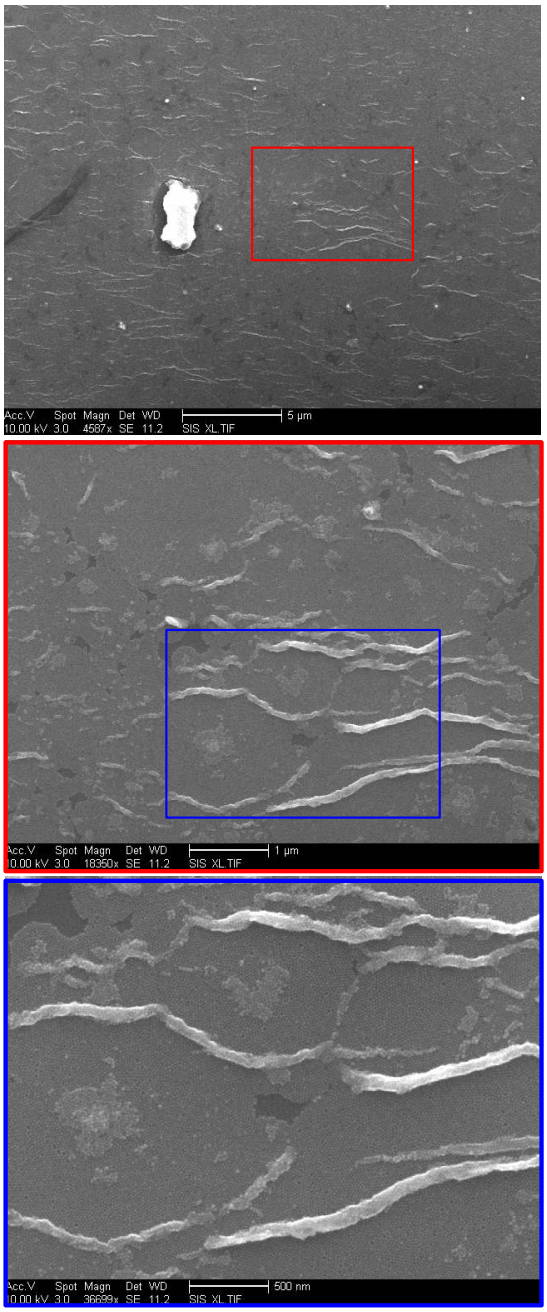

Figure 4.11: SEM of compressed 20 nm nanoparticle film having been transferred to a silicon substrate with the Langmuir-Schaefer transfer method. Figure shows successive magnification of film, highlighting the buckling structures.

Chapter 5

Phase Separation of Bi-Dispersed Films

The following is in a reproduction of my paper submitted to *Applied Physics Letters*, titled "Spontaneous Phase Separation During Self-Assembly in Bi-Dispersed Metallic Nanoparticle Monolayers."

5.1 Abstract

Recent developments in the synthesis of iron oxide nanoparticles have resulted in the ability to fabricate roughly spherical particles with extremely high size uniformity (low poly–dispersity). These particles can form self-assembled monolayer films at an air-water interface. When the poly–dispersity of the particles is low these monolayers can be well–ordered over a length scale dozens of times the particle size. The van der Waals forces between the particles is what drives this self–assembly. Through the use of Grazing Incidence X-Ray Diffraction we demonstrate that when these films are formed at the liquid surface from bi–dispersed solutions containing 10 and 20 nm particles suspended in chloroform, the particles phase separate into well–ordered patches during the self–assembly process. Furthermore, the domain sizes of these phase separated regions are at most 2-3 times smaller than that of a film comprising only mono–dispersed particles and their degree of disorder is comparable. This is shown for multiple solutions with differing ratios

of 10 and 20 nm particles.

5.2 Introduction

Due to their small size, the interactions between metallic nanoparticles are dominated by van der Waals forces. These van der Waals forces drive self-assembly which, along with the particles' shape and composition, determines the resulting organization. The organization can form one, two or three dimensional structures. [9,10,35,37,49–51,76,79] One such manner of assembly is the formation of highly uniform monolayers at the air-water interface. To do so, the monolayer constituents are first suspended in an organic solvent which is then deposited onto the water surface. The particles then organize into patches of monolayer film. This has been done with a wide array of different particles such as polystyrene beads, phospholipids, polymers, and nanotubules among others. [9, 33, 52, 78, 80–84]

In the case of metallic nanoparticles like gold, silver, or iron oxide, they must be capped with a hydrophobic ligand to prevent them from aggregating and from passing below the water's surface. [43,58] With improvements in nanoparticle synthesis the ability to make highly mono–dispersed nanoparticles has allowed for these sorts of films to be created with a great degree of uniformity. [44, 59] This tunable synthesis opens the possibility of controllably studying how different sized particles interact - an approach not previously explored.

Herein we demonstrate that in addition to forming a well ordered monolayer film, self-assembly has the ability to phase separate iron oxide nanoparticles of differing sizes. Specifically, when approximately spherical iron oxide nanoparticles of two sizes (10 and 20 nm) are randomly mixed into the initial sample solution, they will separate into distinct 10 and 20 nm domains once deposited onto the liquid substrate. Varying the relative concentration of 10 and 20 nm particles allows us to explore how this phase separation is affected by differing relative surface area coverage.

5.3 Data Collection

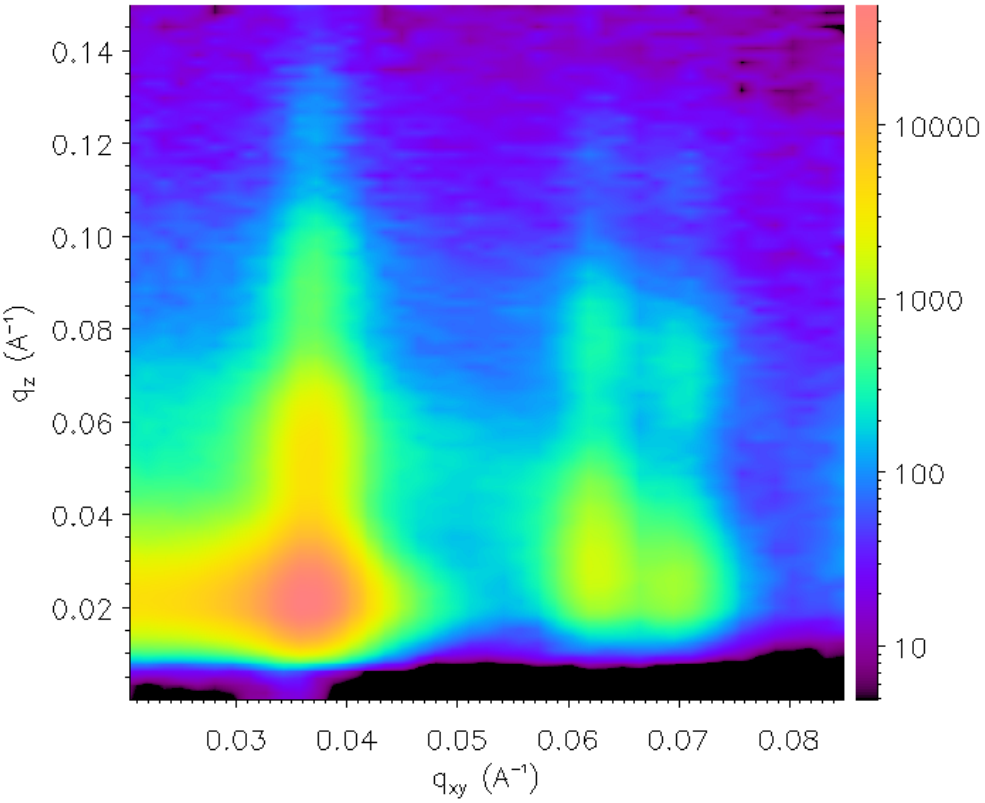

Figure 5.1: Two-dimensional GID data for the mono–dispersed 20 nm particle film showing first through third order Bragg rods - the locations of these along the q_{xy} direction correspond to Bragg plane spacings within the film (q_z and q_{xy} in units of Å^{-1}).

The nanoparticles were purchased from Ocean Nano Tech. The 10 and 20 nm iron oxide nanoparticles were coated in a surface ligand of oleic acid. Both particles had a size distribution that was less than 5% of their manufactured diameter. The particles were initially in powder form and were then each suspended in chloroform at a concentration of $0.50 \pm 0.02\,\text{mg/mL}$ - these two solutions are referred to as the 10 and 20 nm stock solutions. From these two stock solutions the following mixtures were made (labeled as 10nm:20nm solutions by volume): 1:8, 1:2, and 4:1. The first mixture corresponded to equal number of 10 and 20 nm particles per unit volume, given a factor of 2 difference in their diameter. The

second mixture corresponded approximately to equal total surface area coverage of 10 and 20 nm particles, per unit volume. Finally, the third mixture was predominantly 10 nm particles (in both number and surface area coverage) per unit volume.

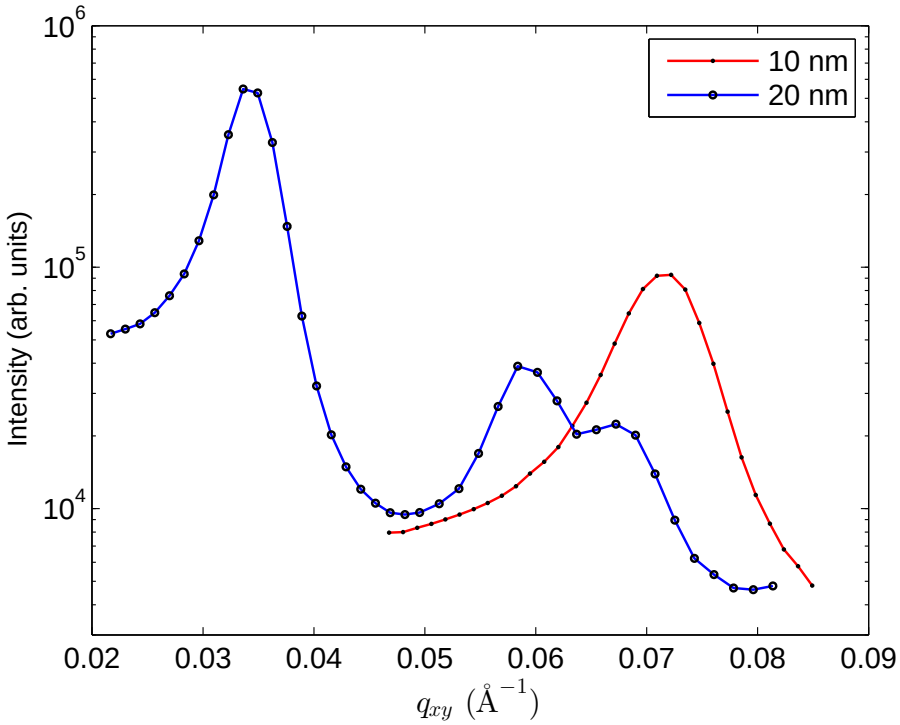

Figure 5.2: GID peak intensity vs q_{xy} for both 10 nm (red) and 20 nm (blue) mono-dispersed films.

The films were formed using the in–house Langmuir-Blodgett trough at Sector 15 ID-C at the Advanced Photon Source (Argonne National Labs), which had a total surface area of $338.2 \pm 0.2\,\mathrm{cm}^2$. The trough was filled with purified water (from a Milli-Q purification system) such that the water surface formed a convex meniscus. In total, five different of films were made: two mono–dispersed films from the 10 and 20 nm stock solutions and three bi-dispersed films from the three mixtures. Using a syringe, the drop-casting deposition method was carried out in order to disperse the nanoparticles onto the water surface as the chloroform evaporated. [18] For each film, the solution was deposited until the point at which the drops no longer spread unimpeded by the particles already on the liquid surface.

This volume varied for the different solutions, despite all the solutions having the same particle mass density. This was due to the difference in surface area coverage per unit of solution volume for the different particle ratios. For the mono–dispersed 10 nm solution this volume corresponded to 1150 μL and for the mono-dispersed 20 nm solution, 2455 μL. For the mixed solutions the deposited volumes were between these two values ($1:8 \rightarrow 2440\,\mu$L, $1:2 \rightarrow 1800\,\mu$L, $4:1 \rightarrow 1300\,\mu$L). Once deposited the films were allowed to come to equilibrium for approximately 30 minutes, so that the chloroform could fully evaporate and the particles could redistribute. At this point the films were ready to be measured. Multiple measurements were taken across each film to verify uniformity.

The GID measurements were taken using a monochromatic beam of wavelength $\lambda = 1.239$ Å. The incident beam size was 20 μm horizontal by 120 μm vertical. The beam was at an incident angle of $\alpha = 0.0906°$, which resulted in an illuminated film area of 20 μm $\times$ 7.6 cm along the beam direction. The scattered signal was measured using a 2D X-Ray detector (PILATUS 100k) at a distance 550.0 mm downstream from the sample. The resulting measurement of the scattered field can be seen in Figure 5.1 (showing the scattering from the mono–dispersed 20 nm film), where the horizontal direction (q_{xy}) corresponds to the in–plane portion of the elastic scattering vector and the vertical direction (q_z) corresponds to the out–of–plane component. The q_z direction contains no structure factor information since the films were monolayers. All fluctuations along q_z are due to the average particle form factor. The intensity variation along the q_{xy} direction contains the information about the in-plane structure. [19,20] Therefore, the 2D data (as seen in Figure 5.1) was integrated along the q_z direction. The resulting Bragg peak profile can be seen in Figure 5.2 for both mono–dispersed films (10 and 20 nm). Data was collected for the first through third order GID peaks for the 20 nm film and only the first order peak of the 10 nm film. The latter was located at approximately twice the q_{xy} value as the 20 nm first order peak, as a result of the particles being approximately half the diameter.

Due to the small scattering angle the detector was masked with slits oriented along q_z. This shielded the detector from the high intensity low-q scatter. The

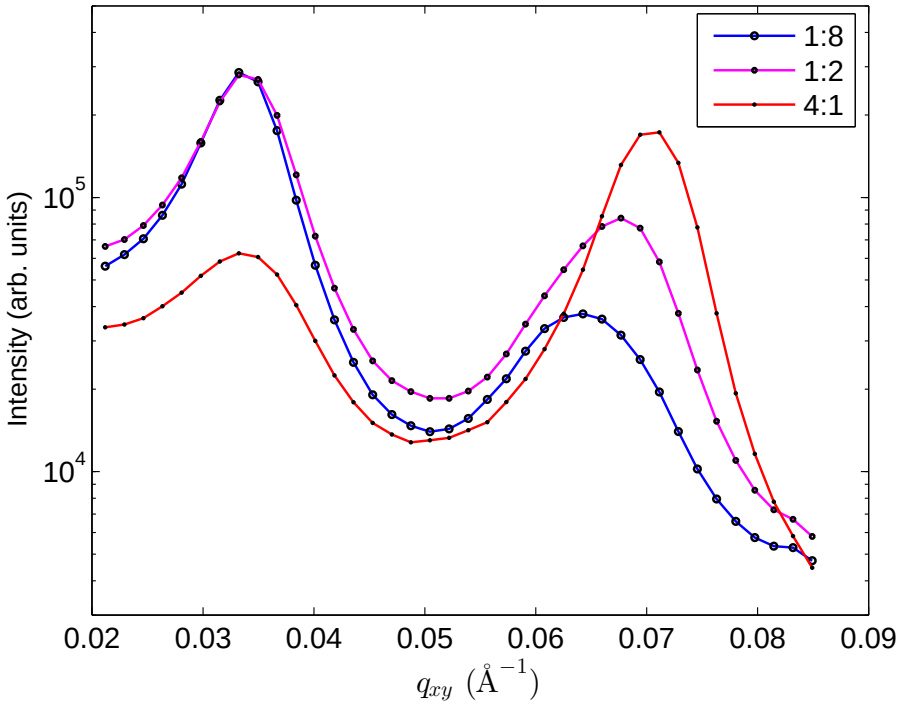

Figure 5.3: GID peak intensity vs q_{xy} for the three mixtures of 10 to 20 nm particles - 1:8 (blue), 1:2 (magenta), and 4:1 (red).

detector and slits were then stepped along q_{xy} and the results were joined to form the 2D image seen in Figure 5.1. These slits defined the q_{xy} resolution, which was $\Delta q_{xy} = 0.0031\,\text{Å}^{-1}$. In the same manner, Bragg peak data was collected for the three mixed solution films, the results of which can be seen in Figure 5.3. Note that the peaks corresponding to the hexagonal close packed (HCP) structure of 20 nm particles as well as that for 10 nm are visible, but with differing relative peak amplitudes as compared to the mono–dispersed films. The presence of both peaks suggests some degree of phase separation of the two particle sizes.

The diffraction data from the five films (2 mono–dispersed and 3 bi–dispersed mixtures) were then analyzed to extract quantitative information about the in–plane structure. From the peak location and width we could determine the inter–particle spacing and the correlation length of the ordered film regions. In this way the structures of the bi–dispersed films were compared to the mono–dispersed references.

5.4 Peak Fitting and Scherrer Equation

The peak fits were performed on the log of the intensity data - this greatly improved the fits' convergence. For the mono–dispersed films a Gaussian was fit to each of the GID peaks and a quadratic spline was fit to the background. For the bi-dispersed films, the third order peak from the 20 nm signal and the first order peak from the 10 nm signal were almost centered on one another (approximately 0.068 and 0.071 Å^{-1}, respectively). As a result, these two contributions were approximated by a single Gaussian. The 20 nm contribution to this peak could be determined by assuming a consistent relative amplitude between the first, second, and third order peaks. The first and second order 20 nm peaks (located at approximately 0.034 and 0.059 Å^{-1}, respectively) were fit by single Gaussian functions. In this way the model was kept to fewer fit parameters to avoid overfitting.

Fits using Lorentizan and Voigt functions for peak shape were also performed [85], but neither showed good convergence when fit to the data or the log of the data. Table 5.4 shows the results of the Gaussian peak fitting to the log of the intensity data for the five films. From the peak widths the correlation lengths (L) of the ordered regions were calculated. This was done using the Scherrer equation (equation 5.1), where $\lambda = 1.239\,\text{Å}$ (X-Ray wavelength), K is a unitless shape factor close to unity, β is the full width at half max (FWHM) of the Bragg peak (in radians) which was calculated from the Gaussian fit's σ value, and θ is the Bragg angle. The result, L, is the average linear dimension of an ordered film region. [75]

$$L = \frac{\mathrm{K}\lambda}{\beta \cos\theta} \tag{5.1}$$

From the fitting results for the mono-dispersed films the average interparticle spacing, calculated from the first GID peak location, was $10.12 \pm 0.04\,\text{nm}$ and $21.03 \pm 0.17\,\text{nm}$ (for 10 and 20 nm films); the peak locations were consistent with a HCP structure, similar to that seen in other work. [36, 55] In order to calculate the grain size using the Scherrer equation we first had to determine the FWHM.

In order to calculate the FWHM, the broadening due to instrumental resolution first needed to be accounted for, as shown in equation 5.2

Table 5.1: Results of peak fitting to mono-dispersed 10 and 20 nm films as well as bi-dispersed films. q_0 and σ are the peak centroid and standard deviation. L is the average correlation length, calculated from Scherrer equation for each peak width.

film	q_0 (Å^{-1})	σ (Å^{-1})	L (nm)
20 nm	0.0345 ± 0.0001	0.0034 ± 0.0001	545 ± 67
	0.0592 ± 0.0002	0.0039 ± 0.0002	324 ± 44
	0.0685 ± 0.0002	0.0035 ± 0.0002	430 ± 105
10 nm	0.0717 ± 0.0001	0.0051 ± 0.0001	209 ± 6
1:8	0.0341 ± 0.0001	0.0047 ± 0.0001	225 ± 8
	0.0607 ± 0.0014	0.0045 ± 0.0005	192 ± 41
	0.0682 ± 0.0014	0.0050 ± 0.0005	175 ± 36
1:2	0.0343 ± 0.0001	0.0049 ± 0.0001	204 ± 7
	0.0599 ± 0.0001	0.0040 ± 0.0004	246 ± 66
	0.0686 ± 0.0004	0.0053 ± 0.0002	182 ± 10
4:1	0.0344 ± 0.0001	0.0053 ± 0.0002	153 ± 9
	0.0608 ± 0.0018	0.0057 ± 0.0011	130 ± 35
	0.0711 ± 0.0004	0.0054 ± 0.0002	210 ± 12

$$\sigma^2_{grain} = \sigma^2_{peak} - \sigma^2_{instrumental} \tag{5.2}$$

where σ_{grain} is the peak broadening due to finite grain size and $\sigma_{instrumental}$ is the instrumental broadening (given by the slit resolution Δq_{xy} defined above). [20] From σ_{grain} the FWHM, and subsequently L, was calculated. This was done for each peak.

The same procedure was carried out for the bi-dispersed films. In this case the third peak was a mixed contribution from the first order 10 nm GID peak and the third order 20 nm peak. The ratio of amplitudes for the first, second, and third order GID peaks from the mono-dispersed 20 nm film were approximately $3.2 : 2.1 : 1.7$ (respectively), as determined from the amplitude fit parameters. From this we could estimate how much of the amplitude of the overlapped peak was contributed by the 20 nm signal, assuming the intensities added linearly. The resulting correlation lengths for the mono– and bi–dispersed films can be seen in Table 5.4.

The Scherrer equation is intended to be used in analyzing grain size of

crystallites comprising atomic scale lattices but not necessarily lattice–like organization of loosely–bonded nanostructures such as we have here. [20] Despite this, the Scherrer equation provides us with a way to consistently compare correlation lengths between different films, using the diffraction peak widths. Given that the diffraction is not from atomic lattice planes we did not attempt to take into account peak broadening due to strain (which would contribute an additional term to equation 5.2), given that we had no practical way to approximate the strain that may have been present in the films. Thus, the correlation lengths in Table 5.4 are likely underestimates.

As shown in Table 5.4, the average correlation length for the ordered film regions for a given particle decreased as the relative concentration of that particle decreased. The film with the smallest concentration of 10 nm particles (the 1:8 mixture - $\sim 20\%$ of the film area) had a correlation length $\sim 84\%$ of that of the mono–dispersed 10 nm film. The film with the smallest concentration of 20 nm particles (the 4:1 mixture - $\sim 10\%$ of the film area) had a correlation length $\sim 33\%$ of that of the mono–dispersed 20 nm film.

5.5 Ordered Fraction

In addition to the average correlation length, we calculated the fraction of particles contributing to the ordered regions of the bi–dispersed films relative to that of the mono–dispersed films. In order to do this, we made use of the fact that the integrated intensity of the Bragg peak would be proportional to the ordered scattering volume. [20, 21] If we then divided this result by the total deposited volume of particles that make up the film, the result would be proportional to the fraction of particles within the film that are in an ordered configuration. This is expressed in equation 5.3 where I_{Bragg} is the 10 or 20 nm Bragg peak intensity vs. q_{xy} (absent the diffuse background); $V_{ordered}$ is the volume of 10 or 20 nm particles that are in an ordered configuration; and V_{total} is the total volume of 10 or 20 nm solution deposited.

$$\frac{1}{V_{total}} \int I_{Bragg}\, \mathrm{d}q \propto \frac{V_{ordered}}{V_{total}} \tag{5.3}$$

Since many other instrumental factors contribute to the intensity integral, equation 5.3 is only illuminating when used to compare the results of a mixed film to that of a mono–dispersed film, both having been measured with the same instrumental conditions. This is done by taking the ratio of the results of equation 5.3 for two different films, thereby canceling the instrumental factors. In this way we compared the bi–dispersed films to the 20 nm mono–dispersed film.

Equation 5.3 was calculated for the first order 20 nm GID peak from the mono–dispersed 20 nm film data and the three mixed films. The resulting values for the mixed films were then divided by that obtained from the 20 nm mono–dispersed film, in order to compare the fraction of ordered particles in the bi–dispersed relative to the mono–dispersed film.

The result for each mixed film is as follows: 0.50 ± 0.06 for the 1:8 mixture, 0.91 ± 0.10 for the 1:2 mixture, and 0.94 ± 0.11 for the 4:1 mixture. Thus the fraction of ordered particles is comparable between the bi– and mono–dispersed films. We did not carry out this procedure for the 10 nm GID peak since the peak overlap with the 20 nm signal resulted in much greater uncertainty in the peak integration.

5.6 Discussion

In conclusion, despite being formed from randomly a mixed solution, bi–dispersed iron oxide nanoparticle films demonstrate a surprising amount of order once self-assembled. This solution of 10 and 20 nm particles is phase separated into patches of the two species. This phase separation must occur spontaneously during the abrupt spreading of the solution onto the liquid surface, but it is unclear if this is solely due to the inter–particle van der Waals forces. In the case of a bi–dispersed film whose surface area comprises 50% each of 10 and 20 nm particles, the ordered regions formed are only approximately $20 - 50\%$ smaller in diameter than their respective mono–dispersed counterparts.

Furthermore, one might expect that even though the bi-dispersed films form ordered regions, these should represent a smaller fraction of the total particles due to the disorder caused by mixing with another size. But in fact the fraction of particles that form well ordered phase separated regions is comparable to that in the mono-dispersed films. These results demonstrate self-assembly may not be solely a local mechansim. With further study this non-local effect may find application in biomolecule manipulation, nanoscale fabrication for things like thin film coatings, and patterning of nanostructures, along with likely many other aspects of nanotechnology.

5.7 Supplemental

The content of this chapter up to this point has been a reproduction of my paper submitted for publication to *Applied Physics Letters*. The remainder of this chapter appended to expand upon the preceding analysis in order to address some details that the brevity of the the journal of submission would not permit.

5.7.1 2D Data - Mixed Films

Figure 5.4 is a characteristic example of the GID data of the 1st diffraction peak from a 10 nm nanoparticle film. This along with Figure 5.1 represent signature data for the mono–dispersed films of the two particle types. The well defined form factor nodes seen in both figures are suggestive of the low poly–dispersity of the two samples. These two measurements act as the controls to which I compared the mixed samples, both for peak locations and peak widths. The 2D GID for the mixed films is seen in Figure 5.5. The evolution from predominantly 20 nm to predominantly 10 nm is clearly visible.

The 1D data corresponding to the bi–dispersed films, seen in Figure 5.3, was generated by integrating the 2D GID data over q_z in the same manner as that in Figure 5.1 was integrated in order to produce the 20 nm plot in Figure 5.2.

Given the well defined Bragg rods, which demonstrate a high degree of symmetry about q_z and well defined form factor nodes, the mixed films must have

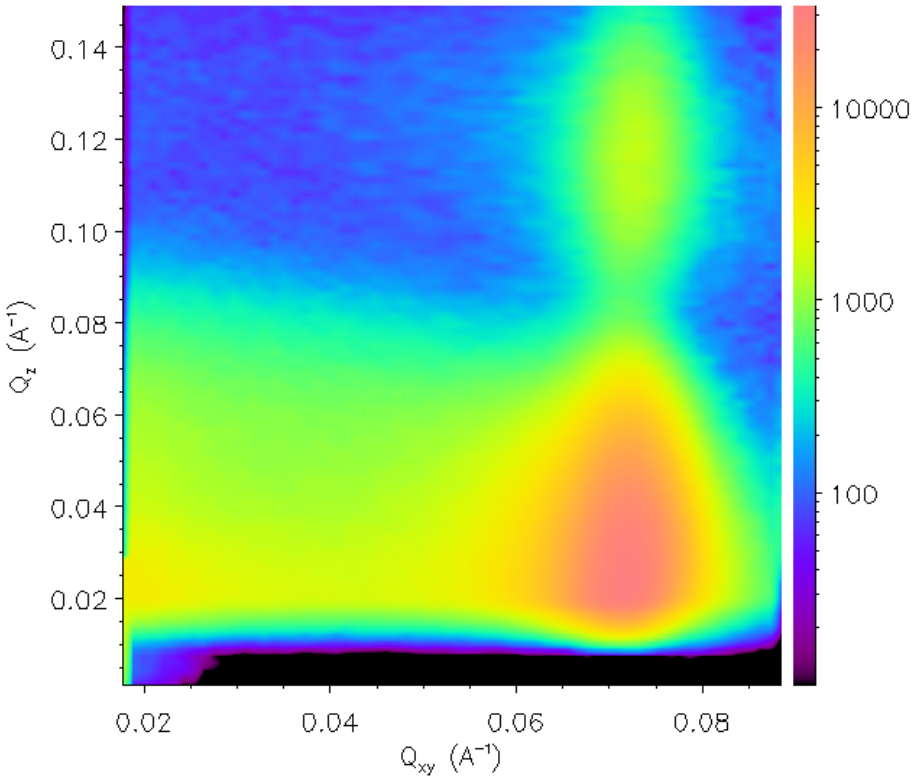

Figure 5.4: 2D GID data of a 10 nm mono-dispersed monolayer film showing the 1st order GID Bragg rod. The form factor node along the q_z direction is clearly defined.

a well defined interparticle spacing and therefore have a low degree of disorder - an assessment made based solely on the form of the 2D data. Similar measurements have been made on both gold and silver nanoparticle monolayers which should contrasting results - the silver nanoparticle data demonstrates one broad and asymmetric peak, indicative of a liquid like organization. On the other, hand the gold data demonstrates similar characteristics to that which we show here. [77]

5.7.2 Uncompressed vs. Compressed

In the proceeding sections of this chapter the analysis was done on uncompressed mixed films. All observed structure was the result of self-assembly. However the bi–dispersed films corresponding to the data in Figure 5.5 were compressed

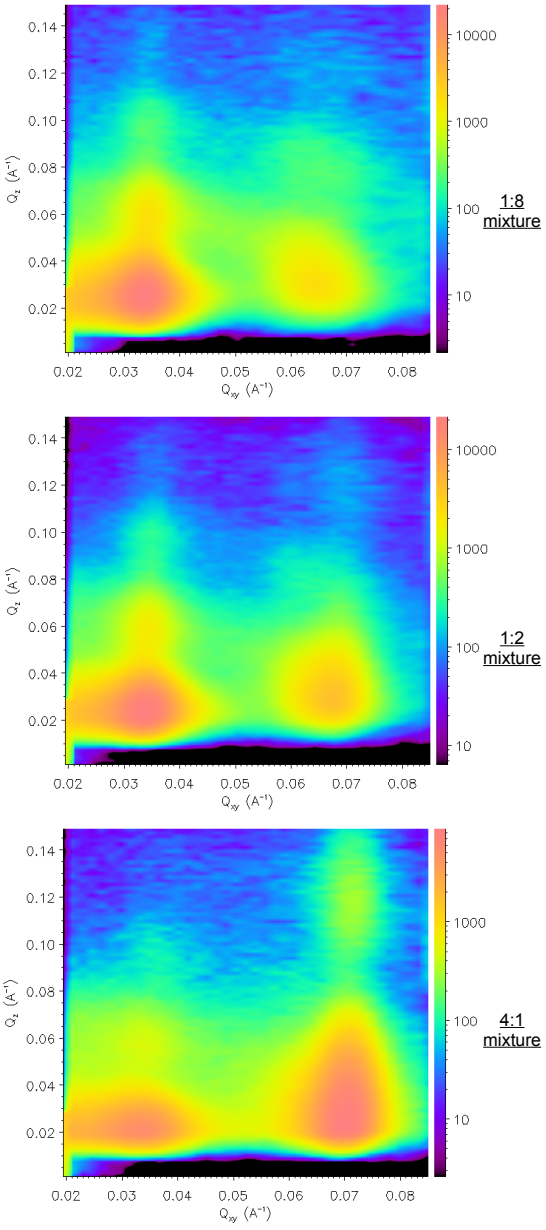

Figure 5.5: 2D GID data from the bi–dispersed films. Top: 1:8 mixture (10:20nm particles by mass), middle: 1:2 mixture, and bottom: 4:1 mixture. The form factor (along the q_z) is visible in the overlapped peak, most prominently in 1:2 mixture.

and subsequent GID data was taken. The films were compressed to approximately 24% of their original surface area ($338\,\mathrm{cm}^2 \rightarrow 81\,\mathrm{cm}^2$), which corresponded to a

pressure of 34.8 mN/m for the 1:8 mixed film , 36.6 mN/m for the 1:2 mixed film, and 32.1 mN/m for the 4:1 mixed film. The GID data pre– and post–compression can be seen in Figure 5.6.

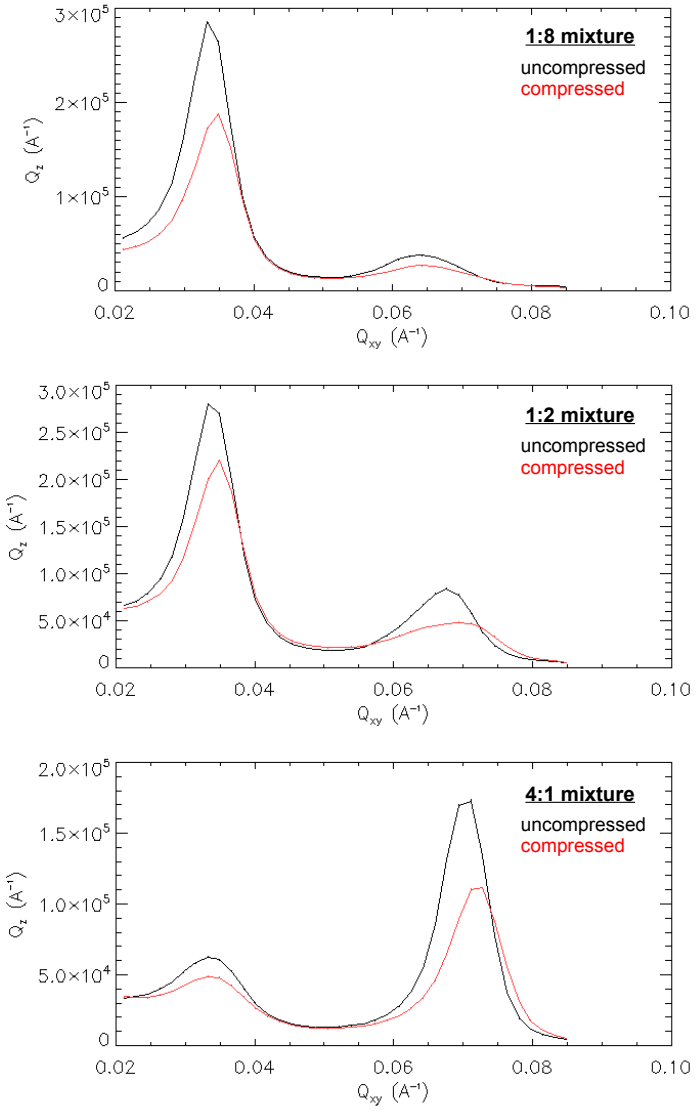

Figure 5.6: Comparison of bi–dispersed films in their compressed and uncompressed state.

There are a few noteworthy aspects about the resulting compression: 1.) The size of the ordered regions of 10 and 20 nm particles are greatly reduced as

evidenced by the marked decrease in peak intensity seen for all three mixtures in Figure 5.6. As a comparison, the compression of the mono–dispersed films resulted in little to no disruption of the ordered monolayer regions, as was previously discussed in chapter 2. This lose of order may be the result of the smaller 10 nm particles slipping between or under the 20 nm regions and ultimately causing dislocation defects in the 20 nm regions. 2.) Both 10 and 20 nm peak locations shift toward a larger q_{xy} value when compressed. This corresponds to a smaller average interparticle spacing.

5.7.3 Peak Fitting

The peak fitting for the five films was performed on the log of the intensity data. Voigt and Lorentzian fits were attempted on the raw data, but the convergence was poor compared to that of the fit to the log of the data. [85, 86] Additionally, the quadratic model for the background conformed better to the shape of the monotonic background once the log of the data had been taken. The results of the fit to the 10 and 20 nm mono–dispersed films can be seen in Figure 5.7 and the results of the bi–dispersed films can be seen in Figure 5.8. The blue dashed line is the quadratic background fitting, the green line is the complete fit (background+3 Gaussian peaks), and the red line is the integrated data.

Since the Guassian model was fit to the log of the intensity data the FWHM of the raw data did was not directly related to the fit parameter σ in the typical fashion, $FWHM = 2\sqrt{2\ln 2}\sigma$, given that the peak fit was not a simple Gaussian. By fitting log(I) with a Gaussian, the model is then given by:

$$I(q) = e^{(A\, e^{-(\Delta q^2/2\sigma^2)})} \tag{5.4}$$

The minimum value of this peak shape is $I_{min} = I(\pm\infty) = 1$ and the maximum value is given by $I_{max} = I(0) = e^A$. Thus the FWHM will be the peak width at the half-way point between the maximum and minimum. Therefore,

$$I(q_h) = \frac{e^A + 1}{2} = \exp(A\, e^{-(\Delta q_h^2/2\sigma^2)}) \tag{5.5}$$

must be solved for Δq_h, such that $2\Delta q_h = \text{FWHM}$. The result is

$$\text{FWHM} = 2(\Delta q_h) = 2\sigma \sqrt{2 \ln \left(\frac{A}{\ln \left(\frac{e^A + 1}{2} \right)} \right)} \tag{5.6}$$

where A and σ are the peak fitting parameters. Unlike a typically Gaussian fit the FWHM, in this case, depends on both the amplitude and σ of the peak. Equation 5.6 was used in calculating the results of Section 5.4 from the fit parameters in Table 5.4. The FWHM was then used to calculate the grain size using the Scherrer equation, the results of which can be found in the same table.

The text of Chapter 5, in part, is a reprint of material as it appears in: J. Stanley, L. Boucheron, B. Lin, M. Meron, O. Shpyrko , "Spontaneous phase separation during self-assembly in bi-dispersed metallic nanoparticle monolayers", *Applied Physics Letters*, (submitted for publication), 2014.

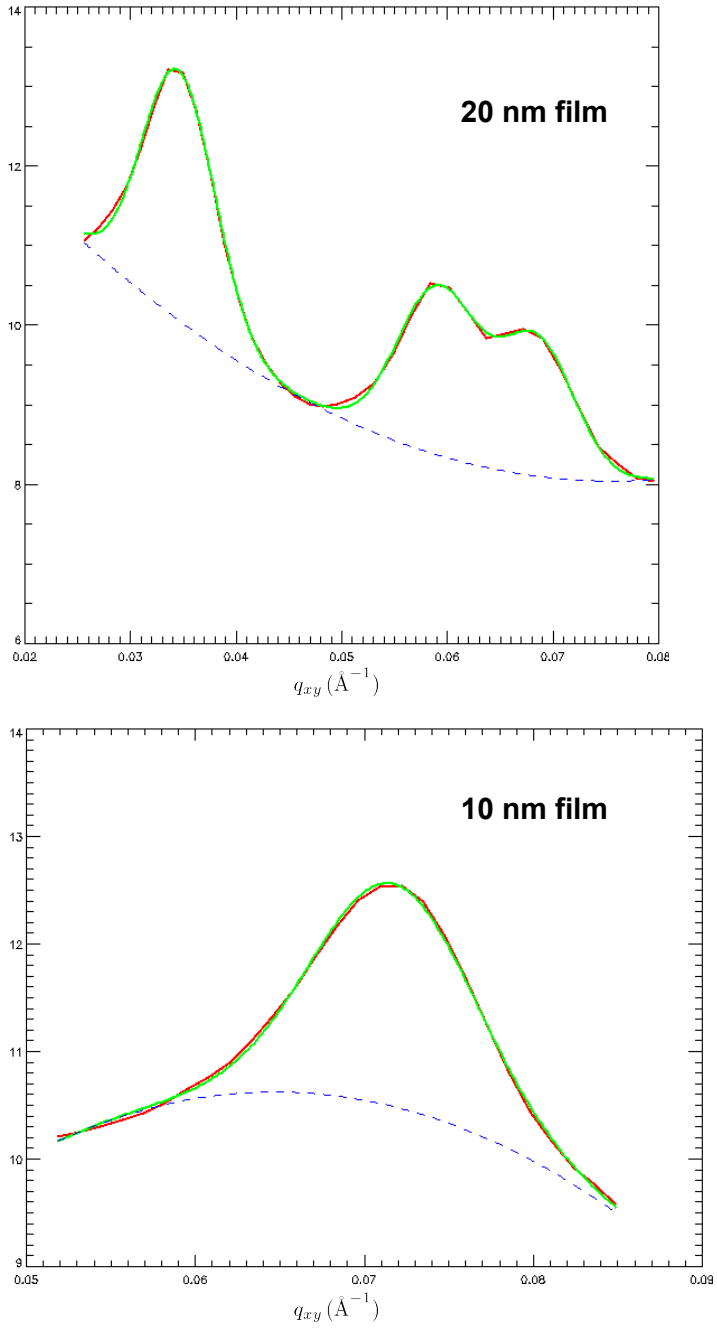

Figure 5.7: Peak fitting to the log of the mono–dispersed film data. The integrated data (red), the 3 Gaussian peak fit (green), and the quadratic background fit (blue dash).

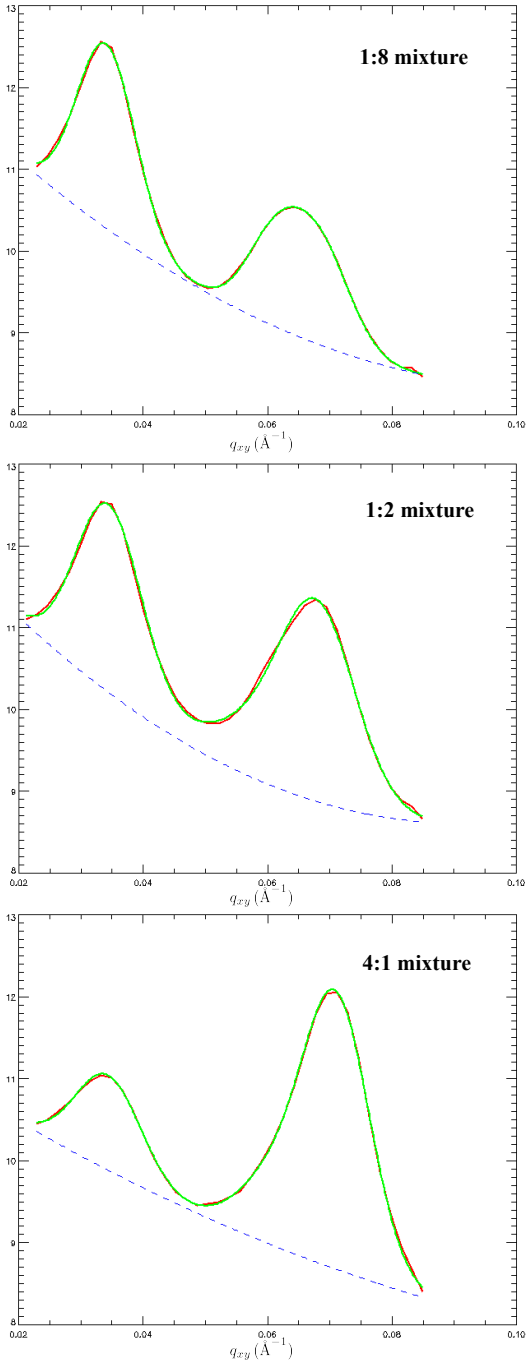

Figure 5.8: The results of a 3 Gaussian peak model with a quadratic background for the three bi–dispersed films.

Bibliography

[1] M. Pauly, B. P. Pichon, P. Panissod, S. Fleutot, P. Rodriguez, M. Drillon, and S. Begin-Colin, "Size dependent dipolar interactions in iron oxide nanoparticle monolayer and multilayer LangmuirBlodgett films," *Journal of Materials Chemistry*, vol. 22, no. 13, p. 6343, 2012.

[2] A. Figuerola, R. Di Corato, L. Manna, and T. Pellegrino, "From iron oxide nanoparticles towards advanced iron-based inorganic materials designed for biomedical applications.," *Pharmacological research : the official journal of the Italian Pharmacological Society*, vol. 62, pp. 126–43, Aug. 2010.

[3] S. Laurent, D. Forge, M. Port, A. Roch, C. Robic, L. V. Elst, and R. N. Muller, "Magnetic iron oxide nanoparticles: synthesis, stabilization, vectorization, physicochemical characterizations, and biological applications.," *Chemical reviews*, vol. 108, pp. 2064–2110, June 2008.

[4] S. R. Rudge, T. L. Kurtz, C. R. Vessely, L. G. Catterall, and D. L. Williamson, "Preparation, characterization, and performance of magnetic iron-carbon composite microparticles for chemotherapy.," *Biomaterials*, vol. 21, pp. 1411–20, July 2000.

[5] A. K. Gupta and M. Gupta, "Synthesis and surface engineering of iron oxide nanoparticles for biomedical applications.," *Biomaterials*, vol. 26, pp. 3995–4021, June 2005.

[6] A. Lozsán, M. García-Sucre, and G. Urbina-Villalba, "Steric interaction between spherical colloidal particles," *Physical Review E*, vol. 72, p. 061405, Dec. 2005.

[7] Y. Lalatonne, J. Richardi, and M. P. Pileni, "Van der Waals versus dipolar forces controlling mesoscopic organizations of magnetic nanocrystals.," *Nature materials*, vol. 3, pp. 121–5, Feb. 2004.

[8] P. C. Ohara, D. V. Leff, J. R. Heath, and W. M. Gelbart, "Crystallization of Opals from Polydisperse Nanoparticles," *Physical Review Letters*, vol. 75, no. 19, pp. 3466–3470, 1995.

[9] D. Schultz, X. Lin, and D. Li, "Structure, Wrinkling, and Reversibility of Langmuir Monolayers of Gold Nanoparticles," *Journal of Physical Chemistry B*, pp. 24522–24529, 2006.

[10] K. J. M. Bishop, C. E. Wilmer, S. Soh, and B. a. Grzybowski, "Nanoscale forces and their uses in self-assembly.," *Small (Weinheim an der Bergstrasse, Germany)*, vol. 5, pp. 1600–30, July 2009.

[11] H. C. Hamaker, "The London-van der Waals Attraction Between Spherical Particles," *Physica*, vol. 4, no. 10, 1937.

[12] B. Faure, G. Salazar-Alvarez, and L. Bergstrom, "Hamaker constants of iron oxide nanoparticles," *Langmuir*, pp. 8659–8664, 2011.

[13] D. Mishra and M. Benitez, "Self-assembled iron oxide nanoparticle multilayer: x-ray and polarized neutron reflectivity," *Nanotechnology*, vol. 23, 2012.

[14] C. Ménager, L. Belloni, and V. Cabuil, "Osmotic equilibrium between an ionic magnetic fluid and an electrostatic lamellar phase," *Langmuir*, vol. 17, no. 10, pp. 3516–3522, 1996.

[15] S. Das, P. Ranjan, P. S. Maiti, G. Singh, G. Leitus, and R. Klajn, "Dual-responsive nanoparticles and their self-assembly.," *Advanced materials (Deerfield Beach, Fla.)*, vol. 25, pp. 422–6, Jan. 2013.

[16] G. Singh, H. Chan, A. Baskin, and E. Gelman, "Self-assembly of magnetite nanocubes into helical superstructures," *Science*, vol. 345, no. 6201, pp. 380–382, 2014.

[17] G. Singh, H. Chan, T. Udayabhaskararao, E. Gelman, D. Peddis, A. Baskin, G. Leitus, P. Kral, and R. Klajn, "Magnetic field-induced self-assembly of iron oxide nanocubes," *Faraday Discuss.*, Jan. 2015.

[18] E. Gomar-Nadal, J. Puigmartí-Luis, and D. B. Amabilino, "Assembly of functional molecular nanostructures on surfaces.," *Chemical Society reviews*, vol. 37, pp. 490–504, Mar. 2008.

[19] J. Als-Nielsen and D. McMorrow, *Elements of Modern X-Ray Physics*. John Wiley and Sons, 2011.

[20] A. Guinier, *X-Ray Diffraction In Crystals, Imperfect Crystals, and Amorphous Bodies*. W. H. Freeman and Company, 1963.

[21] D. S. Sivia, *Elementary Scattering Theory for X-Ray and Neutron Users*. Oxford University Press, 2011.

[22] A. Braslau, P. Pershan, and G. Swislow, "Capillary waves on the surface of simple liquids measured by x-ray reflectivity," *Physical Review A*, vol. 38, no. 5, 1988.

[23] S. Sinha, E. Sirota, S. Garoff, and H. Stanley, "X-ray and neutron scattering from rough surfaces," *Physical Review B*, 1988.

[24] K. Mecke and S. Dietrich, "Effective Hamiltonian for liquid-vapor interfaces," *Physical Review E*, vol. 59, no. 6, pp. 6766–6784, 1999.

[25] C. Fradin, A. Braslau, D. Luzet, and M. Alba, "Investigating liquid surfaces down to the nanometer scale using grazing incidence X-ray scattering," *Physica B: Condensed . . .*, vol. 248, pp. 310–315, 1998.

[26] C. Fradin, A. Braslau, D. Luzet, and D. Smilgies, "Reduction in the surface energy of liquid interfaces at short length scales," *Nature*, pp. 871–874, 2000.

[27] L. Parratt, "Surface studies of solids by total reflection of X-rays," *Physical review*, vol. 95, 1954.

[28] W. C. Marra, "X-ray total-external-reflectionBragg diffraction: A structural study of the GaAs-Al interface," *Journal of Applied Physics*, vol. 50, no. 11, p. 6927, 1979.

[29] L. Wiegart, S. M. O'Flaherty, P. Terech, and B. Struth, "Observation of the desorption of mineral nanoparticles from a hybrid Langmuir monolayer: an in situ grazing incidence X-ray (GIXOS) study," *Soft Matter*, vol. 2, no. 1, p. 54, 2006.

[30] S. O'Flaherty, L. Wiegart, O. Konovalov, and B. Struth, "Observation of zinc phthalocyanine aggregates on a water surface using grazing incidence X-ray scattering," *Langmuir*, no. 25, pp. 11161–11166, 2005.

[31] Y. Dai, B. Lin, M. Meron, K. Kim, B. Leahy, and O. G. Shpyrko, "A comparative study of Langmuir surfactant films: Grazing incidence x-ray off-specular scattering vs. x-ray specular reflectivity," *Journal of Applied Physics*, vol. 110, no. 10, p. 102213, 2011.

[32] S. Mora, J. Daillant, D. Luzet, and B. Struth, "X-ray surface scattering investigation of Langmuir films: Phase transitions and elastic properties," *Europhysics Letters (EPL)*, vol. 66, pp. 694–700, June 2004.

[33] Q. Cao, S.-j. Han, G. S. Tulevski, Y. Zhu, D. D. Lu, and W. Haensch, "Arrays of single-walled carbon nanotubes with full surface coverage for high-performance electronics.," *Nature nanotechnology*, vol. 8, pp. 180–6, Mar. 2013.

[34] H. Zeng, J. Li, J. Liu, Z. Wang, and S. Sun, "Exchange-coupled nanocomposite magnets by nanoparticle self-assembly," *Nature*, vol. 420, no. November, pp. 395–398, 2002.

[35] P. Poddar, T. Telem-Shafir, T. Fried, and G. Markovich, "Dipolar interactions in two- and three-dimensional magnetic nanoparticle arrays," *Physical Review B*, vol. 66, p. 060403, Aug. 2002.

[36] V. Aleksandrovic, D. Greshnykh, I. Randjelovic, A. Frömsdorf, A. Kornowski, S. V. Roth, C. Klinke, and H. Weller, "Preparation and electrical properties of cobalt-platinum nanoparticle monolayers deposited by the Langmuir-Blodgett technique.," *ACS nano*, vol. 2, pp. 1123–30, June 2008.

[37] Y. Yang, L. Gao, G. P. Lopez, and B. B. Yellen, "Tunable assembly of colloidal crystal alloys using magnetic nanoparticle fluids.," *ACS nano*, vol. 7, pp. 2705–16, Mar. 2013.

[38] K. Wang, K. Jiang, B. Chung, T. Ouchi, P. J. Burke, D. a. Boysen, D. J. Bradwell, H. Kim, U. Muecke, and D. R. Sadoway, "Lithiumantimonylead liquid metal battery for grid-level energy storage," *Nature*, Sept. 2014.

[39] J. B. Edel, A. a. Kornyshev, and M. Urbakh, "Self-assembly of nanoparticle arrays for use as mirrors, sensors, and antennas.," *ACS nano*, vol. 7, pp. 9526–32, Nov. 2013.

[40] S.-C. Pang, M. a. Anderson, and T. W. Chapman, "Novel Electrode Materials for Thin-Film Ultracapacitors: Comparison of Electrochemical Properties of Sol-Gel-Derived and Electrodeposited Manganese Dioxide," *Journal of The Electrochemical Society*, vol. 147, no. 2, p. 444, 2000.

[41] K. Blodgett and I. Langmuir, "Built-up films of barium stearate and their optical properties," *Physical Review*, vol. 1007, no. 1935, pp. 964–983, 1937.

[42] I. Langmuir and V. Schaefer, "Activities of urease and pepsin monolayers," *Journal of the American Chemical . . .*, vol. 1115, no. 1, 1938.

[43] T. Wen and S. Majetich, "Ultra-large-area self-assembled monolayers of nanoparticles," *ACS nano*, vol. 5, no. 11, pp. 8868–8876, 2011.

[44] D. K. Lee, Y. H. Kim, C. W. Kim, H. G. Cha, and Y. S. Kang, "Vast magnetic monolayer film with surfactant-stabilized Fe3O4 nanoparticles using Langmuir-Blodgett technique.," *The journal of physical chemistry. B*, vol. 111, pp. 9288–93, Aug. 2007.

[45] K. Lee, M. Lipp, and D. Takamoto, "Apparatus for the continuous monitoring of surface morphology via fluorescence microscopy during monolayer transfer to substrates," *Langmuir*, vol. 9, no. 10, pp. 2567–2572, 1998.

[46] R. Banerjee, S. Hazra, S. Banerjee, and M. Sanyal, "Nanopattern formation in self-assembled monolayers of thiol-capped Au nanocrystals," *Physical Review E*, vol. 80, p. 056204, Nov. 2009.

[47] a. Datta, S. Kundu, M. Sanyal, J. Daillant, D. Luzet, C. Blot, and B. Struth, "Dramatic enhancement of capillary wave fluctuations of a decorated water surface," *Physical Review E*, vol. 71, p. 041604, Apr. 2005.

[48] L. Pocivavsek, S. L. Frey, K. Krishan, K. Gavrilov, P. Ruchala, A. J. Waring, F. J. Walther, M. Dennin, T. a. Witten, and K. Y. C. Lee, "Lateral stress relaxation and collapse in lipid monolayers.," *Soft matter*, vol. 4, pp. 2019–2029, Jan. 2008.

[49] G. D. Moon, T. I. Lee, B. Kim, G. Chae, J. Kim, S. Kim, J.-M. Myoung, and U. Jeong, "Assembled monolayers of hydrophilic particles on water surfaces.," *ACS nano*, vol. 5, pp. 8600–12, Nov. 2011.

[50] S. C. Glotzer, M. J. Solomon, and N. a. Kotov, "Self-assembly: From nanoscale to microscale colloids," *AIChE Journal*, vol. 50, pp. 2978–2985, Dec. 2004.

[51] S. Majetich, T. Wen, and R. Booth, "Functional magnetic nanoparticle assemblies: formation, collective behavior, and future directions," *ACS nano*, vol. 5, no. 8, pp. 6081–6084, 2011.

[52] D. Schwartz, J. Garnaes, R. Viswanathan, and J. Zasadzinski, "Surface order and stability of Langmuir-Blodgett films," *Science*, vol. 257, pp. 508–511, 1992.

[53] J. Zasadzinski, R. Viswanathan, L. Madsen, J. Garnaes, and D. Schwartz, "Langmuir-blodgett films," *Science*, vol. 263, 1994.

[54] R. Viswanathan, J. Zasadzinski, and D. Schwartz, "Spontaneous chiral symmetry breaking by achiral molecules in a Langmuir-Blodgett film," *Nature*, vol. 368, 1994.

[55] R. Banerjee, M. K. Sanyal, M. K. Bera, a. Singh, J. Novak, and O. Konovalov, "Structural reordering in monolayers of gold nanoparticles during transfer from water surface to solid substrate," *Physical Review E*, vol. 83, p. 051605, May 2011.

[56] P. Siffalovic and E. Majkova, "Self-assembly of nanoparticles at solid and liquid surfaces," *Smart Nanoparticles ...*, 2012.

[57] P. Müller-Buschbaum, "Grazing incidence small-angle X-ray scattering: an advanced scattering technique for the investigation of nanostructured polymer films.," *Analytical and bioanalytical chemistry*, vol. 376, pp. 3–10, May 2003.

[58] Y. Dai, B. Lin, M. Meron, K. Kim, B. Leahy, T. a. Witten, and O. G. Shpyrko, "Synchrotron X-ray studies of rapidly evolving morphology of self-assembled nanoparticle films under lateral compression.," *Langmuir : the ACS journal of surfaces and colloids*, vol. 29, pp. 14050–6, Nov. 2013.

[59] M. Pauly, B. P. Pichon, A. Demortière, J. Delahaye, C. Leuvrey, G. Pourroy, and S. Bégin-Colin, "Large 2D monolayer assemblies of iron oxide nanocrystals by the LangmuirBlodgett technique," *Superlattices and Microstructures*, vol. 46, pp. 195–204, July 2009.

[60] S. S. You, R. Rashkov, P. Kanjanaboos, I. Calderon, M. Meron, H. M. Jaeger, and B. Lin, "Comparison of the mechanical properties of self-assembled Langmuir monolayers of nanoparticles and phospholipids.," *Langmuir : the ACS journal of surfaces and colloids*, vol. 29, pp. 11751–7, Sept. 2013.

[61] V. Santhanam, J. Liu, R. Agarwal, and R. Andres, "Self-assembly of uniform monolayer arrays of nanoparticles," *Langmuir*, vol. 19, pp. 7881–7887, 2003.

[62] T. Kallio, J. Laine, and P. Stenius, "Intermolecular Interactions and the Adhesion of Oleic Acid," *Journal of Dispersion Science and Technology*, vol. 30, pp. 222–230, Jan. 2009.

[63] T. Ezquerra and M. Garcia-Gutierrez, *Applications of synchrotron light to scattering and diffraction in materials and life sciences*. Springer, 2009.

[64] I. Valmianski, C. Monton, and I. K. Schuller, "Microscopy image segmentation tool: robust image data analysis.," *The Review of scientific instruments*, vol. 85, p. 033701, Mar. 2014.

[65] P. de Gennes, "Deposition of langmuir-blodgett layers," *Colloid and Polymer Science*, vol. 465, pp. 463–465, 1986.

[66] Z. Jiang, X.-M. Lin, M. Sprung, S. Narayanan, and J. Wang, "Capturing the crystalline phase of two-dimensional nanocrystal superlattices in action.," *Nano letters*, vol. 10, pp. 799–803, Mar. 2010.

[67] L. Pocivavsek, R. Dellsy, A. Kern, S. Johnson, B. Lin, K. Y. C. Lee, and E. Cerda, "Stress and fold localization in thin elastic membranes.," *Science (New York, N.Y.)*, vol. 320, pp. 912–6, May 2008.

[68] Q. Guo, X. Teng, S. Rahman, and H. Yang, "Patterned langmuir-blodgett films of monodisperse nanoparticles of iron oxide using soft lithography," *Journal of the American Chemical Society*, vol. 125, pp. 630–631, Jan. 2003.

[69] F. Boyer, E. Guazzelli, and O. Pouliquen, "Unifying Suspension and Granular Rheology," *Physical Review Letters*, vol. 107, p. 188301, Oct. 2011.

[70] S. You, R. Rashkov, and P. Kanjanaboos, "Comparison of the Mechanical Properties of Self-Assembled Langmuir Monolayers of Nanoparticles and Phospholipids," *Langmuir*, 2013.

[71] M. Le Merrer, S. Cohen-Addad, and R. Höhler, "Bubble Rearrangement Duration in Foams near the Jamming Point," *Physical Review Letters*, vol. 108, pp. 1–4, May 2012.

[72] E. Brown, H. Zhang, N. A. Forman, B. W. Maynor, D. E. Betts, J. M. DeSimone, and H. M. Jaeger, "Shear thickening and jamming in densely packed suspensions of different particle shapes," *Physical Review E*, vol. 84, no. 3, p. 031408, 2011.

[73] L. Cipelletti, L. Ramos, S. Manley, E. Pitard, D. a. Weitz, E. E. Pashkovski, and M. Johansson, "Universal non-diffusive slow dynamics in aging soft matter," *Faraday Discussions*, vol. 123, pp. 237–251, Jan. 2003.

[74] A. Fluerasu, A. Moussaïd, A. Madsen, and A. Schofield, "Slow dynamics and aging in colloidal gels studied by x-ray photon correlation spectroscopy," *Physical Review E*, vol. 76, pp. 3–6, July 2007.

[75] A. Patterson, "The Scherrer formula for X-ray particle size determination," *Physical review*, vol. 56, pp. 978–982, 1939.

[76] Z. Nie, A. Petukhova, and E. Kumacheva, "Properties and emerging applications of self-assembled structures made from inorganic nanoparticles.," *Nature nanotechnology*, vol. 5, pp. 15–25, Jan. 2010.

[77] K. Kim, B. D. Leahy, Y. Dai, O. Shpyrko, J. S. Soltau, M. Pelton, M. Meron, and B. Lin, "Governing factors in stress response of nanoparticle films on water surface," *Journal of Applied Physics*, vol. 110, no. 10, p. 102218, 2011.

[78] K. Vegso, P. Siffalovic, M. Jergel, M. Weis, M. Benkovicova, E. Majkova, S. Luby, T. Kocsis, and I. Capek, "Silver Nanoparticle Monolayer-to-Bilayer Transition at the Air/Water Interface as Studied by the GISAXS Technique: Application of a New Paracrystal Model.," *Langmuir : the ACS journal of surfaces and colloids*, vol. 28, pp. 9395–404, June 2012.

[79] T. Sau and C. Murphy, "Self-assembly patterns formed upon solvent evaporation of aqueous cetyltrimethylammonium bromide-coated gold nanoparticles of various shapes," *Langmuir*, no. 5, pp. 2923–2929, 2005.

[80] S. Tatur, M. Maccarini, R. Barker, A. Nelson, and G. Fragneto, "Effect of functionalized gold nanoparticles on floating lipid bilayers," *Langmuir*, 2013.

[81] J. Saccani, S. Castano, B. Desbat, and D. Blaudez, "A phospholipid bilayer supported under a polymerized Langmuir film.," *Biophysical journal*, vol. 85, pp. 3781–7, Dec. 2003.

[82] J. Soeda, H. Matsui, T. Okamoto, I. Osaka, K. Takimiya, and J. Takeya, "Highly oriented polymer semiconductor films compressed at the surface of ionic liquids for high-performance polymeric organic field-effect transistors.," *Advanced materials (Deerfield Beach, Fla.)*, vol. 26, pp. 6430–5, Oct. 2014.

[83] T. Simmons, N. Maeda, J. Miao, M. Bravo-Sanchez, J. Dordick, and R. Linhardt, "Self-assembly of carbon nanotube films from room temperature ionic liquids," *Carbon*, vol. 58, pp. 226–231, July 2013.

[84] V. Sashuk, K. Winkler, A. ywociski, T. Wojciechowski, E. Górecka, and M. Fiakowski, "Nanoparticles in a capillary trap: dynamic self-assembly at fluid interfaces.," *ACS nano*, vol. 7, pp. 8833–9, Oct. 2013.

[85] T. D. Keijser and J. Langford, "Use of the Voigt function in a single-line method for the analysis of X-ray diffraction line broadening," *Journal of Applied . . .*, pp. 308–314, 1982.

[86] S. Förster, a. Timmann, M. Konrad, C. Schellbach, a. Meyer, S. S. Funari, P. Mulvaney, and R. Knott, "Scattering curves of ordered mesoscopic materials.," *The journal of physical chemistry. B*, vol. 109, pp. 1347–60, Feb. 2005.